약학박사 학위논문

Structural and Biophysical Characterization of human NDRG3, a key component of lactate-induced hypoxia responses

젖산 유도 저산소증 반응의 핵심 물질인 NDRG3의 구조 및 생물리학적 정의

2020년 02월

서울대학교 대학원

약학과 의약생명과학전공

김 경 록

Abstract

Structural and Biophysical Characterization of human NDRG3, a key component of lactate-induced hypoxia responses

Kyung Rok Kim

College of Pharmacy

The Graduate School

Seoul National University

The N-Myc downstream-regulated gene (NDRG) has been known to play promiscuous roles in cell proliferation, differentiation, and hypoxia-induced cancer metabolism. Especially, NDRG3 is related to proliferation and migration of prostate cancer cells. Furthermore, it has been reported to implicate lactate-triggered hypoxia responses and tumorigenesis. However, molecular mechanisms of the functions of NDRG3 remain unclear. Here, I report the crystal structure of human NDRG3 at 2.2 Å resolution with one homohexamer in an asymmetric unit. Although NDRG3 adopts an α/β-hydrolase superfamily fold, complete substitution of non-catalytic residues for the canonical catalytic triad and steric hindrance around the pseudo-active site seem to disable catalytic functions of α/β-hydrolase. NDRG3 shares a high similarity to NDRG2 in terms of amino acid sequence and structure. Interestingly, NDRG3 exhibits remarkable structural differences in a flexible loop corresponding to helix α6 of NDRG2 that is responsible for tumor suppression. Thus, this flexible loop region seems to play a distinct role in oncogenic progression induced by NDRG3. Collectively, these studies could provide structural and biophysical insights into

the molecular characteristics of NDRG3.

Keywords: N-Myc downstream-regulated gene 3 (NDRG3); α/β-hydrolase fold; Crystal structure; Unfolded helix

Student Number: 2014-30556

Table of Contents

List of Tables

List of Figures

Abbreviations

ASU	Asymmetric unit
CCD	Charge coupled device
CD	Circular dichroism
EST	Esterase
FPLC	Fast protein liquid chromatography
HIF	Hypoxia-inducible factors
ITC	Isothermal titration calorimetry
MALS	Multi angle light scattering
MR	Molecular replacement
MST	Microscale thermophoresis
NDRG	N-Myc downstream regulated gene
NTA	Nitrilotriacetic acid
PAGE	Polyacrylamide gel electrophoresis
PCR	Polymerase chain reaction
PDB	Protein data bank
PEG	Polyethylene glycol
PISA	Proteins, Interfaces, Structures and Assemblies
PHD	Proline hydroxylase
PTM	Post-translational modification
r.m.s.d.	Root-mean-square deviation
RT-PCR	Reverse transcription polymerase chain reaction

SDS	Sodium dodecyl sulfate
SEC	Size exclusion chromatography
SPR	Surface plasmon resonance
TCEP	Tris(2-carboxyethyl)phosphine hydrochloride
TCF	T-cell factor
XRD	X-ray diffraction

1. Introduction

1.1. The α/β-hydrolase fold

The α/β-hydrolase superfamily fold is one of the largest groups among structurally related proteins, since its discovery in 1992 (Ollis, et al., 1992, Protein Eng, 1). The fold contains eight canonical β-strands, wherein the second strand is antiparallel to rest and is surrounded by α-helices (Figure 1). Hydrolase activity is the primary function of the α/β-hydrolase superfamily and a nucleophile-histidine-acid in the catalytic triad is essential for hydrolysis. Some α/β-hydrolase fold proteins contain additional motifs of variable sizes, structures, and positions which aid substrate selection, regulation hydrolysis, or nonenzymatic function. Nonenzymatic α/β-hydrolase proteins, such as neuroligins, gliotactin, and thyroglobulin, have been reported to associate to multiprotein scaffolds or regulate protein-protein interactions (Botti, et al., 1998, Protein Eng, 2; De Jaco, et al., 2012, Protein Pept Lett, 3). Although the active site pocket of the nonenzymatic α/β-hydrolase fold is conserved, the substitution of non-active residues results in the loss of hydrolysis function. The inactive subfamilies seem to diverge from a hydrolase ancestor, with the catalytic triad being substituted by non-active residues during evolution (Marchot and Chatonnet, 2012, Protein Pept Lett, 4).

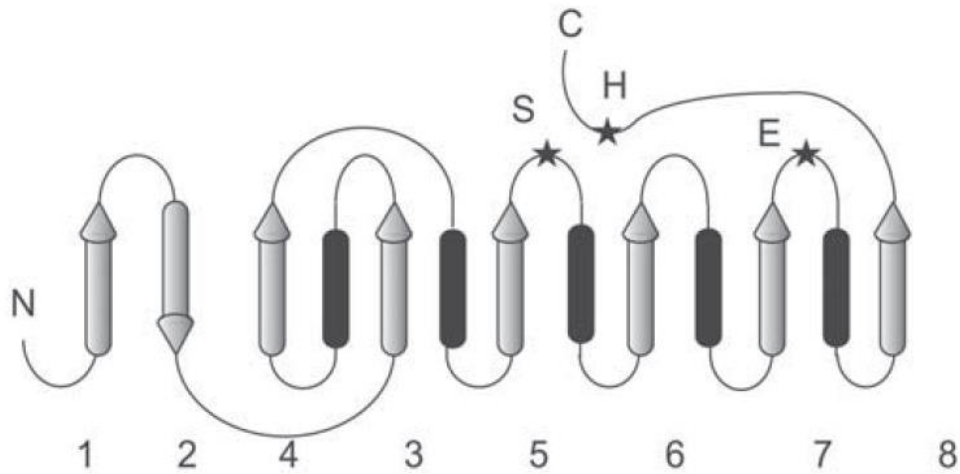

Figure 1. Schematic diagram of canonical α/β-hydrolase fold.

The canonical α/β-hydrolase fold consists of eight beta-strands surrounded by alpha-helices. Beta-strands and alpha-helices are represented by grey arrows and black cylinders, respectively. The positions of canonical catalytic triad are marked by black stars. S, H, and E letters indicate nucleophile, histidine, and acidic residues, respectively (Marchot and Chatonnet, 2012, Protein Pept Lett, 4).

1.2. N-Myc downstream-regulated gene family

The N-Myc downstream-regulated gene (NDRG) family is a member of the α/β-hydrolase superfamily and repressed by Myc expression (Shimono, et al., 1999, Mech Dev, 5; Shaw, et al., 2002, Proteins, 6). Since Myc overexpression is related to cell proliferation and metastasis, NDRG is believed to regulate tumor progression (O'Connell, et al., 2003, J Biol Chem, 7; Vervoorts, et al., 2006, J Biol Chem, 8). There are four NDRG proteins in human: NDRG1, NDRG2, NDRG3, and NDRG4. Human NDRG family proteins share 53-65% amino acid sequence identity and NDRG1 contains a characteristic three decapeptide sequence repeats motif in the C-terminal region (Figure 2 and Figure 3) (Qu, et al., 2002, Mol Cell Biochem, 9).

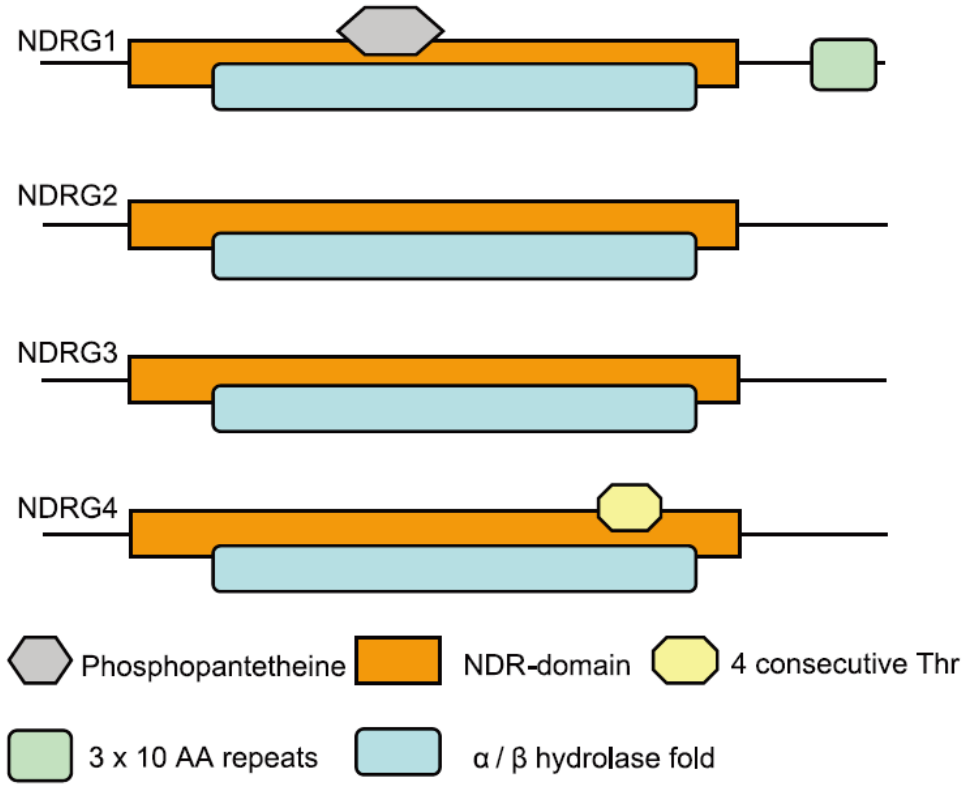

Figure 2. Structure of NDRG isoforms according to its sequences.

The domains are defined by the *Pfam* database (El-Gebali, et al., 2019, Nucleic Acids Res, 10). Represented are the NDR domain, α/β-hydrolase fold, regions altered in different isoforms (Phosphopantetheine, 3 X 10 amino acid repeats), and remarkable sequence details (4 consecutive Thr) (Melotte, et al., 2010, FASEB J, 11).

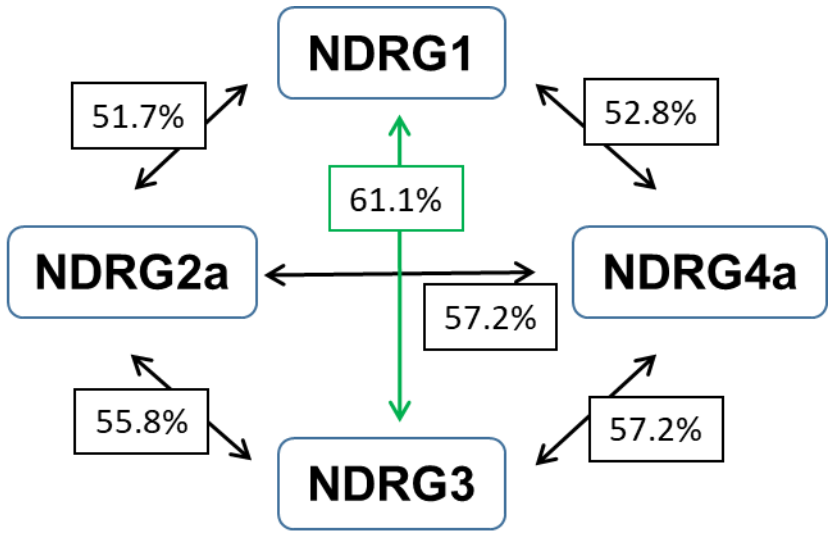

Figure 3. Sequence identities among NDRG isoforms.

The human NDRG isoforms sequences are cited from *Uniprot* database (https://www.uniprot.org). Green arrow represents the highest sequence identity.

Although NDRG family proteins share a high sequence identity, their tissue distributions differ and they play different roles in tumor regulation and hypoxia responses (Table 1 and Figure 4). For example, NDRG1 has been proposed to be a prognostic biomarker for colorectal cancer as it has been reported to suppresses cell invasion, migration, and proliferation rate (Kurdistani, et al., 1998, Cancer Res, 10; Guan, et al., 2000, Cancer Res, 11; Mao, et al., 2013, PLoS One, 12). NDRG2 is known to remarkably reduce cell proliferation in various types of cancer (Deng, et al., 2003, Int J Cancer, 13; Kim, et al., 2009, Int J Cancer, 14; Furuta, et al., 2010, Biochem Biophys Res Commun, 15; Ma, et al., 2010, J Exp Clin Cancer Res, 16; Ma, et al., 2012, PLoS One, 17; Huang, et al., 2015, Mol Med Rep, 18; Hong, et al., 2016, J Gastroenterol Hepatol, 19), as well as inhibit signaling pathways for oncogenic factors, such as lymphoid enhancer factor/T-cell factor (Kim, et al., 2009, Carcinogenesis, 20), nuclear factor-κB (Kim, et al., 2009, Carcinogenesis, 21), and matrix metalloproteinase-3 (Takarada-Iemata, et al., 2018, Glia, 22). Any roles of NDRG4 in tumors remain unidentified.

Isoform	Cancer type	Expression	Function	References
NDRG1	Breast	Low expressed in breast tumor cells with lymph node or bone metastasis.	Tumor suppressive	(Ring, et al., 2006, J Clin Oncol, 12; Bandyopadhyay, et al., 2004, Oncogene, 13)
	Colorectal	Low expressed in adenocarcinomas and metastatic colon cancer		(Guan, et al., 2000, Cancer Res, 14; van Belzen, et al., 1997, Lab Invest, 15)
	Glioma	Low expressed in brain cancer and enhanced from grade IV to grade I glioma		(Sun, et al., 2009, J Neurooncol, 16)
	Prostate	Low expressed in lymph node or bone metastasis patients.		(Bandyopadhyay, et al., 2003, Cancer Res, 17)
	Pancreatic	Expression is associated with regulating angiogenesis		(Maruyama, et al., 2006, Cancer Res, 18)
	Liver	Overexpressed in hepatocellular carcinoma correlated with differentiation, vascular invasion, and survive.	Oncogenic	(Chua, et al., 2007, Mod Pathol, 19)
	Cervical	Overexpressed in invasive cervical cancer compared to carcinoma.		(Nishio, et al., 2008, Cancer Lett, 20)
NDRG2	Liver	Downregulated in cancer	Tumor suppressive	(Lee, et al., 2008, Cancer Res, 21)
	Colon	Low expressed in cancer and adenomas.		(Chu, et al., 2011, Mol Cancer Ther, 22)
	Pancreatic	Low expressed in cancer.		(Yamamura, et al., 2013, Biochem Biophys Res Commun, 23)
	Gastric	Low expressed in cancer.		(Choi, et al., 2007, Exp Mol Med, 24)
	Glioblastoma	Downregulated in high-grade glioblastomas expression.		(Deng, et al., 2003, Int J Cancer, 25)
	Renal	Downregulated in cancer		(Liang, et al., 2012, Ann Surg Oncol, 26)

NDRG3	Prostate	Expressed in both prostate cancer cells and prostatic stromal cells	Oncogenic	(Wang, et al., 2009, Int J Cancer, 27)
	Liver	Overexpression is correlated with lactate induced cell proliferation.		(Lee, et al., 2015, Cell, 28; Jing, et al., 2018, Biosci Rep, 29)
	Colorectal	Overexpression is correlated with migration of colorectal cancer.		(Li, et al., 2018, Onco Targets Ther, 30)
	Prostate	Downregulated in advanced prostate cancer.	Tumor suppressive	(Lee, et al., 2018, Exp Mol Med, 31)
	Breast	Downregulated in advanced breast cancer.		(Estiar, et al., 2017, Future Oncol, 32)
NDRG4	Colorectal	Low expressed in cancer	Tumor suppressive	(Chu, et al., 2015, Oncotarget, 33)
	Glioblastoma	Increased in glioblastoma cells		(Ding, et al., 2012, OMICS, 34)

Table 1. Functions of NDRG isoforms in cancer (Melotte, et al., 2010, FASEB J, 11; Lee, et al., 2016, Oncotarget, 35).

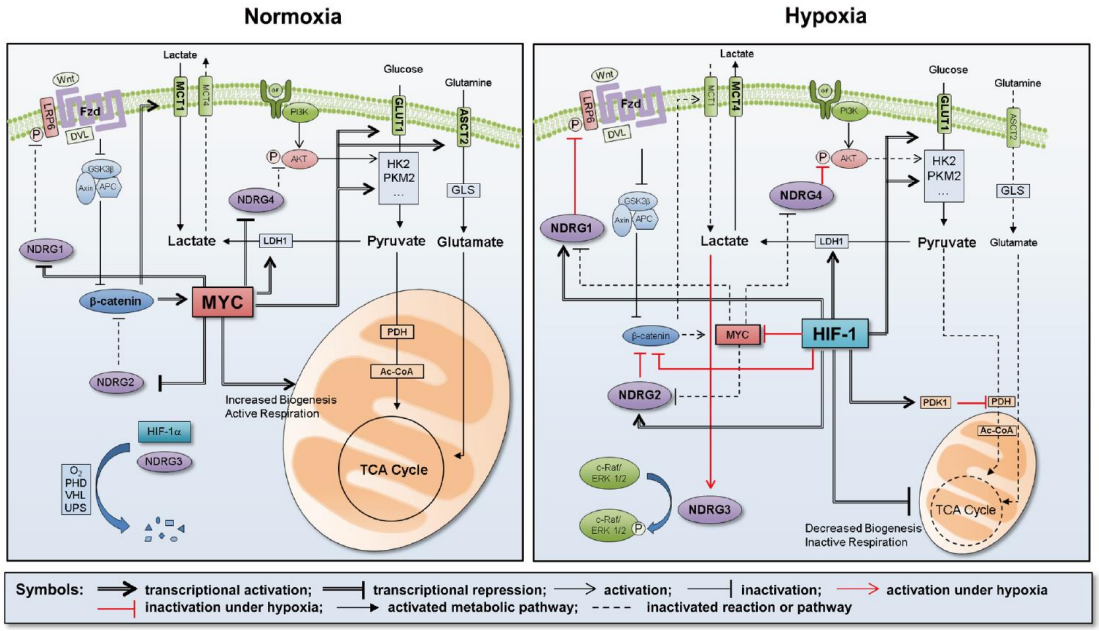

Figure 4. Summary of NDRG related hypoxia responses.

Under normoxia condition, NDRG isoforms are downregulated by Myc. Since NDRG isoforms are repressed by Myc, the mitochondrial energy metabolism turns to active state. However, HIF-1 controls energy metabolism instead of Myc under hypoxia and restricts the mitochondrial energy metabolism. HIF-1 directly and indirectly upregulates NDRG1, 2, and 4, and the NDRG isoforms play diverse roles in hypoxia. NDRG3 is not directly controlled by HIF-1 (Lee, et al., 2016, Oncotarget, 35).

1.3. Expression level and functions of NDRG3

Compared with the tumor suppressive NDRG members, NDRG3 has been reported to be oncogenic. NDRG3 is upregulated in epithelial prostate cancer cells and prostatic stromal cells at both the mRNA and protein level, and overexpression of NDRG3 induces cell proliferation and migration (Wang, et al., 2009, Int J Cancer, 27) (Figure 5). Furthermore, while NDRG1 is downregulated by N-Myc in different cell lines, NDRG3 does not seem to be downregulated by N-Myc (Figure 6).

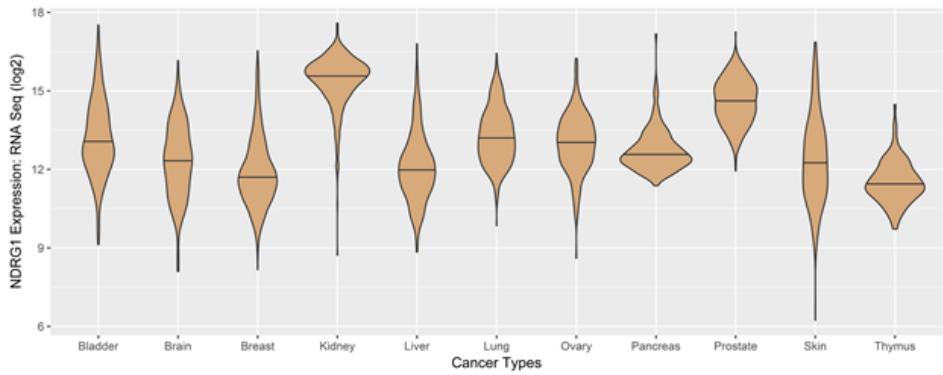
NDRG1 Expression: RNA Seq (log2)
18
15
12
9
6
Bladder
Brain
Breast
Kidney
Liver
Lung
Ovary
Pancreas
Prostate
Skin
Thymus
Cancer Types

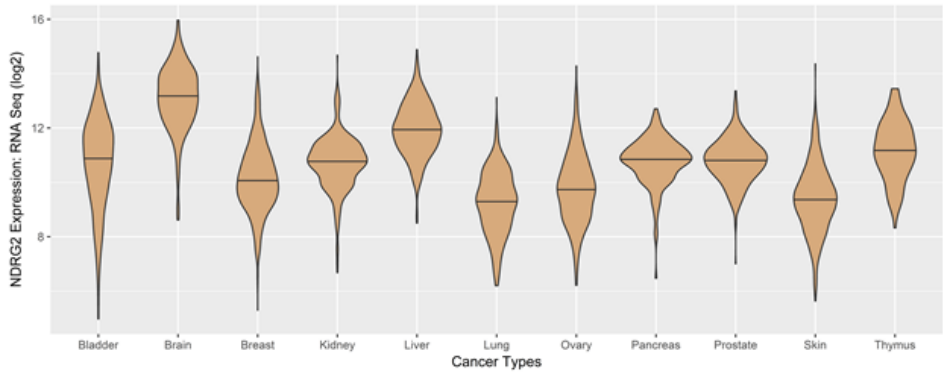
NDRG2 Expression: RNA Seq (log2)
16
12
8
Bladder
Brain
Breast
Kidney
Liver
Lung
Ovary
Pancreas
Prostate
Skin
Thymus
Cancer Types

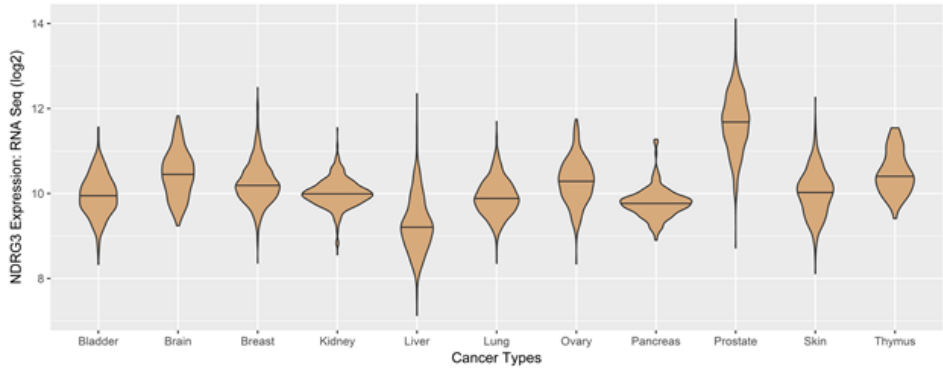
NDRG3 Expression: RNA Seq (log2)
14
12
10
8
Bladder
Brain
Breast
Kidney
Liver
Lung
Ovary
Pancreas
Prostate
Skin
Thymus
Cancer Types

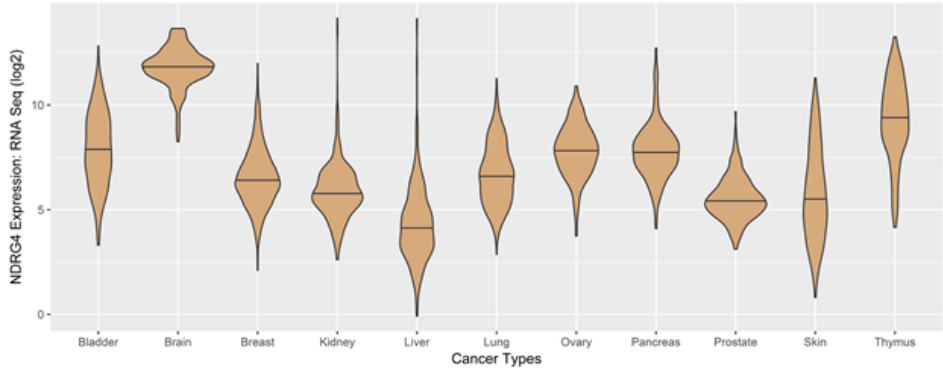
NDRG4 Expression: RNA Seq (log2)
10
5
0
Bladder
Brain
Breast
Kidney
Liver
Lung
Ovary
Pancreas
Prostate
Skin
Thymus
Cancer Types

Figure 5. RNA expression level of NDRG isoforms in different cancer types.

NDRG3 is highly expressed in prostate cancer cells. The data are analyzed using *cBioPortal* database (https://www.cbioportal.org) and cases were as below; Bladder Bladder Urothelial Carcinoma (408), Glioblastoma Multiforme (166), Breast Invasive Carcinoma (1,101), Kidney Renal Clear Cell Carcinoma (577), Liver Hepatocellular Carcinoma (373), Lung Adenocarcinoma (517), Ovarian Serous Cystadenocarcinoma (307), Pancreatic Adenocarcinoma (179), Prostate Adenocarcinoma (498), Skin Cutaneous Melanoma (472), and Thymoma (120).

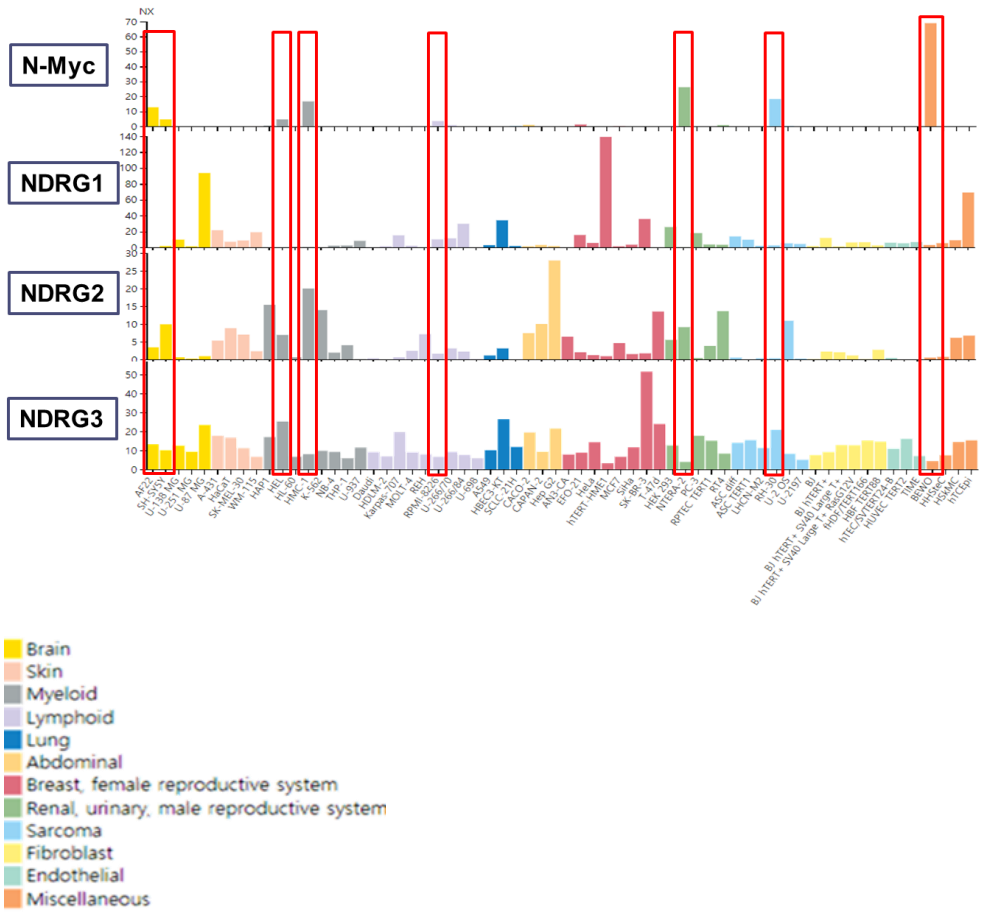

Figure 6. RNA expression level of NDRG isoforms in different cell lines.

Red boxes indicate the cell lines which highly express N-Myc. Compared with NDRG1, NDRG3 does not seem to be downregulated by N-Myc. The data of RNA expression is analyzed using *The Human Protein Atlas* database (https://www.proteinatlas.org).

Interestingly, NDRG3 plays a role in cell proliferation and anti-apoptosis under hypoxia. Lee at al. found a novel "NDRG3-Raf-ERK" pathway that was mediated by accumulated lactate under hypoxic conditions (Lee, et al., 2015, Cell, 28)(Figure 7 and 8). Under normoxia, NDRG3 is degraded by PHD2/VHL dependent ubiquitination. However, NDRG3 bypasses the degradation pathway when it is complexed with lactate, the end-product of anaerobic metabolism. The NDRG3-lactate complex is deposited in the cell and directly induces the phosphorylation of c-Raf, triggering ERK-mediated cell proliferation. Furthermore, the lactate-mediated "NDRG3-Raf-ERK" pathway could affect double-strand break repair in spermatogenesis by upregulating RAD51 via phosphorylating CREB (Pan, et al., 2017, Sci Rep, 36). In lieu of lactate-mediated NDRG3 signaling, NDRG3 provokes anti-apoptotic processes during hypoxia postcondition by regulating the adenosine A2a receptor (Cui, et al., 2017, Biochem Biophys Res Commun, 37), and activates Src phosphorylation in colorectal cancer progression (Li, et al., 2018, Onco Targets Ther, 30). On the other hand, NDRG3 is related to anti-metastatic function, which is mediated by dissociating the coactivator p300 from HIF-1α (Lee, et al., 2018, Exp Mol Med, 31).

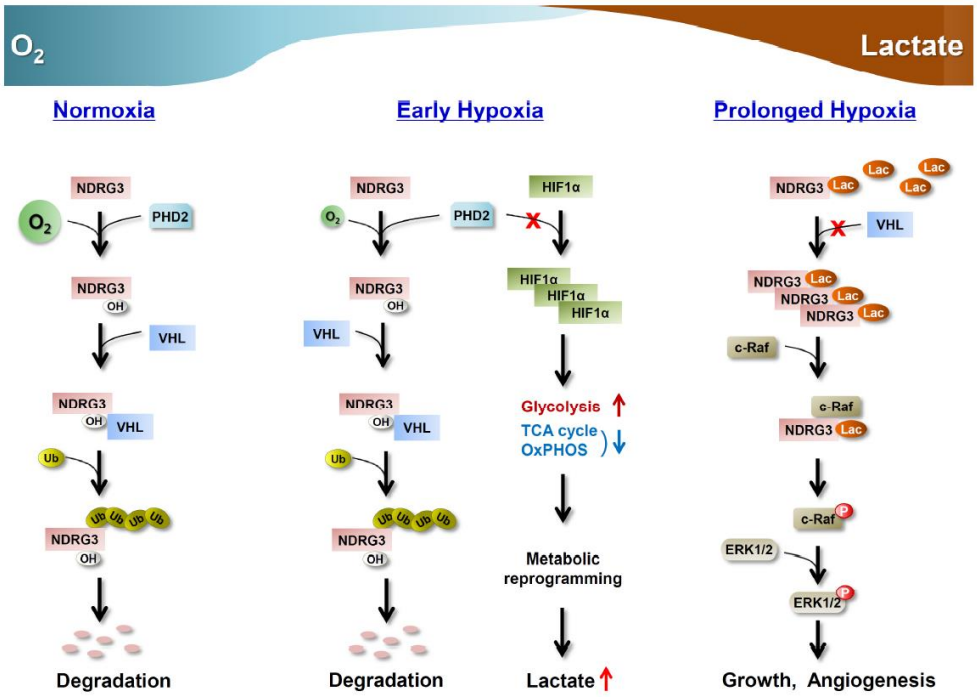

Figure 7. A scheme of hypoxia responses involving NDRG3.

NDRG3 is regulated by PHD2/VHL pathway under normoxia condition. When lactate binds to NDRG3, NDRG3 could bypass degradation pathway and accumulates in cells. NDRG3 triggers Raf-ERK signaling for cell growth and angiogenesis. (Park, et al., 2015, BMB Rep, 38)

Figure 8. A news article of lactate - induced cancer and QR code of the news video.

(https://www.youtube.com/watch?v=5H88g3AqpGU).

1.4. Purpose of this study

I was fascinated by NDRG3 which connect lactate, the end-product of glycolysis, to cancer. Furthermore, previous studies revealed that NDRG3 is related to hypoxia conditioning pathways. Although NDRG3 has been recently received attention for its promiscuous roles in regulating cell proliferation and metastasis, the structure of NDRG3 has not yet been elucidated.

To gain insights into the molecular mechanism of NDRG3, I determined the crystal structure of human NDRG3 and implemented biophysical studies on NDRG3.

2. Materials and Methods

2.1. Cloning, protein expression, and purification of NDRG3

The full-length of human NDRG3 gene encoded in pGEX4T-2 plasmid was presented by the Korea Research Institute of Bioscience and Biotechnology (Dr. Dong Chul Lee, Daejeon, Republic of Korea). The truncated gene (residues 29-320) was PCR-amplified using PrimeSTAR® HS DNA polymerase (Takara, Kusatsu, Japan) and subcloned to expression vector pET-28a(+) (Novagen, Kenilworth, NJ, USA) to produce recombinant protein containing a N-terminal hexahistidine tag (MGSSHHHHHHSSGLVPRGSHM)(Figure 9). The NDRG3 fused plasmid was transformed to an *Escherichia coli* strain, BLR(DE3) (Novagen, Kenilworth, NJ, USA) and cultured in Luria-Bertani medium (Alpha Biosciences, Baltimore, MD, USA) supplemented with 30 μg/mL kanamycin. NDRG3 protein expression was induced by addition of 0.5 mM isopropyl β-d-thiogalactopyranoside (IPTG) and the cells were incubated for 16 h at 293 K after growing to mid-log phase for 2 h at 310 K. The cells were pelleted by centrifugation at 6,000× g for 10 min at 277 K and disrupted by sonication in buffer A (20 mM 2-amino-2-(hydroxymethyl)propane-1,3-diol with hydrochloride (Tris-HCl) (pH 7.5), 500 mM sodium chloride, 35 mM Imidazole) with 1 mM phenylmethylsulfonyl fluoride (PMSF). The crude lysate was centrifuged at 36,000× g for 50 min at 277 K and the supernatant was transferred into a nickel-charged HiTrap™ Chelating HP column (GE Healthcare, Chicago, IL, USA). After wash with buffer

A, the column-bound proteins were eluted by the addition of a buffer containing 20 mM Tris-HCl (pH 7.5), 500 mM sodium chloride, and an imidazole gradient increasing from 35 to 1000 mM. During an imidazole gradient elution, NDRG3 protein was divided into monomer and dimer fractions (Figure 10).The protein was diluted with a buffer containing 20 mM Tris-HCl (pH 8.0), 50 mM of sodium chloride, 1% glycerol, and 0.5 mM tris(2-carboxyethyl)phosphine hydrochloride (TCEP) using a HiPrep™ 26/10 Desalting column (GE Healthcare, Chicago, IL, USA) and further purified using a HiTrap™ Q HP 5 ml column (GE Healthcare, Chicago, IL, USA) with linear gradient from 50 to 500 mM of sodium chloride. The eluted proteins were loaded on a HiLoad™ 16/600 Superdex 200 prep grade column (GE Healthcare, Chicago, IL, USA) equilibrated with 10 mM Tris-HCl (pH 7.5), 150 mM of sodium chloride, 1% glycerol, and 0.1 mM TCEP (Figure 11). The purified monomer protein was concentrated to 40 mg/mL using an Amicon Ultra-15 centrifugal filter unit (Merck Millipore, Burlington, MA, USA) for further studies.

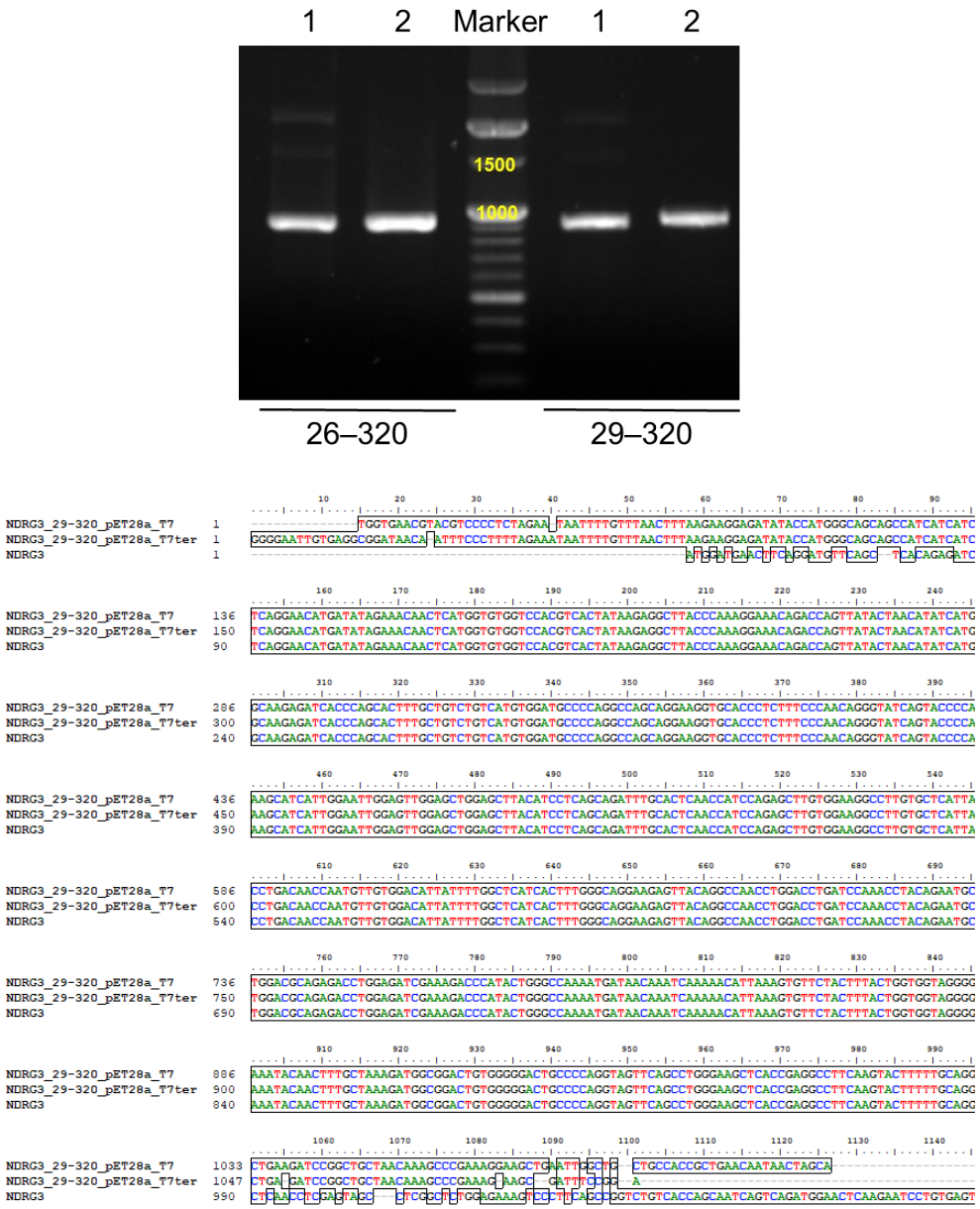

Figure 9. Cloning result of NDRG3.

NDRG3 gene (29-320) was amplified by PCR (up) and fused to expression vector. Yellow numbers indicate the base pair range of marker. The sequence of subcloned NDRG3 gene was equal to that of NDRG3 gene (down).

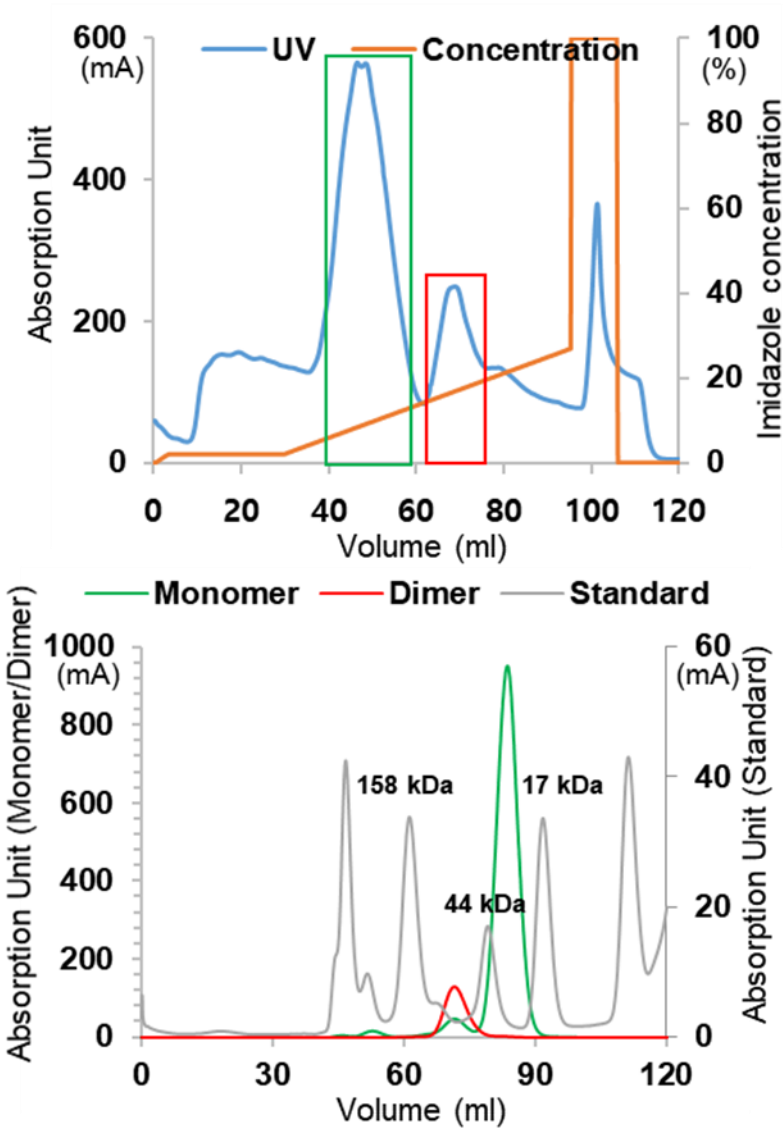

Figure 10. Preparation of NDRG3 dimer and monomer.

NDRG3 protein was divided into monomer and dimer fractions during an imidazole gradient elution. The green box is fractions of NDRG3 monomer and the red box is fractions of NDRG3 dimer.

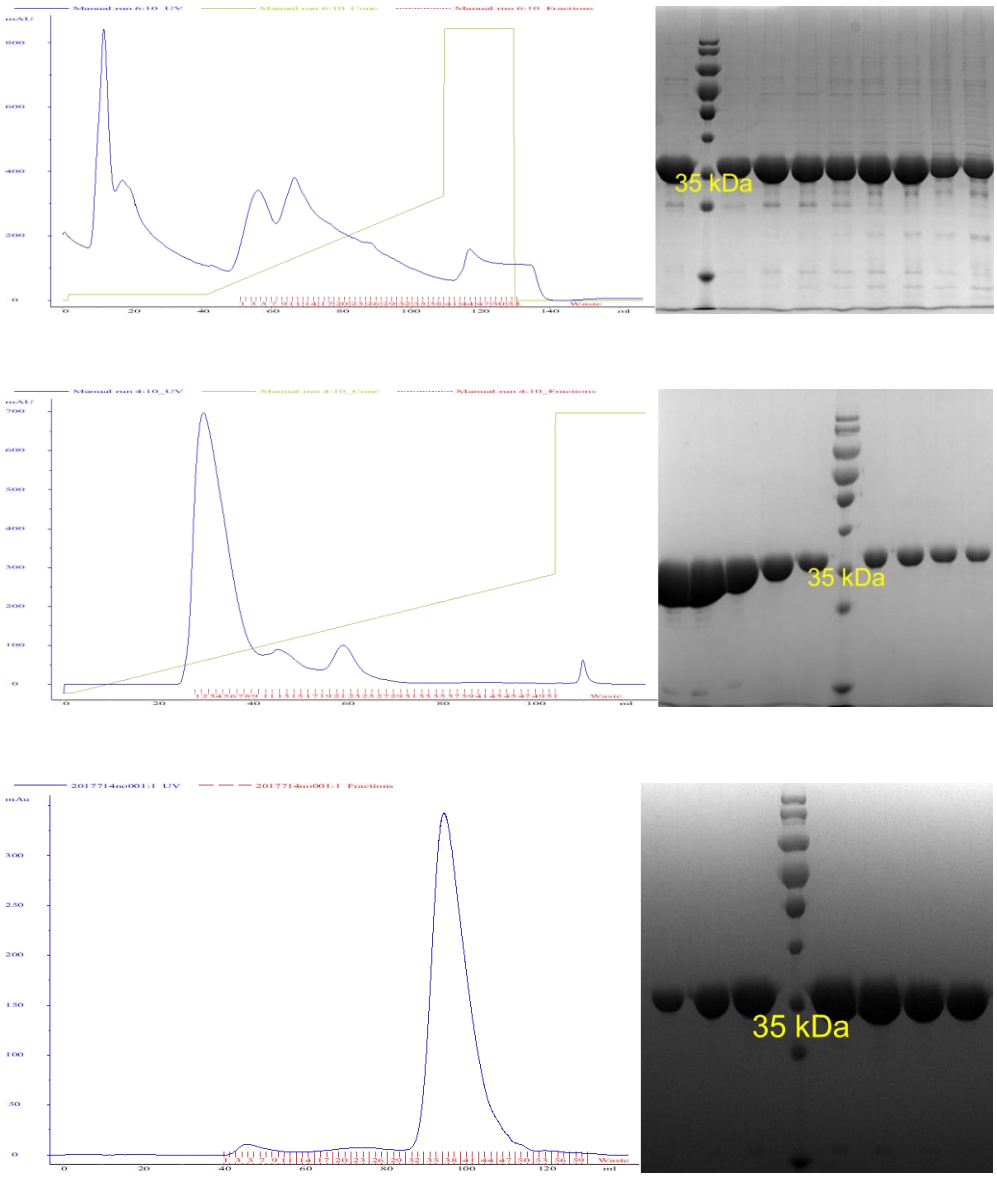

Figure 11. Purification steps of NDRG3 monomer.

Purification of NDRG3 was implemented with three steps; 1) affinity chromatography using Ni-NTA column (up), 2) ion exchange chromatography (middle), and 3) size exclusion chromatography (down). Purity of protein fractions was analyzed using SDS-PAGE.

2.2. Mutagenesis and purification of NDRG3

The NDRG3 mutants (C30S, S255A/N281A, I171M/S176H, and C30S/I171M/S176H) were produced by PCR-based site-directed mutagenesis (PrimeSTAR® HS DNA polymerase; Takara, Kusatsu, Japan). NDRG3 S255A/N281A mutant plasmid was transformed into BLR(DE3) *E. coli* strain (Novagen, Kenilworth, NJ, USA). Each cells containing NDRG3 wild type (WT) plasmid and S255A/N281A plasmid was cultured and induced by 0.5 mM of IPTG, and additionally incubated for 16 h at 293 K. The cells were pelleted by centrifugation at 6000× g for 10 min at 277 K and disrupted by sonication in a buffer containing 20 mM Tris-HCl pH 7.5, 500 mM sodium chloride, and 35 mM imidazole supplemented with 1 mM PMSF. The crude lysates were centrifuged at 36,000 × g for 50 min at 277 K and the resultant supernatant was loaded onto a nickel-charged HiTrap™ Chelating HP 5 ml column (GE Healthcare, Chicago, IL, USA). After washing unbound proteins, the column-bound proteins were eluted by addition of a buffer containing 20 mM Tris-HCl pH 7.5, 500 mM sodium chloride, and 300 mM imidazole. Then, 0.5 mg of eluted NDRG3 WT and S255A/N281A proteins were loaded onto Superdex™ 200 Increase 10/300 GL (GE Healthcare, Chicago, IL, USA) pre-equilibrated with 10 mM Tris-HCl pH 7.5, 150 mM sodium chloride, 1% glycerol, and 0.5 mM TCEP at flow rate of 0.75 mL/min using the ÄKTA Pure FPLC system (GE Healthcare, Chicago, IL, USA). NDRG3 C30S, I171M/S176H, and C30S/I171M/S176H mutated plasmids were transformed into SoluBL21™, *E. coli* strain (Gelantis, San Diego, CA, USA). The overexpression and purification steps were the same as for the purification of NDRG3 WT (Figure 12, 13, and 14). Each purified monomeric mutant was concentrated to 20 mg/mL

using an Amicon ultra-15 centrifugal filter unit (Merck Millipore, Burlington, MA, USA) for further studies.

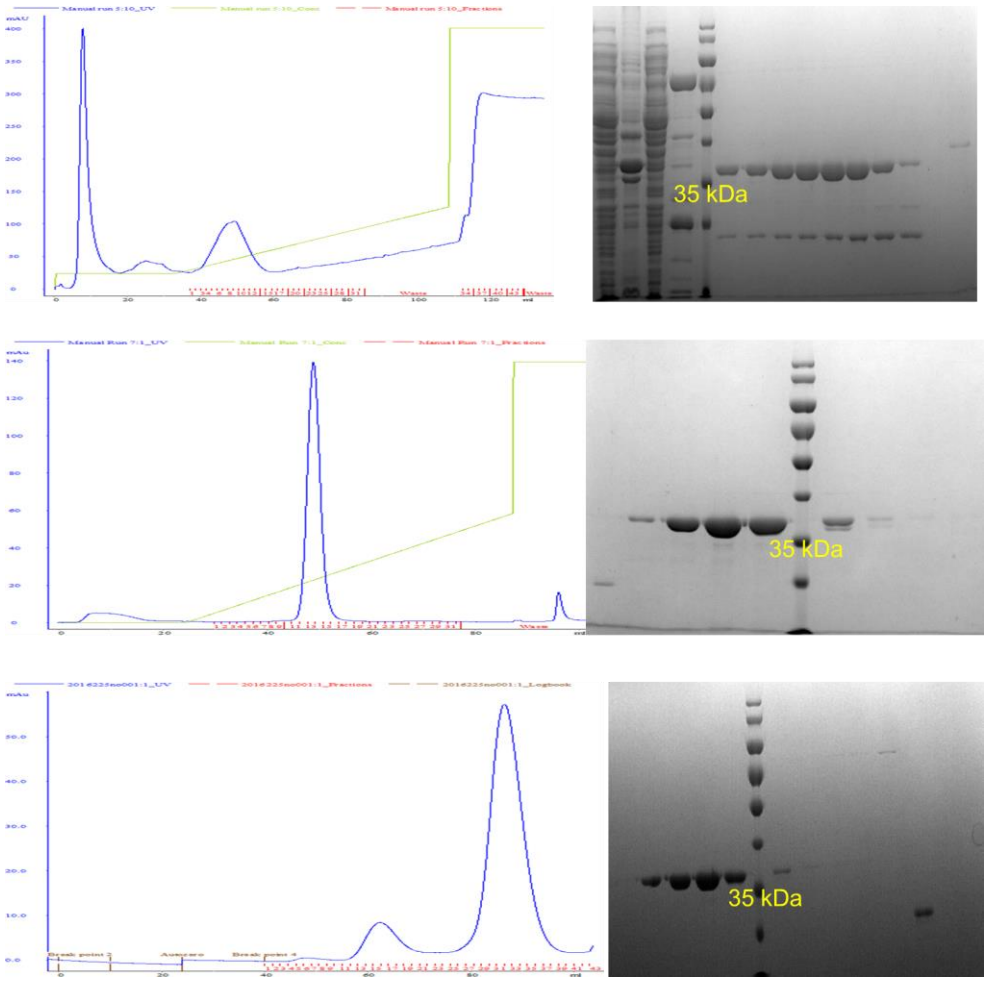

Figure 12. Purification steps of NDRG3 I171M/S176H.

Purification of NDRG3 I171M/S176H mutant was implemented with three steps; 1) affinity chromatography using Ni-NTA column (up), 2) ion exchange chromatography (middle), and 3) size exclusion chromatography (down). Purity of protein fractions was analyzed using SDS-PAGE.

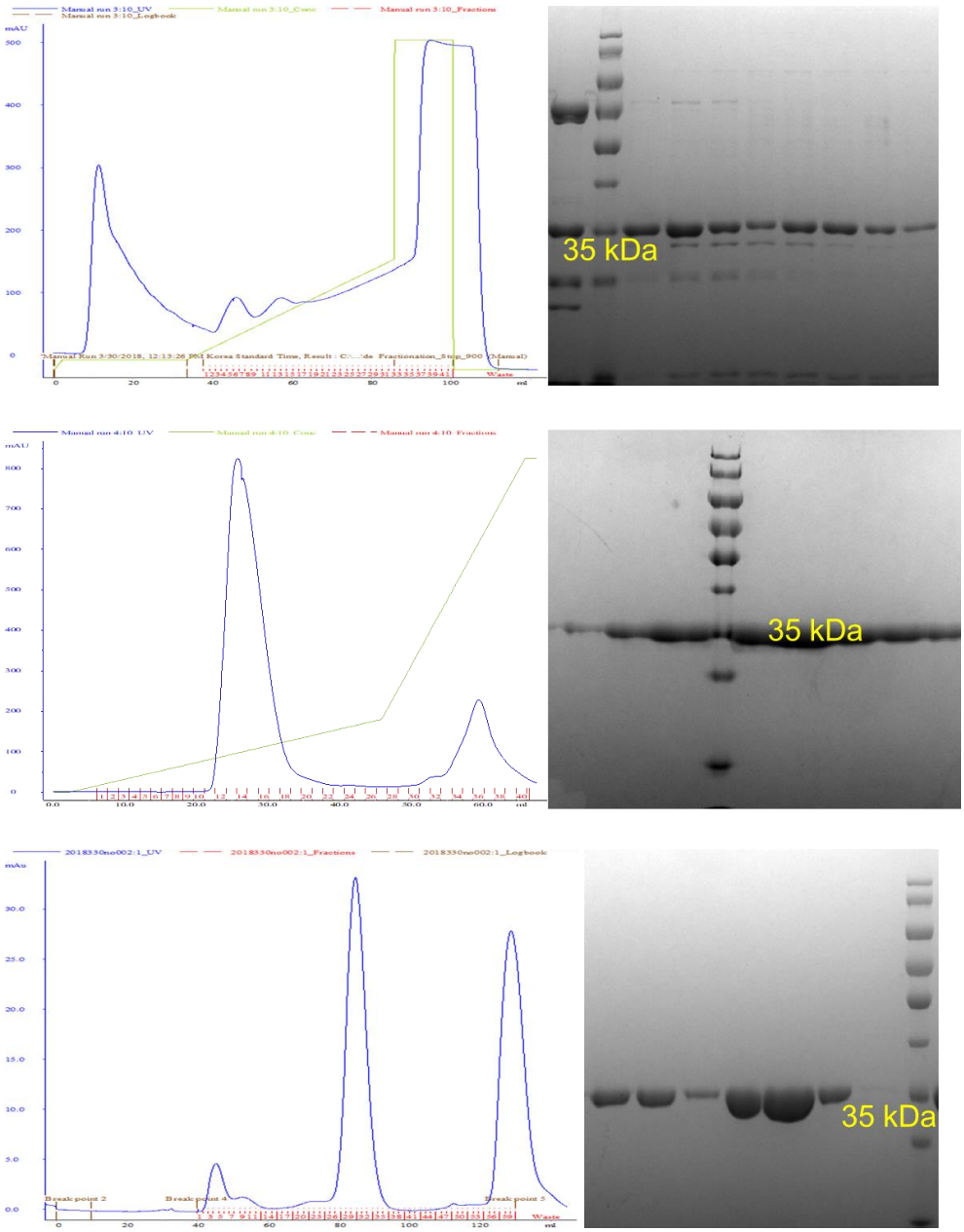

Figure 13. Purification steps of NDRG3 C30S.

Purification of NDRG3 C30S mutant was implemented with three steps; 1) affinity chromatography using Ni-NTA column (up), 2) ion exchange chromatography (middle), and 3) size exclusion chromatography (down). Purity of protein fractions was analyzed using SDS-PAGE.

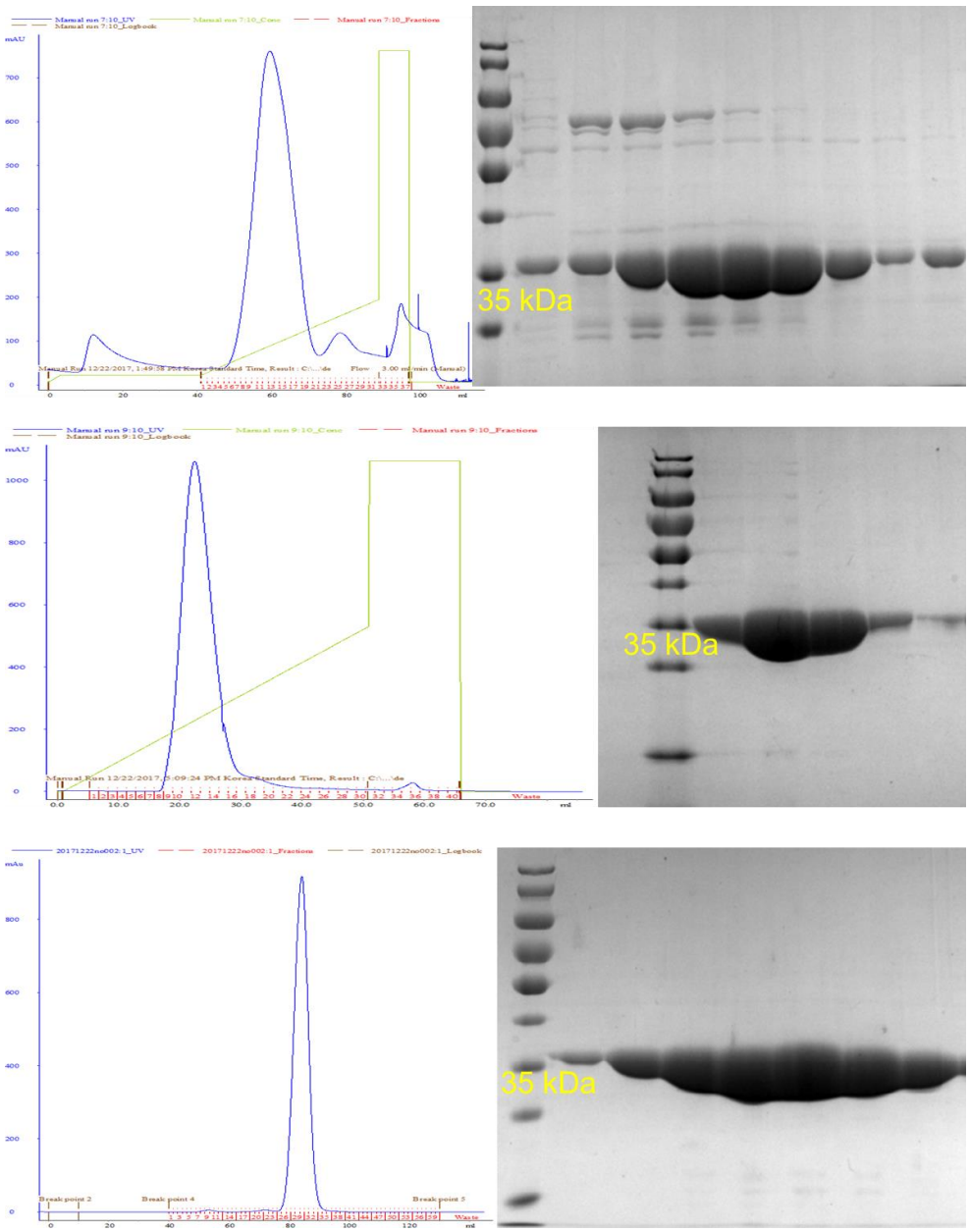

Figure 14. Purification steps of NDRG3 C30S/I171M/S176H.

Purification of NDRG3 C30S/I171M/S176H mutant was implemented with three steps; 1) affinity chromatography using Ni-NTA column (up), 2) ion exchange chromatography (middle), and 3) size exclusion chromatography (down). Purity of protein fractions was analyzed using SDS-PAGE.

2.3. Crystallization

The human NDRG3 (residues 29–320) was diluted to 20 mg/mL, and initial crystallization experiments were carried out with commercially available crystal screening kits using the sitting-drop vapor diffusion method at 295 K. First crystals were obtained by mixing 0.5 μL of 20 mg/mL NDRG3 and 0.5 μL of a solution containing 200 mM sodium citrate tribasic dihydrate and 20% polyethylene glycol (PEG)3,350 (Index; Hampton Research, Aliso Viejo, CA, USA) (Figure 15). Since the crystals did not well diffract, we optimized the crystals with a matrix screening containing 100–300 mM sodium citrate tribasic dihydrate and 10–30% PEG3,350 using the hanging-drop vapor diffusion method. The best diffracting crystal was grown in a drop mixed with 1 μL of 10 mg/mL protein solution, 0.8 μL of a crystallization solution containing 200 mM sodium citrate tribasic dihydrate and 20% PEG3,350, and 0.2 μL of the crystallization solution containing microseeds of the initial crystals (Figure 16). Initial crystals of NDRG3 C30S were obtained with the same crystallization solution as for NDRG3 crystals. The best diffracting crystal of C30S mutant was obtained by mixing 15 mg/mL protein supplemented with 0.01 mM TCEP (Figure 17). First crystals of NDRG3 I171M/S176H were obtained by mixing 0.5 μL of 13 mg/mL protein and an equal volume of crystallization solution containing 200 mM ammonium citrate tribasic (pH 7.0) and 20% PEG3,350 buffer condition (PEG/Ion 2; Hampton Research, Aliso Viejo, CA, USA). The crystals of I171M/S176H mutant were optimized with the crystallization solution supplemented with 3% dextran sulfate sodium salt (Mr 5000) (Figure 18). All crystals

were cryoprotected with paratone oil, then flash-frozen in a liquid nitrogen gas flow at 100 K prior to data collection.

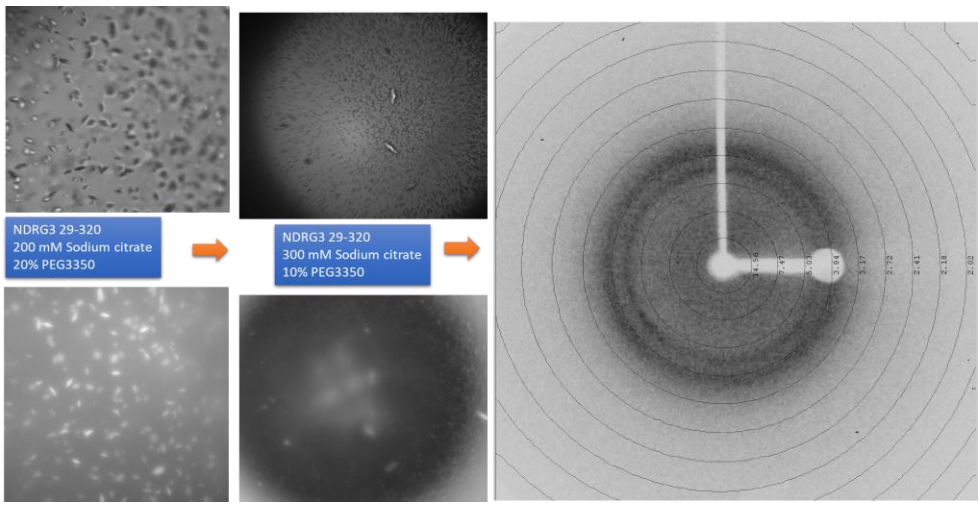

Figure 15. Initial crystals of NDRG3.

I obtained initial crystals of NDRG3 with 200 mM sodium citrate and 20% PEG3350 solution. Initial crystals were observed using microscope in visible light (up-left) and UV (down-left). Further optimized crystals of NDRG3 were observed using microscope in visible light (up-middle) and UV (down-middle). The first optimized crystal was checked by Supernova XRD machine to determine whether the crystal is protein crystal or small molecule crystal. (Agilent) (right).

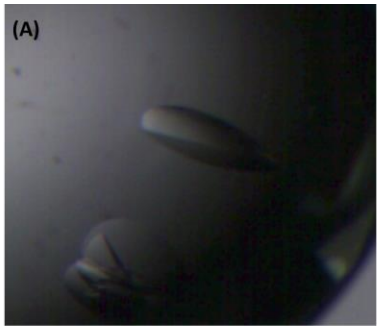

NDRG3 29-320
200 mM Sodium citrate
20% PEG3350
microseeding

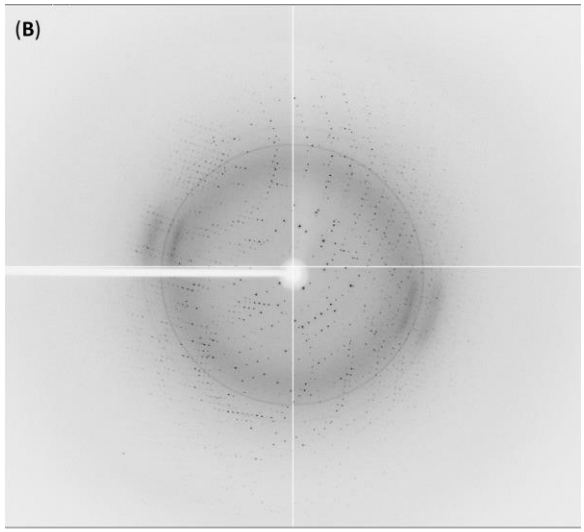

(C)

Shell Lower limit	Upper Angstrom	Average I	Average error	Norm. stat.	Linear Chi**2	Square R-fac	R-fac	Rmeas	Rpim	CC1/2	CC*
50.00	5.97	147.9	4.5	3.4	0.893	0.046	0.058	0.052	0.023	0.995	0.999
5.97	4.74	108.6	3.7	3.1	0.753	0.048	0.056	0.053	0.023	0.995	0.999
4.74	4.14	131.7	4.4	3.6	0.800	0.048	0.056	0.053	0.023	0.996	0.999
4.14	3.76	98.0	3.7	3.1	0.841	0.055	0.062	0.061	0.027	0.994	0.999
3.76	3.49	85.2	3.4	3.0	0.911	0.062	0.068	0.069	0.030	0.994	0.999
3.49	3.29	62.4	2.9	2.7	0.969	0.077	0.081	0.086	0.037	0.993	0.998
3.29	3.12	45.0	2.6	2.4	0.986	0.097	0.104	0.108	0.047	0.986	0.997
3.12	2.99	31.8	2.4	2.3	1.007	0.124	0.133	0.138	0.059	0.981	0.995
2.99	2.87	24.9	2.3	2.2	0.999	0.151	0.160	0.168	0.072	0.972	0.993
2.87	2.77	18.4	2.2	2.1	1.031	0.198	0.212	0.221	0.095	0.949	0.987
2.77	2.69	16.2	2.1	2.1	1.033	0.222	0.227	0.247	0.107	0.948	0.987
2.69	2.61	13.8	2.1	2.1	0.998	0.256	0.258	0.285	0.123	0.938	0.984
2.61	2.54	11.7	2.1	2.1	0.986	0.297	0.303	0.330	0.143	0.912	0.977
2.54	2.48	10.2	2.2	2.1	0.987	0.346	0.362	0.385	0.167	0.879	0.967
2.48	2.42	9.0	2.2	2.2	0.982	0.392	0.392	0.436	0.190	0.872	0.965
2.42	2.37	7.9	2.2	2.2	0.942	0.438	0.441	0.488	0.212	0.838	0.955
2.37	2.32	8.1	2.2	2.2	0.947	0.442	0.444	0.492	0.214	0.836	0.954
2.32	2.28	6.8	2.3	2.3	0.956	0.526	0.536	0.586	0.255	0.763	0.930
2.28	2.24	6.5	2.3	2.3	0.936	0.569	0.548	0.634	0.277	0.790	0.940
2.24	2.20	5.7	2.3	2.3	0.917	0.641	0.627	0.715	0.311	0.726	0.917
All reflections		42.8	2.7	2.5	0.944	0.101	0.077	0.113	0.049	0.991	0.998

Figure 16. The best diffracting crystal of NDRG3.

(A) The best diffracting crystal of NDRG3 was grown under 200 mM sodium citrate and 20% PEG3350 solution with microseed. (B) A diffraction image of the best diffracting crystal of NDRG3. (C) Scaling statistics of the best diffracting crystal of NDRG3.

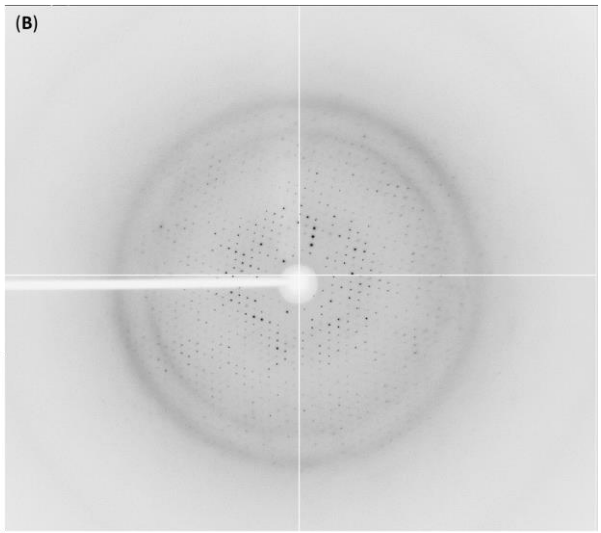

(C)

Shell Lower limit	Upper Angstrom	Average I	Average error	Average stat.	Norm. Chi**2	Linear R-fac	Square R-fac	Rmeas	Rpim	CC1/2	CC*
50.00	9.21	359.6	9.1	6.3	0.959	0.038	0.046	0.042	0.019	0.997	0.999
9.21	7.32	186.5	6.6	5.3	0.698	0.036	0.043	0.041	0.020	0.997	0.999
7.32	6.40	71.6	3.9	3.5	0.634	0.052	0.054	0.059	0.027	0.994	0.998
6.40	5.81	58.5	3.8	3.5	0.703	0.066	0.063	0.075	0.035	0.993	0.998
5.81	5.40	63.8	4.1	3.8	0.745	0.066	0.062	0.075	0.034	0.994	0.998
5.40	5.08	60.7	4.3	4.1	0.804	0.076	0.073	0.087	0.040	0.991	0.998
5.08	4.82	68.7	4.8	4.5	0.836	0.078	0.072	0.089	0.042	0.992	0.998
4.82	4.61	65.8	4.9	4.7	0.908	0.088	0.081	0.101	0.048	0.990	0.998
4.61	4.44	59.6	5.0	4.8	0.958	0.106	0.097	0.121	0.056	0.987	0.997
4.44	4.28	54.1	5.0	4.8	0.993	0.117	0.106	0.135	0.063	0.986	0.996
4.28	4.15	36.4	4.8	4.7	1.068	0.180	0.161	0.206	0.096	0.968	0.992
4.15	4.03	31.9	4.8	4.8	1.007	0.191	0.169	0.218	0.102	0.965	0.991
4.03	3.92	28.0	4.9	4.8	1.016	0.233	0.206	0.266	0.124	0.949	0.987
3.92	3.83	26.9	5.0	5.0	1.033	0.256	0.230	0.293	0.136	0.941	0.985
3.83	3.74	24.3	5.2	5.2	1.039	0.296	0.268	0.339	0.158	0.907	0.975
3.74	3.66	24.9	5.4	5.3	1.108	0.308	0.282	0.353	0.166	0.873	0.966
3.66	3.59	23.0	5.5	5.4	1.066	0.339	0.318	0.387	0.180	0.876	0.966
3.59	3.52	16.1	5.4	5.4	1.079	0.471	0.390	0.538	0.250	0.844	0.957
3.52	3.46	13.5	5.3	5.3	1.030	0.553	0.469	0.632	0.293	0.785	0.938
3.46	3.40	10.3	5.3	5.3	0.983	0.695	0.559	0.794	0.369	0.729	0.918
All reflections		65.6	5.2	4.8	0.936	0.095	0.064	0.108	0.050	0.992	0.998

Figure 17. The best diffracting crystal of NDRG3 C30S.

(A) The best diffracting crystal of NDRG3 C30S mutant was grown under 200 mM sodium citrate, 20% PEG3350, and 0.01 mM TCEP solution. (B) A diffraction image of the best diffracting crystal of NDRG3 C30S mutant. (C) Scaling statistics of the best diffracting crystal of NDRG3 C30S mutant.

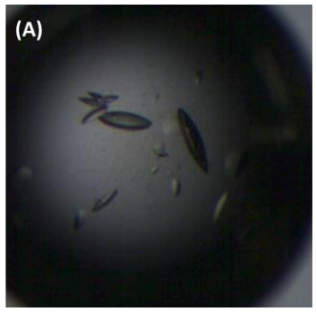

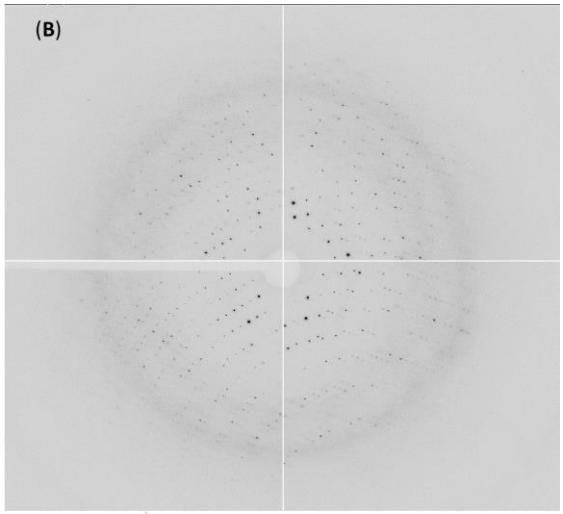

NDRG3 29-320 I171M/S176H
200 mM ammonium citrate tribasic (pH 7.0)
20% PEG3350
3% dextran sulfate sodium salt (Mr 5,000)

(C)

Shell Lower limit	Upper Angstrom	Average I	Average error	Average stat.	Chi**2	Norm. R-fac	Linear R-fac	Square Rmeas	Rpim	CC1/2	CC*
50.00	8.94	32.0	1.5	0.8	0.918	0.062	0.083	0.071	0.034	0.990	0.998
8.94	7.10	9.7	0.6	0.4	0.939	0.073	0.079	0.084	0.040	0.993	0.998
7.10	6.21	3.7	0.3	0.3	0.986	0.114	0.120	0.131	0.064	0.973	0.993
6.21	5.64	3.6	0.3	0.3	1.034	0.129	0.127	0.148	0.071	0.979	0.995
5.64	5.24	3.7	0.4	0.3	1.130	0.139	0.139	0.160	0.077	0.970	0.992
5.24	4.93	4.0	0.4	0.4	1.084	0.139	0.135	0.159	0.077	0.975	0.994
4.93	4.68	4.1	0.4	0.4	1.103	0.146	0.146	0.168	0.080	0.968	0.992
4.68	4.48	4.0	0.4	0.4	1.094	0.146	0.146	0.168	0.081	0.970	0.992
4.48	4.31	3.5	0.4	0.4	1.155	0.170	0.161	0.197	0.098	0.960	0.990
4.31	4.16	2.6	0.4	0.4	1.125	0.214	0.184	0.246	0.119	0.960	0.990
4.16	4.03	2.0	0.4	0.4	1.127	0.268	0.239	0.308	0.149	0.935	0.983
4.03	3.91	2.0	0.4	0.4	1.106	0.270	0.253	0.310	0.149	0.919	0.979
3.91	3.81	1.8	0.4	0.4	1.089	0.307	0.286	0.352	0.169	0.911	0.976
3.81	3.72	1.6	0.4	0.4	1.103	0.333	0.317	0.383	0.184	0.884	0.969
3.72	3.63	1.4	0.4	0.4	1.035	0.376	0.326	0.432	0.210	0.889	0.970
3.63	3.55	1.3	0.4	0.4	1.000	0.385	0.342	0.444	0.218	0.880	0.967
3.55	3.48	1.0	0.4	0.4	0.997	0.465	0.515	0.540	0.270	0.830	0.952
3.48	3.42	0.9	0.4	0.4	0.993	0.483	0.434	0.565	0.286	0.781	0.937
3.42	3.36	0.8	0.4	0.4	1.013	0.501	0.468	0.592	0.308	0.750	0.926
3.36	3.30	0.7	0.4	0.4	0.965	0.576	0.562	0.679	0.351	0.672	0.896
All reflections		4.2	0.4	0.4	1.053	0.137	0.093	0.158	0.077	1.054	1.013

Figure 18. The best diffracting crystal of NDRG3 I171M/S176H.

(A) The best diffracting crystal of NDRG3 I171M/S176H mutant was grown under 200 mM ammonium citrate tribasic (pH 7.0), 20% PEG3350, and 3% dextran sulfate sodium salt (Mr 5,000) solution. (B) A diffraction image of the best diffracting crystal of NDRG3 I171M/S176H mutant. (C) Scaling statistics of the best diffracting crystal of NDRG3 I171M/S176H mutant.

2.4. X-ray data collection, refinement and structure determination

X-ray diffraction data of NDRG3 and C30S mutant crystals were collected at BL-7A synchrotron beam line at the Pohang Light Source (Pohang, Republic of Korea), using a Quantum Q270 CCD detector (Area Detector Systems Corporation, Poway, CA, USA). The diffraction data of NDRG3 crystal were integrated and scaled in *C*-centered monoclinic space group *C*2 using *HKL2000* program (Otwinowski and Minor, 1997, Methods Enzymol, 39) with six monomers in an asymmetric unit (ASU). The structure was solved using molecular replacement method with the structure of human NDRG2 protein (PDB Id: 2XMQ) (Hwang, et al., 2011, J Biol Chem, 40) as a phasing model using *PHASER-MR* in the *PHENIX* software (Adams, et al., 2010, Acta Crystallogr D Biol Crystallogr, 41). The model was completed by iterative cycles of refinement using *REFMAC5* (Vagin, et al., 2004, Acta Crystallogr D Biol Crystallogr, 42) in the *CCP4i* software suite (Winn, et al., 2011, Acta Crystallogr D Biol Crystallogr, 43) and *Wincoot* (Emsley, et al., 2010, Acta Crystallogr D Biol Crystallogr, 44). All refinement steps were monitored with R_{free} value calculated from 5.0% of the independent reflections. Because of merohedral twinning of NDRG3 crystal, the intensity-based twin law option in *REFMAC5* was applied for all refinement processes. The space group of NDRG3 C30S crystal was $P3_121$ and it contains four molecules in an ASU. The crystal structure of NDRG3 C30S was determined using *PHASER-MR* in the *PHENIX* software and refined using *REFMAC5*. I adjusted the TLS refinement option of which parameters were calculated by *PDB-REDO* (Joosten, et al., 2014, IUCrJ, 45). X-ray

diffraction data for NDRG3 I171M/S176H were collected at BL-11C Pohang Light Source (Pohang, Republic of Korea), using a Pilatus3 6M detector (Dectris, Baden-Daettwil, Switzerland). The space group of the mutant crystal was $P3_221$ and the structure was determined using *PHASER-MR* in the *PHENIX* software. Since the diffraction data were predicted to contain merohedral twinning, twin law was adjusted to mutant refinement at the processing in *REFMAC5* as for the NDRG3 wild type crystal. The stereochemical qualities of the NDRG3 and mutants models were checked using *MolProbity* (Chen, et al., 2010, Acta Crystallogr D Biol Crystallogr, 46). The data collection and refinement statistics are summarized in Table 1. Graphical representations for the protein structure were drawn using *PyMOL* (Schrodinger, 2015, 47) (Table 2).

Table 2. Statistics for data collection and model refinement

	NDRG3	NDRG3 C30S	NDRG3 I171M/S176H
Data Collection [a]			
Beamline	PLS-7A	PLS-7A	PLS-11C
Space group	$C2$	$P3_121$	$P3_221$
Cell dimensions			
a, b, c (Å), α, β, γ (°)	173.34, 100.15, 110.74, 90.00, 90.01, 90.00	99.76, 99.76, 332.71, 90.00, 90.00, 120.00	100.39, 100.39, 111.76, 90.00, 90.00, 120.00
X-ray wavelength (Å)	0.9793	0.9793	0.9794
Resolution (Å)[b]	50.0-2.2 (2.24-2.20)	50.0-3.4 (3.46-3.40)	50.0-3.3 (3.36-3.30)
$\langle I/\sigma(I)\rangle$	15.9 (2.5)	16.6 (2.6)	14.0 (3.0)
Unique reflections	95,796 (4,774)	26,798 (1,311)	10,073 (485)
Redundancy	5.2 (5.1)	6.6 (6.7)	10.5 (8.8)
Completeness (%)	99.7 (99.3)	97.7 (97.5)	99.3 (95.8)
R_{merge} (%)[c]	10.1 (64.1)	10.3 (73.2)	16.4 (62.9)
$R_{p.i.m}$ (%)[d]	4.9 (31.1)	3.9 (27.5)	5.4 (21.5)
Refinement			
No. of reflections	88,791	25,238	9,142
Resolution (Å)	50.0-2.2 (2.24-2.20)	50.0-3.4 (3.46-3.40)	50.0-3.3 (3.36-3.30)
R^e_{work}/R_{free}[f] (%)	16.8%/18.5%	24.1%/27.7%	19.6%/22.6%
Twin fraction	0.172, 0.177, 0.195, 0.129, 0.131, 0.197[g]		0.502, 0.498[h]
No. of subunits	6	4	2
No. of protein atoms	13,139	8,673	4,345
No. of solvent atoms	334	0	6
Mean B value (Å^2)	31.59	125.18	33.22
Ramachandran plot (%)			
favored	1629 (97.7%)	1,085 (98.4%)	541 (98.0%)
allowed	39 (2.3%)	18 (1.6%)	11 (2.0%)
outliers	0 (0%)	0 (0%)	0 (0%)
Rotamer outliers (%)	0 (0%)	0 (0%)	0 (0%)
r.m.s. deviations			
bond lengths (Å)	0.002	0.003	0.004
bond angles (°)	1.143	1.246	1.279

[a] Data collected at the Pohang Light Source.

[b] numbers in parentheses indicate the highest resolution shell of 20.

[c] $R_{merge} = \Sigma_h \Sigma_i |I(h)_i - \langle I(h) \rangle| / \Sigma_h \Sigma_i I(h)_i$, where I(h) is the observed intensity of reflection h, and < I(h) > is the average intensity obtained from multiple measurements.

[d] $R_{p.i.m} = \Sigma_h \sqrt{(1/n-1)} \Sigma_i |I(h)_i - \langle I(h) \rangle| / \Sigma_h \Sigma_i I(h)_i$, where I(h) is the observed intensity of reflection h, and < I(h) > is the average intensity obtained from multiple measurements.

[e] $R = \Sigma ||F_o| - |F_c|| / \Sigma |F_o|$, where $|F_o|$ is the observed structure factor amplitude and $|F_c|$ is the calculated structure factor amplitude.

[f] R_{free} = R-factor based on 4.9% of the data excluded from refinement.

[g] Twin operation is (h, k, l), (-h, -k, l), (-1/2*h-3/2*k, -1/2*h+1/2*k, -l), (-1/2*h+3/2*k, 1/2*h+1/2*k, -l), (1/2*h+3/2*k, 1/2*h-1/2*k, -l), and (1/2*h-3/2*k, -1/2*h-1/2*k, -l), in order. Twin fractions were calculated by *REFMAC5* (Vagin, et al., 2004, Acta Crystallogr D Biol Crystallogr, 42)in the *CCP4i* software suite (Winn, et al., 2011, Acta Crystallogr D Biol Crystallogr, 43).

[h] the twin operation is (h, k, l) and (-k, -h, -l), in order. Twin fractions were calculated by *REFMAC5* (Vagin, et al., 2004, Acta Crystallogr D Biol Crystallogr, 42)in the *CCP4i* software suite (Winn, et al., 2011, Acta Crystallogr D Biol Crystallogr, 43).

2.5. Size exclusion chromatography with multi-angle light scattering (SEC-MALS) analysis

SEC-MALS was implemented with an FPLC machine (GE Healthcare, Chicago, IL, USA) connected to a Wyatt MiniDAWN TREOS MALS instrument and a Wyatt Optilab rEX differential refractometer (Wyatt Technology, Santa Barbara, CA, USA). A HiLoad^{TM} 10/300 Superdex 200 GL (GE Healthcare, Chicago, IL, USA) column was pre-equilibrated with a buffer containing 20 mM Tris-HCl (pH 7.5), 150 mM sodium chloride, and 0.5 mM TCEP, and was normalized using ovalbumin. 100 μL of monomer and dimer NDRG3 WT at 2.0 mg/mL were injected into the machine at flow rate of 0.4 mL/min, respectively. Data were analyzed using the Zimm model for fitting static light-scattering data and graphed using EASI graph with a UV peak in the ASTRA V software (Wyatt Technology, Santa Barbara, CA, USA).

2.6. Circular Dichroism (CD)

CD spectroscopy was implemented with the Chiranscan^{TM}-plus CD Spectrometer (Applied photophysics Ltd., Surrey, UK) at 298 K with a wavelength range from 260 nm to 180 nm. NDRG3, NDRG3 mutants, and NDRG2 proteins were diluted to 0.4 mg/mL with a buffer containing 20 mM potassium phosphate dibasic (pH 7.5) and 50 mM sodium fluoride. The maximum absorbances in CD wavelength were adjusted to have ranges from 0.80 to 0.85. The bandwidth was 1.5 nm and the time per point value was 0.5. The temperature was set to 298 K.

2.7. Surface Plasmon Resonance (SPR)

The *in vitro* binding assays of NDRG3 and NDRG2 against $_{L}$-lactate was evaluated by SPR. SPR binding assays were performed using a carboxymethyl dextran (CM5) sensor chip on a Biacore T200 instrument (GE Healthcare, Chicago, IL, USA). Protein immobilization on sensor chip was performed using the amine coupling at a flow rate of 5 μL/min. The chip was activated with a mixture of N-hydroxysuccinimide and N-(3-Dimethylaminopropyl)-N'-ethylcarbodiimide hydrochloride at a ratio of 1:1 for 400 s. Then, 0.1 mg/mL NDRG3 and NDRG2 were diluted in 10 mM sodium acetate (pH 5.5) and injected until the immobilization level reached at 15,000 RU. The surfaces of the chip were blocked by 1000 mM ethanolamine (pH 8.5). The multi-cycle analysis was performed at a flow rate of 30 μL/min. $_{L}$-lactate at different concentrations of 3.13, 6.25, 12.50, 25.00, and 50.00 mM, were injected over the chip for 120 s, followed by dissociation for 600 s in a separate analysis cycle. The binding assay was

implemented in a buffer containing 150 mM NaCl, 10 mM HEPES-NaOH (pH 7.2), 3 mM ethylenediaminetetraacetic acid (EDTA), and 0.001% polysorbate 20. The sensor chip surface was regenerated with 5 mM NaOH between each cycle. The equilibrium dissociation constant (K_D) was determined using Biacore T200 evaluation software 3.0 (GE Healthcare, Chicago, IL, USA).

2.8. Molecular dynamics and docking study

Molecular dynamics were implemented using *VMD 1.9.2* software (Phillips, et al., 2005, J Comput Chem, 48) followed by *NAMD 2.13* software (Humphrey, et al., 1996, J Mol Graph, 49). Coordinates of NDRG3 C30S was used as template of molecular dynamics. The molecular dynamics system was solvated using water molecules and energy of the system was minimized in order to remove steric clashes. Minimization was performed using steepest descent and conjugate gradient algorithms for 1000 steps for each system. Temperature was set to 298 K with pressure 1 atm for 10 picosecond. Same conditions were applied for 100 picoseconds using a canonical (NVT) ensemble. The cutoff value for non-bonding interactions was set to 8.0 Å. Among 1000 resulting trajectories, 21 coordinates of trajectories in every 50 steps were used for docking simulation against $_L$-lactate. Coordinates for the $_L$-lactate were generated using *ChemDraw V13* software (PerkinElmer). *PatchDock* web-server (Schneidman-Duhovny, et al., 2005, Nucleic Acids Res, 50) followed by *FireDock* (Mashiach, et al., 2008, Nucleic Acids Res, 51) web-server was used for computational docking prediction with protein and compound as receptor and ligand, respectively.

2.9. Data deposition

Coordinates and structure factors of NDRG3 and NDRG3 mutants are deposited in the Protein Data Bank (http://www.rcsb.org) under accession codes 6L4B (NDRG3), 6L4G (I171M/S176H mutant), and 6L4H (C30S mutant) , respectively.

3. Results

− Chapter 1. Structural studies on NDRG3 −

3.1. Overall structure of human NDRG3 contains an α/β-hydrolase fold domain and a small cap-like domain.

The human NDRG3 protein (375 amino acids) was predicted to contain flexible N− and C−terminal regions by the *Xtalpred* server (http://ffas.burnham.org/XtalPred−cgi/xtal.pl) (Slabinski, et al., 2007, Bioinformatics, 52) (Figure 19). Additionally, the known post−translational modification (PTM) data from the *PhosphoSite Plus* database (https://www.phosphosite.org) (Hornbeck, et al., 2015, Nucleic Acids Res, 53) indicated that the C−terminus of NDRG3 contains numerous phosphorylation sites, suggesting that the C−terminal region is highly dynamic (Figure 20). Therefore, a truncated construct (residues 29–320) with an N−terminal hexahistidine tag was designed and crystallized. The NDRG3 structure was determined at 2.2 Å resolution using the molecular replacement method with the crystal structure of human NDRG2b (PDB ID: 2XMQ) as a phasing model, that shares 55.0% sequence identity (Hwang, et al., 2011, J Biol Chem, 40). The NDRG3 crystal contains six monomers in an asymmetric unit (ASU), and belongs to space group *C*2 (Figure 21). The NDRG3 structure includes two domains: a canonical α/β−hydrolase fold domain and a small cap−like domain. The α/β−hydrolase fold domain consists of an eight−stranded β−sheet and eight α−helices (α1−α5 and α11−α13). The β−hairpin structure (β1 and β2) is exposed to the surface,

while six parallel β-strands (from β3 to β8) are surrounded by α-helices (Figure 22). The small cap-like domain (from Ala167 to Arg233) contains a disordered region and four helices (α7-α10), which compactly cover the α/β-hydrolase fold by interacting with four loops. The disordered region in the small cap-like domain (from Trp173 to Leu182) is sequentially matched to the helix α6 region in NDRG2b (Figure 23). Although I could not model the region (from Trp173 to Leu182), I will designate the disordered region as the helix α6 region in accordance with the secondary structure of NDRG2b for the sake of convenience. When I compared root-mean-square deviations (r.m.s.d.) distances of C_α atoms of each subunit compared with chain A as a reference, overall subunits were structurally similar and the helix α6 region is disordered in all the subunits. Interestingly, helix α8 of chain D, E, and F were structurally different from that of chain A. In the crystal packing of NDRG3, helix α8 of chain D, E, and F were influenced by adjacent molecules while that of chain A, B, and C were away from adjacent molecules. Therefore, the crystal structure of chain A, B, and C of NDRG3 seems to represent the structure of NDRG3 in solution than that of chain D, E, and F (Figure 24).

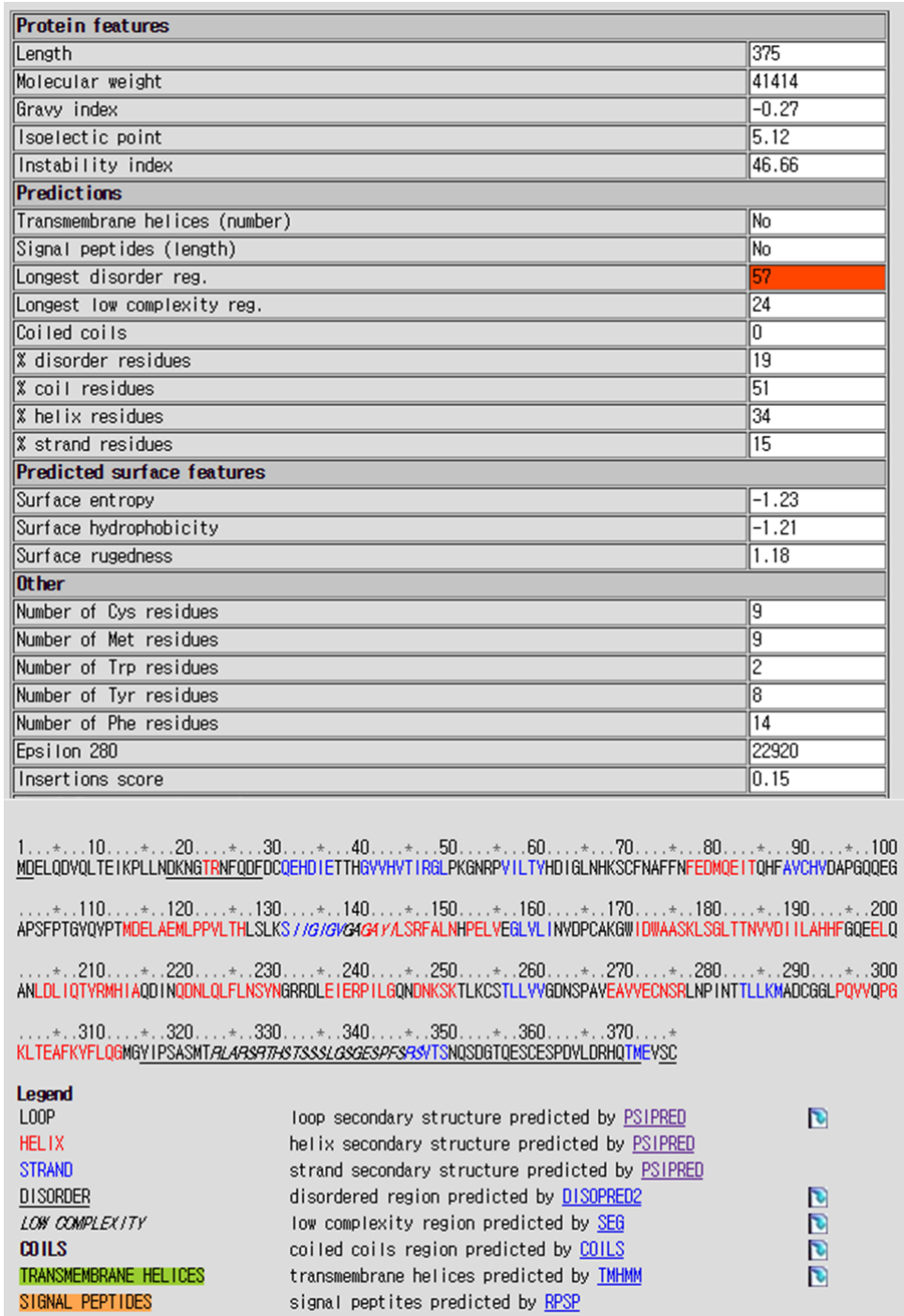

Protein features	
Length	375
Molecular weight	41414
Gravy index	-0.27
Isoelectic point	5.12
Instability index	46.66
Predictions	
Transmembrane helices (number)	No
Signal peptides (length)	No
Longest disorder reg.	57
Longest low complexity reg.	24
Coiled coils	0
% disorder residues	19
% coil residues	51
% helix residues	34
% strand residues	15
Predicted surface features	
Surface entropy	-1.23
Surface hydrophobicity	-1.21
Surface rugedness	1.18
Other	
Number of Cys residues	9
Number of Met residues	9
Number of Trp residues	2
Number of Tyr residues	8
Number of Phe residues	14
Epsilon 280	22920
Insertions score	0.15

Figure 19. Prediction of features and crystallizability of NDRG3 using *Xtalpred* server.

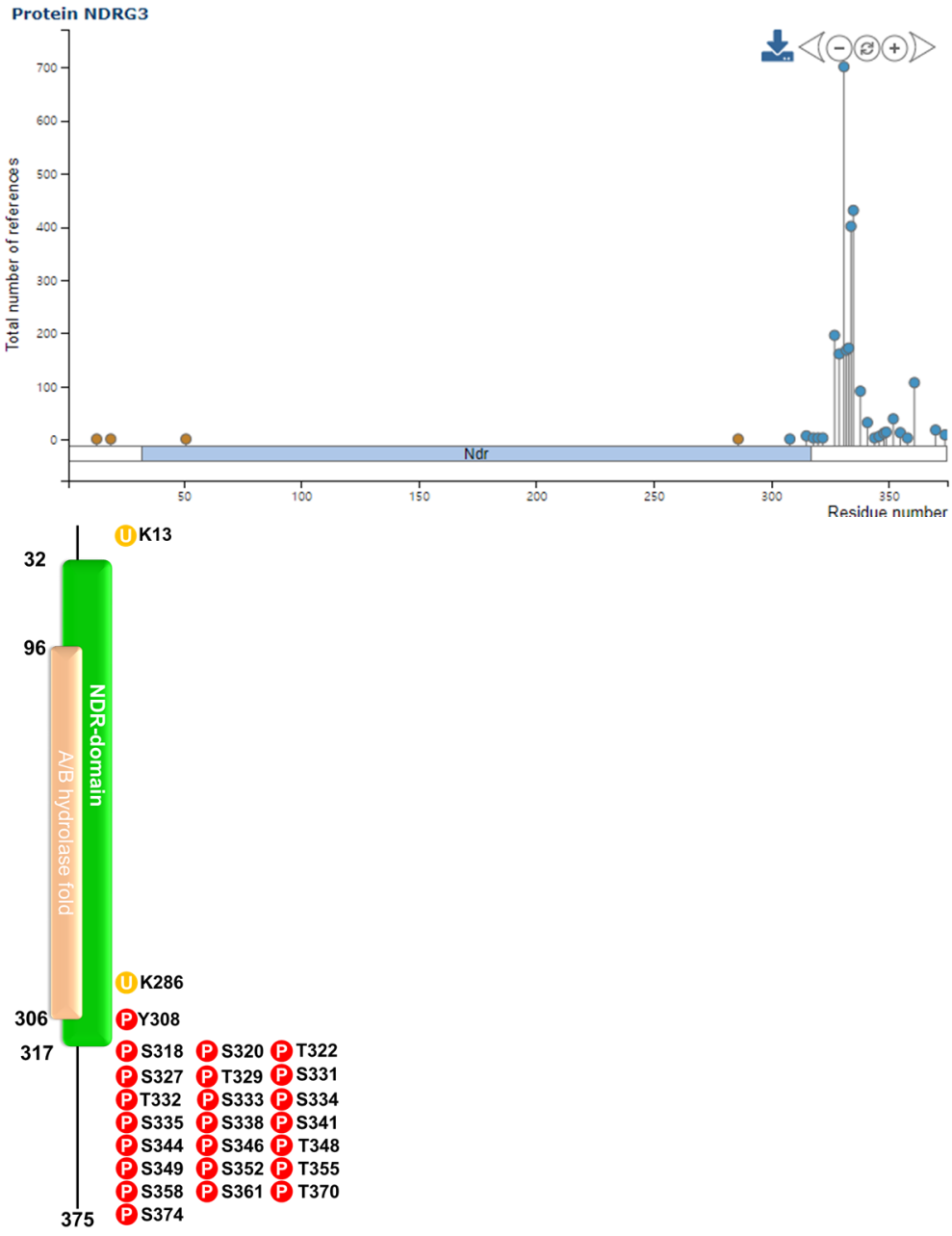

Figure 20. PTM sites on NDRG3 from the *Phosphosite* database.

PTM sites on NDRG3 cite from *Phophosite* database (up). Ubiquitination and phosphorylation sites are represented by yellow and red circles, respectively (down).

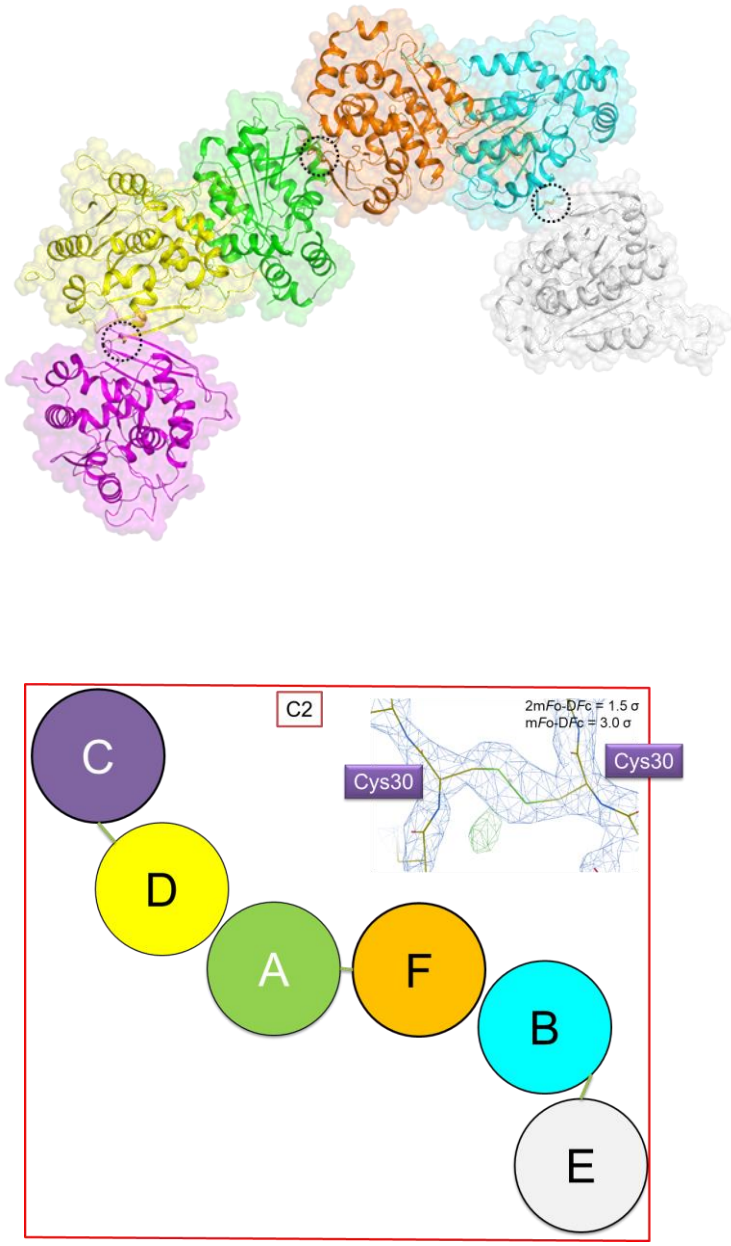

Figure 21. Crystal structure of NDRG3 in ASU.

NDRG3 molecules observed in an asymmetric unit of the crystal. Intermolecular disulfide bonds are shown in stick models and marked with black-dotted circles (up). Diagram of NDRG3 molecules are connected by disulfide bond (down).

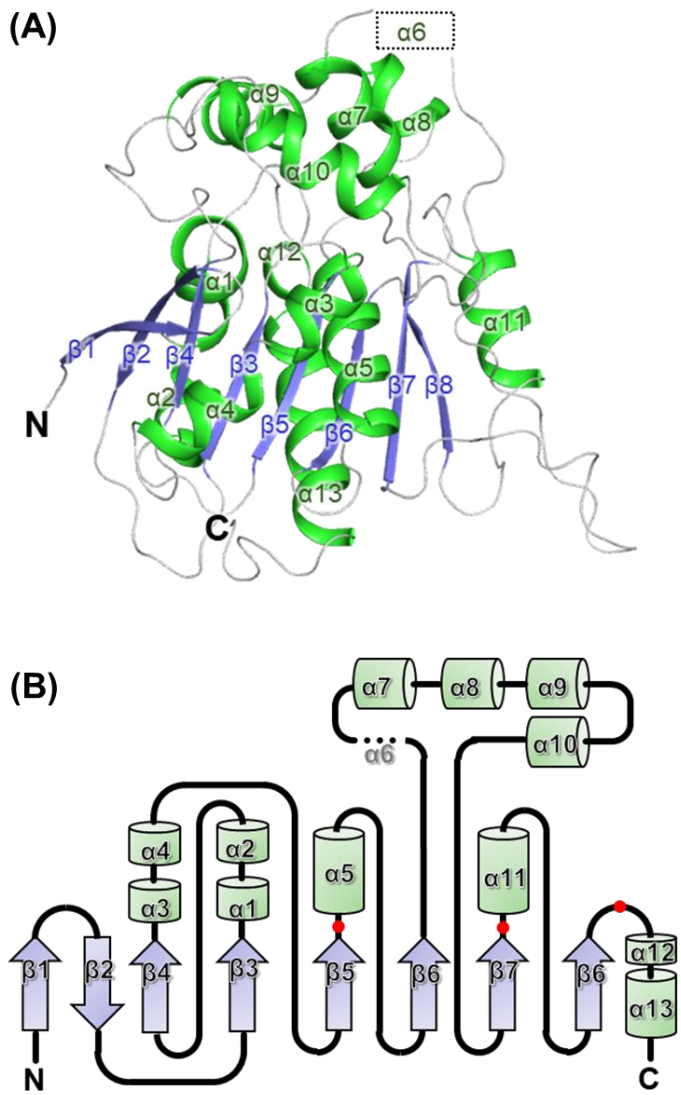

Figure 22. Crystal structure of NDRG3 monomer.

(A) NDRG3 structure is shown in cartoon representation. α-helices, β-strands, and loops are colored in green, blue, and white, respectively. The disordered region corresponding to helix α6 of NDRG2 is shown with a black-dashed box and labeled as the helix α6. (B) Topology diagram of NDRG3. Helices and strands are represented as green cylinder and blue arrow, respectively. The helix α6 region is marked as black dotted line. Red circles indicate the equipositional catalytic triad residues of NDRG3.

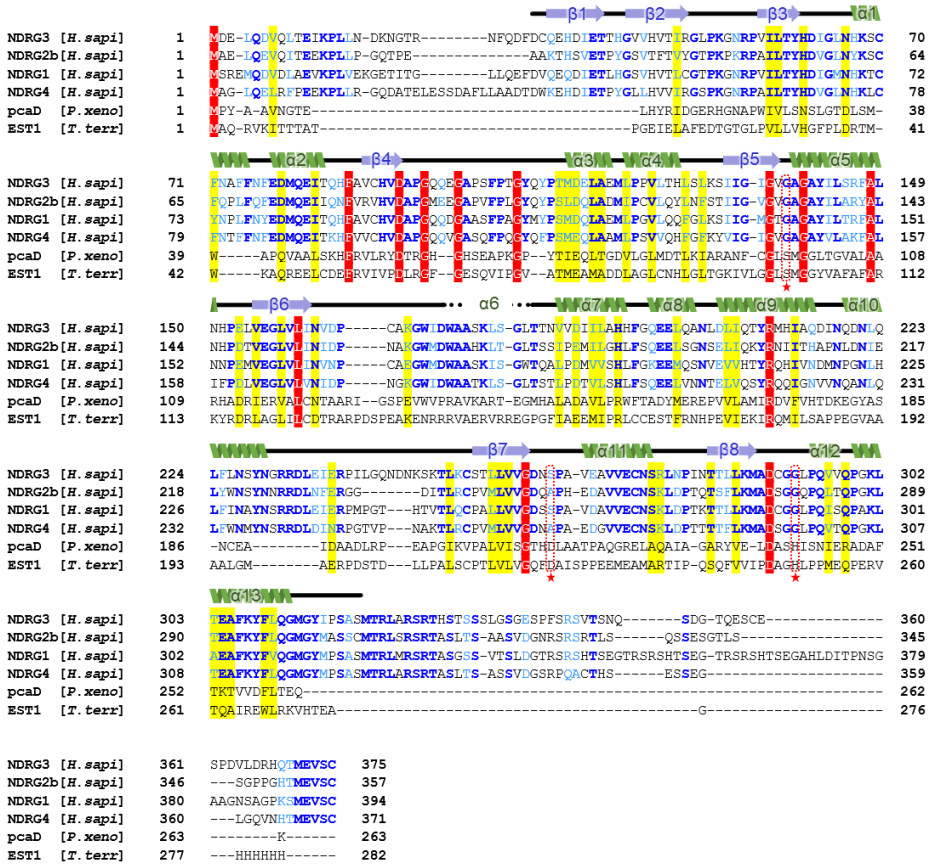

Figure 23. Sequence alignment of NDRG family and α/β-hydrolase fold proteins.

The secondary structure features of NDRG3 are shown at the top of the sequence alignment. The locations of conserved catalytic triad are marked by red asterisks. Strictly conserved residues are highlighted with red-shade boxes, and moderately conserved residues are highlighted with yellow-shaded boxes. Blue and cyan letters represent the identical residues and conserved residues among the NDRG family proteins, respectively. Sequences were aligned using *T-Coffee* web-server (Di Tommaso, et al., 2011, Nucleic Acids Res, 54).

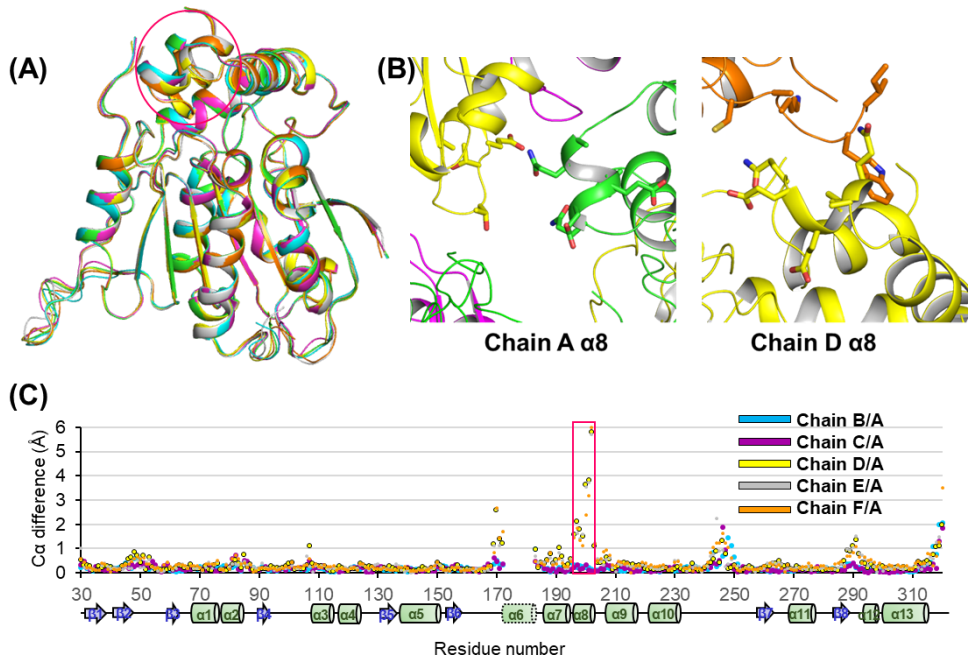

Figure 24. Superimposition of a C_α chain of NDRG3 subunits in ASU.

(A) A red circle indicates helix α8 of NDRG3. The green, cyan, purple, yellow, grey, and orange cartoon models represent chains A, B, C, D, E, and F of NDRG subunits, respectively. (B) A close-up view of the helix α8 region of chain A and D of NDRG3. (C) Structural comparison of C_α distances between chain A of NDRG3 compared with other chains of NDRG3. The secondary structure of NDRG3 is shown at the bottom of the r.m.s.d. distances of C_α atoms.

3.2. Crystal packing of NDRG3 structure indicates dimeric interface.

During purification, NDRG3 (residues 29–320) exists as both monomer and dimer in solution. To date, the NDRG3 dimer has not been reported. To further investigate the oligomeric state of NDRG3 in solution, I implemented size exclusion chromatography with multi–angle light scattering (SEC–MALS). SEC–MALS results indicated that the molecular weight of monomer and dimer fractions of NDRG3 was calculated as 31.4 kDa and 64.1 kDa, respectively (Figure 21). Although the molecular weights are approximately 10% less than predictions, the dimer is stable in solution. In the crystal structure of NDRG3, the crystal contains six molecules connected by disulfide bonds between Cys30–Cys30 in an ASU (Figure 18), whereas it was grown with monomer fractions in purification. Since the SEC–MALS was implemented under a reducing agent, 0.5 mM TCEP, the disulfide bond between Cys30–Cys30 does not seem to contribute forming dimer in solution, but it is a critical interaction for forming crystals. Surprisingly, the crystal structure contains two different dimeric conformations: chain A/D and chain B/F (Figure 22 and 23). Protein, Interfaces, Structures and Assemblies (*PISA*) web–server (Krissinel and Henrick, 2007, J Mol Biol, 55)predicted that the interface between chain B and chain F comprises a similar area (971.5 $Å^2$) as that of the interface between chain A and chain D (999.3 $Å^2$). However, the predicted solvation free energy of the dimeric interface between chain B and chain F was −11.5 kcal/mol, which is more stable than that of chain A and chain D (−4.8 kcal/mol). To clarify the dimeric interface of NDRG3, we mutated Ser255 and Asn281 which are key residues involved in hydrogen bond interactions between chain B/F (Figure 28). After each cells containing NDRG3 wild type (WT) plasmid and S255A/N281A mutant plasmid were overexpressed in a same condition, we compared the ratio of dimer/monomer fractions between NDRG3 WT and S255A/N281A. The dimer fraction of

NDRG3 S255A/N281A was noticeably decreased to 2% out of the total proteins, while the dimer fraction of NDRG3 WT was 12% (Figure 29). Taken all together, these results indicate that NDRG3 forms a dimer, wherein the chain B/F dimer represents dimeric interactions of NDRG3.

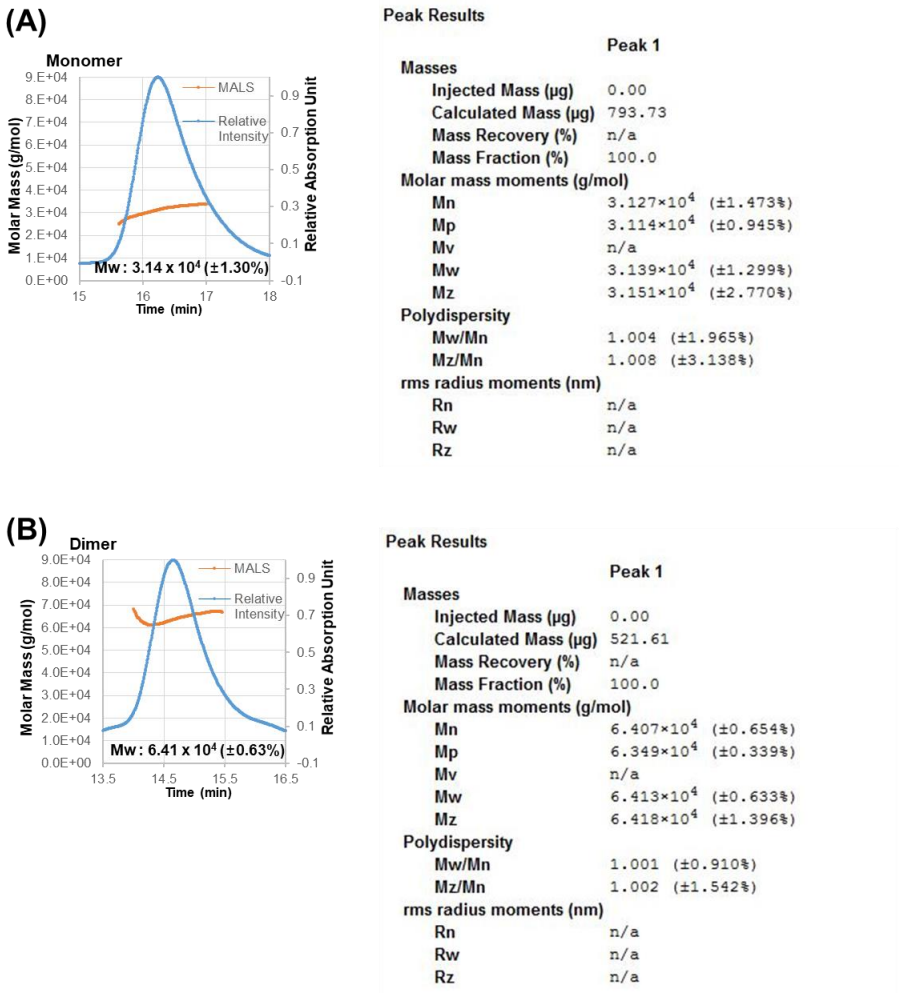

Figure 25. SEC-MALS analyses of the NDRG3 monomer and dimer.

(A) SEC-MALS chromatogram and MALS analyses results of NDRG3 monomer. The blue line indicates the relative absorbance of protein during size exclusion chromatography, and the orange line represents the mass of the molecules analyzed by MALS. (B) SEC-MALS chromatogram and MALS analyses results of NDRG3 dimer. The lines are mapped and denoted as in (A).

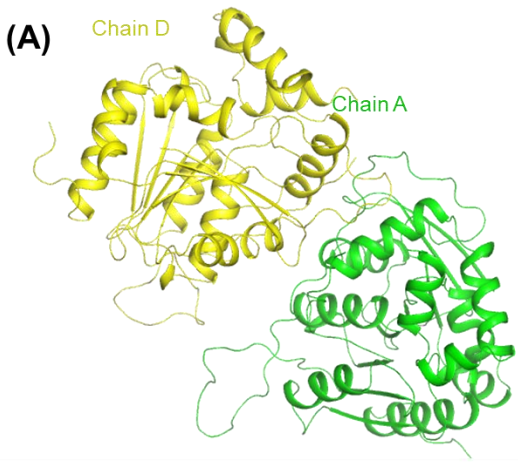

(B) Interface Summary XML

	Structure 1		Structure 2	
Selection range	D		A	
class	Protein		Protein	
symmetry operation	x,y,z		x,y,z	
symmetry ID	1_555		0_555	
Number of atoms				
interface	110	5.0%	104	4.8%
surface	1171	53.5%	1185	54.1%
total	2189	100.0%	2189	100.0%
Number of residues				
interface	29	10.3%	29	10.3%
surface	245	86.9%	247	87.6%
total	282	100.0%	282	100.0%
Solvent-accessible area, Å				
interface	1019.9	7.9%	977.3	7.5%
total	12990.3	100.0%	13097.8	100.0%
Solvation energy, kcal/mol				
isolated structure	-270.8	100.0%	-269.8	100.0%
gain on complex formation	-3.0	1.1%	-1.1	0.4%
average gain	-2.6	1.0%	-2.7	1.0%
P-value	0.461		0.704	

Figure 26. Dimeric interface of NDRG3 A/D dimer in crystal structure.

(A) A dimeric conformation of chain A and chain D in an ASU is represented as cartoon model. (B) Dimeric interface summary are analyzed by *PISA* web-server.

(A)

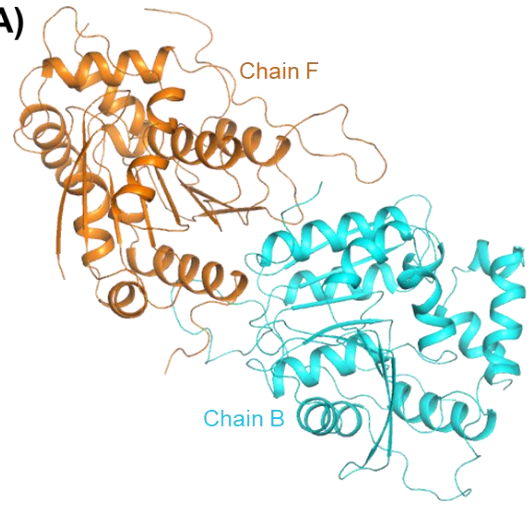

(B) Interface Summary XML

	Structure 1		Structure 2	
Selection range	F		B	
class	Protein		Protein	
symmetry operation	x,y,z		x,y,z	
symmetry ID	1_555		0_555	
Number of atoms				
interface	114	5.2%	111	5.1%
surface	1189	54.3%	1181	54.0%
total	2189	100.0%	2189	100.0%
Number of residues				
interface	33	11.7%	32	11.3%
surface	253	89.7%	252	89.4%
total	282	100.0%	282	100.0%
Solvent-accessible area, Å				
interface	961.8	7.4%	964.6	7.4%
total	13055.6	100.0%	13046.4	100.0%
Solvation energy, kcal/mol				
isolated structure	-269.9	100.0%	-269.1	100.0%
gain on complex formation	-5.4	2.0%	-5.9	2.2%
average gain	-3.0	1.1%	-2.9	1.1%
P-value	0.219		0.156	

Figure 27. Dimeric interface of NDRG3 B/F dimer in crystal structure.

(A) A dimeric conformation of chain B and chain F in an ASU is represented as cartoon model. (B) Dimeric interface summary are analyzed by *PISA* web-server.

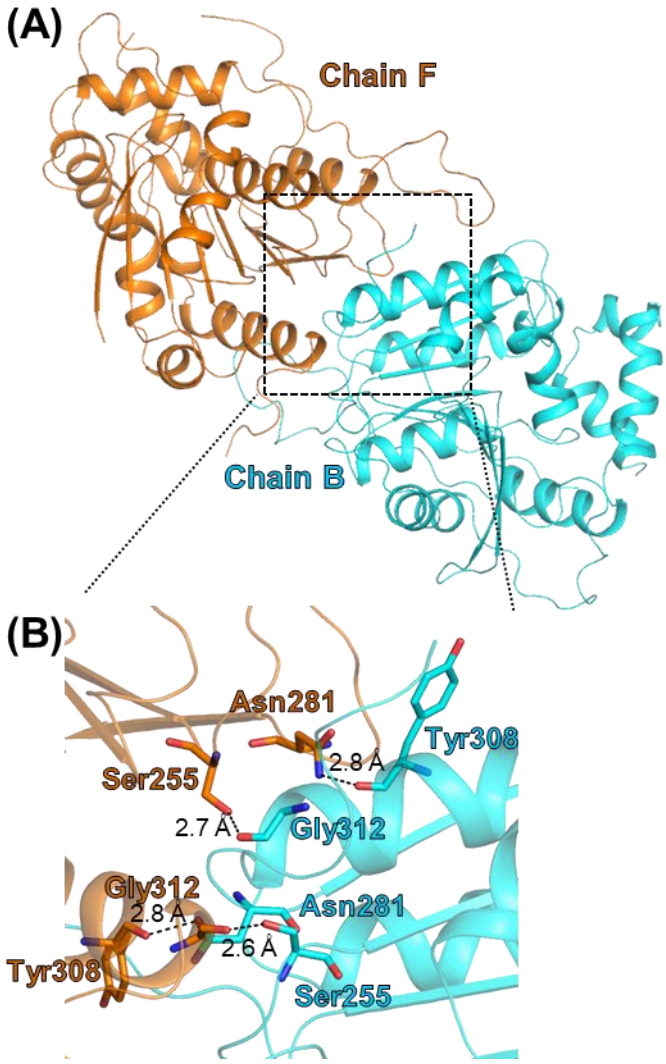

Figure 28. A close-up view of hydrogen bonds between chain B and chain F.

(A) Dimeric interactions of chain B and chain F in an ASU. (B) Residues involved in hydrogen bonding were shown in stick models with labels.

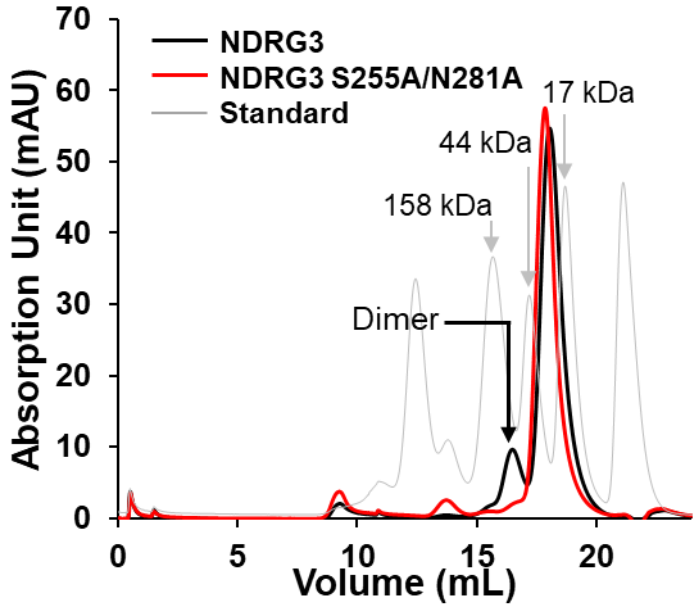

Figure 29. Chromatograms of NDRG3 and S255A/N281A from analytical size exclusion chromatography.

The black and red chromatograms represent profiles of NDRG3 WT and NDRG3 S255A/N281A, respectively. The grey chromatogram indicates a gel filtration standard profile (Bio-Rad #1511901, Hercules, CA, USA).

3.3. Structural comparison with α/β-hydrolase supports loss of enzymatic function in NDRG3.

To gain an insight into structural features of NDRG3, I analyzed the structural similarities using *DALI* web-server (Holm and Laakso, 2016, Nucleic Acids Res, 56). The results showed that the structure of NDRG3 is similar to α/β-hydrolase fold superfamily. With the exception of NDRG2 structures, NDRG3 shares a high similarity with α/β-hydrolases marked with Z score 9.5-26.9, whereas the amino acid sequence alignment shows a low similarity (7-20%) (Table 3). When comparing the structure of NDRG3 to the closest structural homologs, pcaD enol-lactonase from Paraburkholderia xenovorans (PDB ID: 2XUA, Z score: 26.7, sequence identity: 15.6%) and malate complexed esterase (EST) from Thermogutta terrifontis (PDB ID: 4UHE, Z score = 26.2, sequence identity = 18.5%), the overall structure of NDRG3 was superposed to the α/β-hydrolases with root-mean-square deviations (r.m.s.d.) of equipositional C_α atoms at 2.8 Å and 2.9 Å, respectively (Figure 30A). However, the residues of canonical catalytic triad sites of α/β-hydrolase family: nucleophile-acid-histidine, are substituted by non-catalytic residues in NDRG3 (Figure 30B). The nucleophile residue is substituted by Gly138 of NDRG3, which is located on the end of helix α5. His244 of pcaD and His250 of EST are superposed to Gly292 of NDRG3, and Asp217 of pcaD and Asp222 of EST which account for acidic residue of catalytic triad are substituted to Ser264 of NDRG3, respectively. Especially, α/β-hydrolase proteins possess a large pocket and helices on the small cap-like domain do not hinder substrate binding site. Helices α7 and α10 on NDRG3 were closer to pseudo-active site, with a 16.1° and 3.5° angle differences compared with those of pcaD, respectively, and with a 10.3° and 8.2° angle differences to those of EST, respectively. In addition, helix α7, helix α10, and Ile63 in the pseudo-active site of NDRG3, induce a hydrophobic effect, result in helix α7 found near Ile63. In

contrast, Ile63 is substituted to bulky residues, Leu35 of pcaD and Phe35 of EST, respectively, pushing out helix α7. Moreover, due to a hydrogen bond between Nτ atom of His192 on helix α7 and oxygen atom of Asp62, as well as an aromatic phi-phi interaction between Tyr229 on helix α10 and Arg232, the entrance of the pseudo-active site is occupied by bulky residues, His192 and Tyr229, that form a narrow cleft in NDRG3. When I superposed coordinates of substrates of pcaD and EST, His192 on helix α7 and Tyr229 on helix α10 in NDRG3 were found to collide with the substrates (Figure 31). Therefore, it seems plausible that the small cap-like domain of NDRG3 disrupts the substrate binding site compared with that of α/β-hydrolase proteins. Structural differences between NDRG3 and α/β-hydrolase proteins demonstrated that NDRG3 abolishes its hydrolase function by substituting its catalytic triad into non-catalytic residues, and also effectively blocking the binding path of substrates.

Table 3. Top 20 structurally similar candidates of NDRG3 analyzed by *DALI*.

No.	Chain	Z-score	r.m.s.d.	% seq. identity	Description
1	2xmq-A	42.4	1.3	61	NDRG2;
2	3om8-B	27.1	2.9	19	PROBABLE HYDROLASE;
3	2xua-H	26.7	2.8	13	3-OXOADIPATE ENOL-LACTONASE;
4	4uhc-A	26.1	2.9	20	ESTERASE;
5	5egn-A	26.1	3	15	ESTERASE;
6	5h3h-B	26	2.9	15	ABHYDROLASE DOMAIN-CONTAINING PROTEIN;
7	1wom-A	25.4	2.6	17	SIGMA FACTOR SIGB REGULATION PROTEIN RSBQ;
8	5frd-A	25.1	2.9	17	CARBOXYLESTERASE (EST-2);
9	6eb3-B	25.1	3.4	14	EST1;
10	4dgq-A	24.7	2.8	16	NON-HEME CHLOROPEROXIDASE;
11	3fob-A	24.5	2.9	14	BROMOPEROXIDASE;
12	4qes-A	24.5	3.1	12	NON-HAEM BROMOPEROXIDASE BPO-A2, MATRIX PROTEIN 1
13	5a62-A	24.5	2.7	16	PUTATIVE ALPHA/BETA HYDROLASE FOLD PROTEIN;
14	3qvm-B	24.3	2.8	15	OLEI00960;
15	1va4-A	24.2	2.8	16	ARYLESTERASE;
16	1a8q-A	24.2	2.9	14	BROMOPEROXIDASE A1;
17	3v48-A	24.1	3.2	13	PUTATIVE AMINOACRYLATE HYDROLASE RUTD;
18	4q3l-B	23.8	2.7	19	MGS-M2;
19	1u2e-A	23.6	3.2	19	2-HYDROXY-6-KETONONA-2,4-DIENEDIOIC ACID
20	2xmz-A	23.5	2.7	17	HYDROLASE, ALPHA/BETA HYDROLASE FOLD FAMILY;

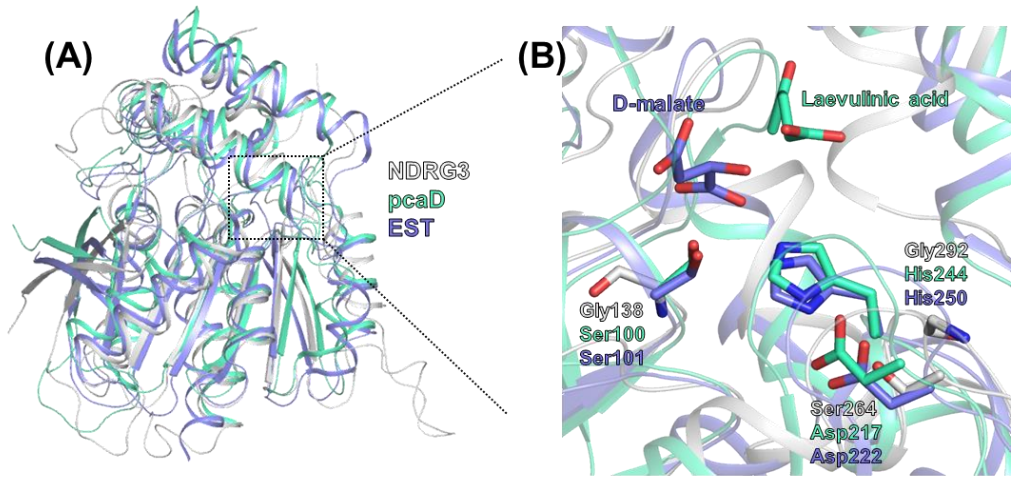

Figure 30. Structural comparison between NDRG3 and its structural homologs, pcaD and EST.

(A) Superimposition of C_α chain of NDRG3, pcaD, and EST. Structures of NDRG3, pcaD, and EST are represented as white, cyan, and blue cartoon models, respectively. (B) A close-up view of catalytic active site of α/β-hydrolase proteins. NDRG3, pcaD, and EST proteins are shown in white, cyan, and blue, respectively. Catalytic triads and substrates are represented as stick models.

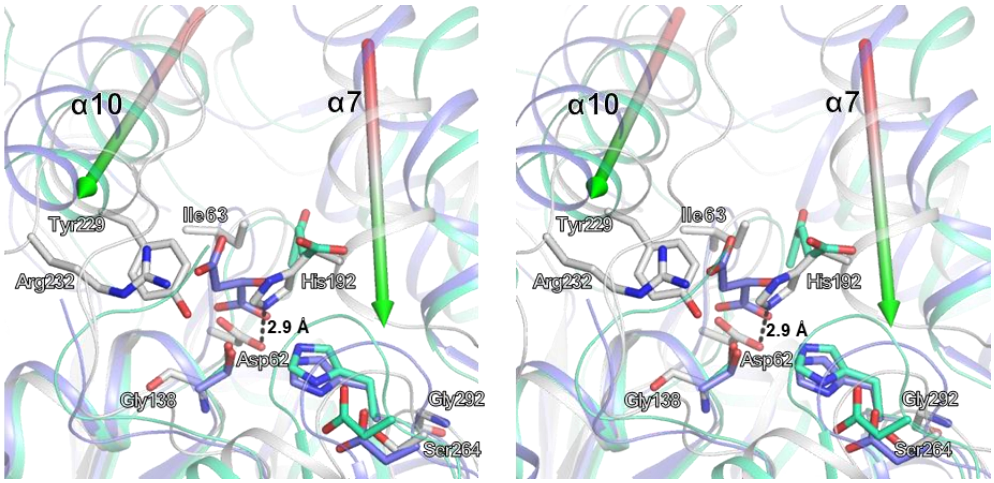

Figure 31. A stereo-view image of active site of NDRG3.

The residues on active sites are mapped and denoted as in Figure 24B. Arrows indicate the direction of each helix. Structural comparison between NDRG3 and its structural homologs, pcaD and EST. Dimeric conformation of NDRG3 B/F dimer in crystal structure.

3.4. NDRG3 shows a structural similarity to NDRG2 and contains a distinctive disordered region and a solvent accessible cavity.

The first structure determined among the NDRG family proteins, NDRG2, shares a high sequential and structural similarity to NDRG3 (Figure 23 and 32). However, there are two regions which show distinctive differences between NDRG2 and NDRG3: the helix $\alpha 6$ region of NDRG2 (Figure 33) and the loop region between helix $\alpha 10$ and $\beta 7$ (Figure 34). While the equivalent region of $\alpha/\beta-$ hydrolase proteins, pcaD, and EST, adopts a helical structure between helix $\alpha 10$ and $\beta 7$, it is found as a loop in the structure of NDRG2 and NDRG3. The loop of NDRG2 is composed of charged residues, such that it is exposed to surface, wherein two glycines (Gly234 and Gly235) seem to be critical for formation of the loop. The loop of NDRG3 between Gly231 and Ser255 is longer than that of NDRG2 by seven residues, and highly dynamic in that the r.m.s.d. values of C_α atoms in the loop region are noticeably higher than the average r.m.s.d. values for all C_α atoms, compared with chain A as a reference (Figure 24).

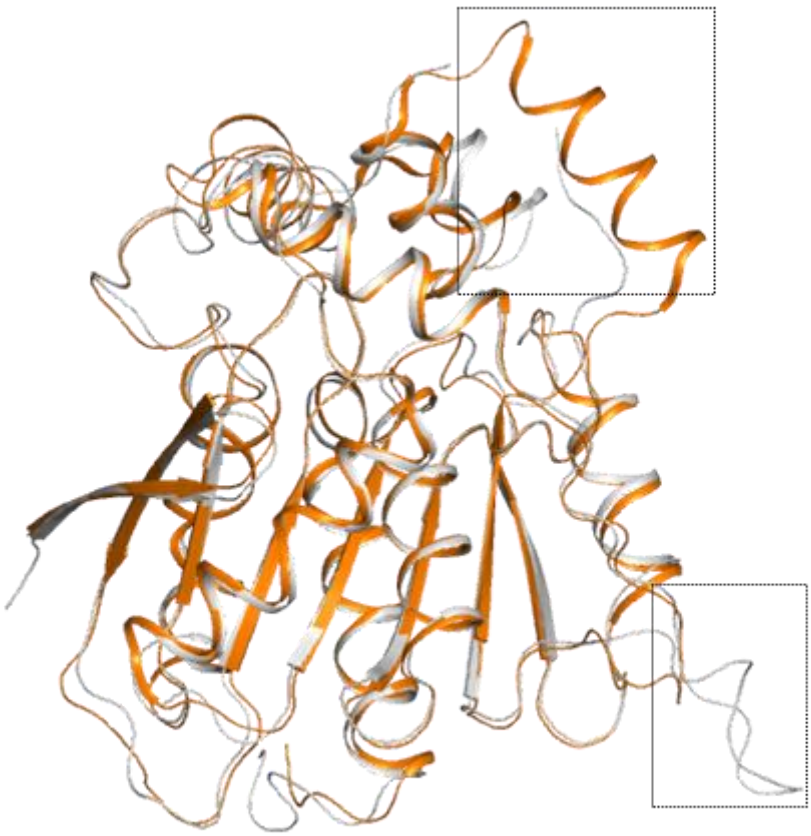

Figure 32. Structural comparison between NDRG3 and NDRG2.

Overall view of superimposition of NDRG3 and NDRG2. NDRG3 and NDRG2 structures are represented as white and orange cartoon models, respectively. The distinctive difference regions are marked by black-dotted box.

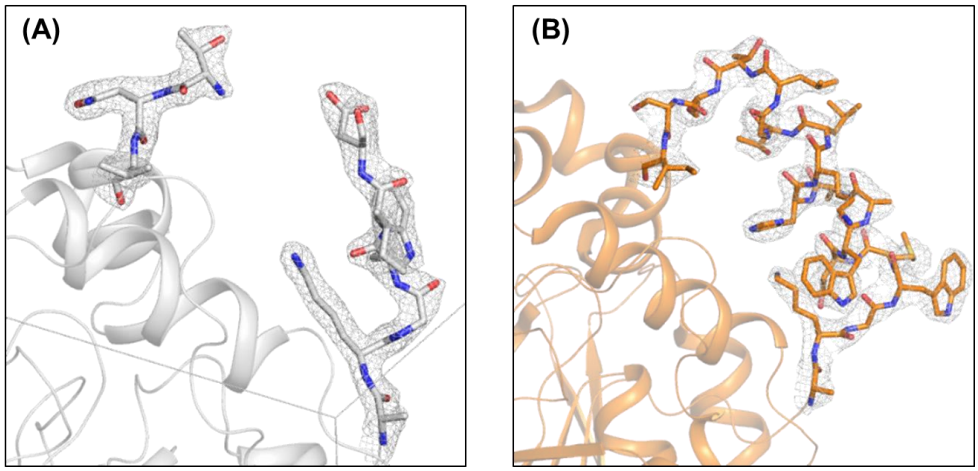

Figure 33. Structural comparison of helix α6 region in NDRG3 and NDRG2.

Electron density map of helix α6 region in NDRG3 and NDRG2. NDRG3 is represented as a white stick model and NDRG2 is represented as an orange stick model, respectively. The 2mF_o−DF_c electron density map contoured at 1.5σ is represented as a grey−colored mesh.

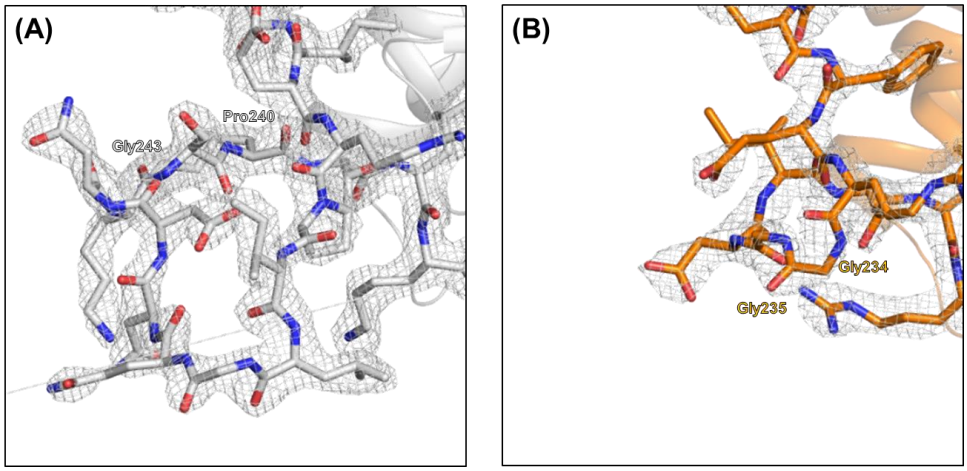

Figure 34. Structural comparison of loop region between helix α 10 and β 7 in NDRG3 and NDRG2.

Electron density map of loop region between helix α 10 and β 7 in NDRG3 and NDRG2. NDRG3 is represented as a white stick model and NDRG2 is represented as an orange stick model, respectively. The 2mF_o−DF_c electron density map contoured at 1.5 σ is represented as a grey−colored mesh.

To further investigate the structural difference between NDRG2 and NDRG3, I compared the r.m.s.d. of C_α atoms between NDRG2 and NDRG3 (Figure 35). Although they share a high structural similarity with 0.92 Å deviation, helix α9 on NDRG3 exhibits a large conformational change by tilting at a 16.0° angle difference compared with NDRG2 (Figure 36A). The C-terminal sequence of helix α9 (red box A in Figure 35), "MHIAQ", of NDRG3 is aligned to "NIITH" of NDRG2, and helix α9 is an amphipathic helix. In helix α9 of NDRG3, His212 interacted with Asp216 through a hydrogen bond, and the hydrogen bond dragged helix α9 to helix α1. On the other hand, His212 is substituted by Ile206 in NDRG2 which resulted in its being unable to form a hydrogen bond with Ala210. As such, helix α9 in NDRG2 appeared closer to helix α7 than in NDRG3, due to this hydrophobic effect. Moreover, the location of Asn263 is a remarkable point in comparison in terms of the r.m.s.d. of C_α from NDRG2 (Figure 35). Asn263 of NDRG3 was found near to loop between β8 and helix α12, forming a hydrogen bond with the main chain of Cys290. On the other hand, Gln250, the corresponding residue in NDRG2, faces to helix α11 and interacts with Glu254 via hydrogen bonding (Figure 36B). Because the Glu254 is substituted to Val267 in NDRG3, Asn263 is unable to interact with helix α10, resulting in the loop between helix α10 and strand β7 bending towards helix α11.

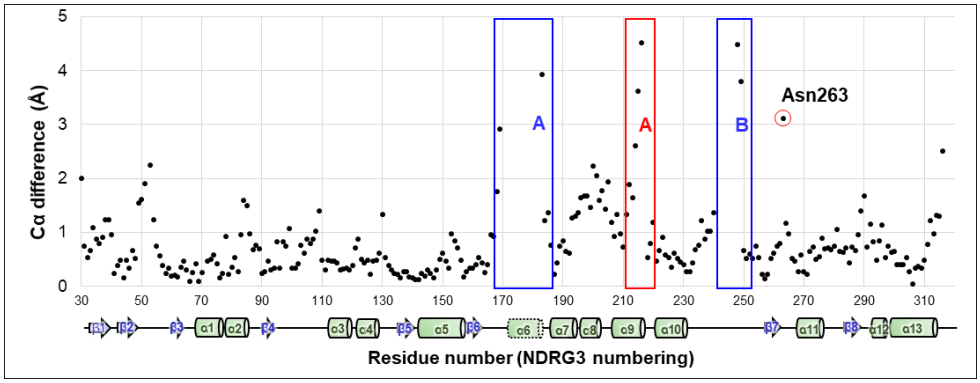

Figure 35. Structural comparison of C_α distances between NDRG3 and NDRG2.

The secondary structure of NDRG3 is shown at the bottom of the r.m.s.d. comparison. The blue box A denotes the helix $\alpha 6$ region; blue box B denotes the loop region between helix $\alpha 10$ and $\beta 7$. The red box A indicates helix $\alpha 9$; the red circle denotes Asn263 on NDRG3.

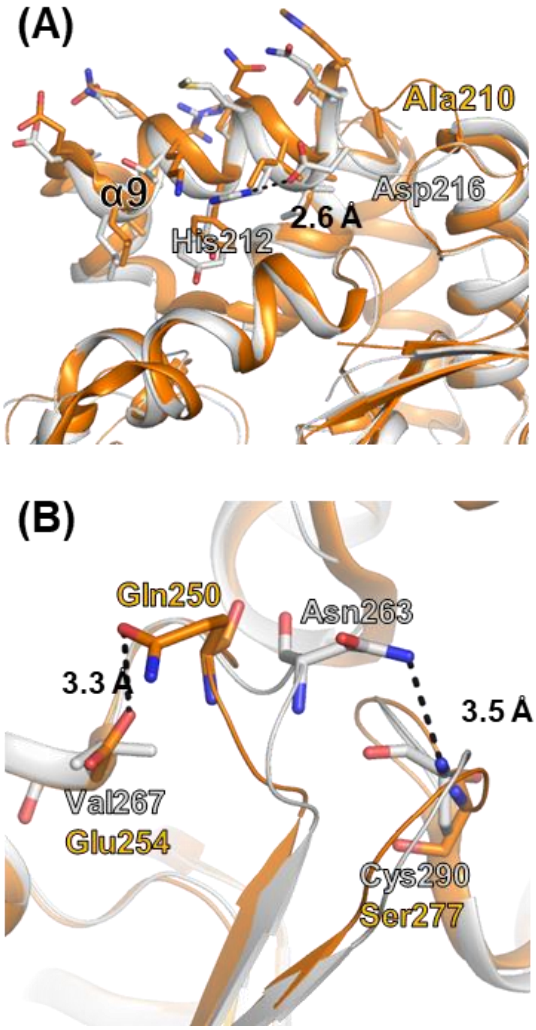

Figure 36. Structural comparison between NDRG3 and NDRG2 in detail.

(A) A close-up view of helix α9 region which are marked as red box A in Figure 35. White and orange cartoon model represent NDRG3 and NDRG2, respectively. Side chains of residue on helix α9 region are shown as stick model. (B) A close-up view of red circle in Figure 35. on which residues are mapped and colored as in (A).

Lastly, His253 located on the loop between strand $\beta 7$ and helix $\alpha 11$ in NDRG2 blocks the pocket of the pseudo-active site. By contrast, this residue in NDRG3 is substituted to Ala266, creating a passage to the pseudo-active site (Figure 37). When I calculated the surface area of the pseudo-active site of NDRG2 and NDRG3 using *KVFinder* (Oliveira, et al., 2014, BMC Bioinformatics, 57), they were found to share a similar volume, with a surface area of 1694.9 $Å^2$ and 1674.2 $Å^2$, respectively. However, they showed a remarkable difference in regards to their solvent accessible surface area, which was 236.2 $Å^2$ and 352.8 $Å^2$, respectively. Substituting Ala266 of NDRG3 to His increased the surface area to 1715.3 $Å^2$, however, the solvent accessible area was reduced to 296.7 $Å^2$. Thus, Ala266 is a key residue for serving accessibility at the pseudo-active site compared with NDRG2. Crystal structures of NDRG2 possesses 3-4 water molecules in the pseudo-active site, His253 on NDRG2 does not block the water accessibility on the pseudo-active site. However, ligand larger than water molecule would be blocked by His253 of NDRG2.

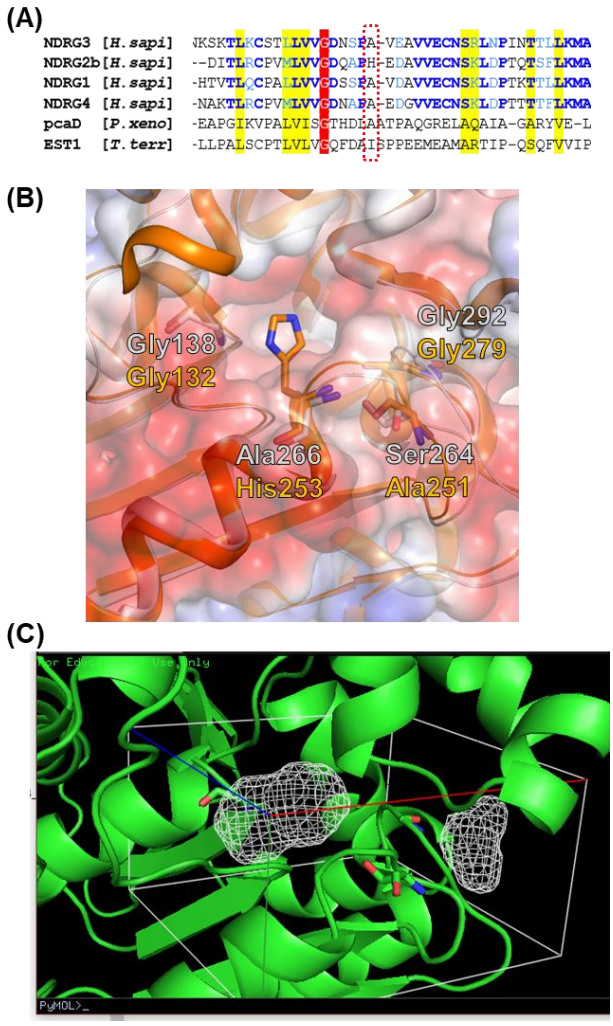

Figure 37. Structural comparison of pseudo-active site in NDRG3 and NDRG2 in detail.

(A) Sequential comparison among NDRG3 isoforms, pcaD, and EST. Ala266 and its equipositional residues are marked by red-dotted circle. (B) Electrostatic potential surface of pseudo-active site of NDRG3. Negatively and positively charged surfaces are represented as red and blue shade, respectively. White sticks represent the catalytic triad and surface entrance residue of NDRG3 and orange sticks represent equipositional residues of NDRG2. (C) Area of pseudo-active site of NDRG3 calculated by *KVfinder*.

3.5. Unfolded helix α6 region of NDRG3 is a flexible loop.

Helix α6 in NDRG2 is known to play a key role in regulating TCF/β-catenin signaling. Interestingly, although NDRG2 and NDRG3 share high similarity in terms of their sequence and structure, the helix α6 region in NDRG3 was disordered, whereas that of NDRG2 was presented as a clear electron density map (Figure 33). In the crystal structure, I suspected that the space between the adjacent molecules is confined and that the helix α6 fold could be disrupted due to the lack of space caused by strong disulfide bonds between each Cys30. To increase the space for the helix α6 region, I designed a disulfide-deficient, denoted as NDRG3 C30S. The crystal structure of NDRG3 C30S mutant was determined with four monomers in an ASU at 3.4 Å resolution (Figure 38). Unexpectedly, when the helix α6 region of chain A was modeled alongside its electron density map, the region was a loop and interacted with chain B (Figure 39). Although the intermolecular interaction of the helix α6 region in the C30S mutant was the result of a crystallographic artefact, the region does not seem to form a helix, based on the crystal structure of C30S mutant (Figure 40). As such, the helix α6 region in NDRG3 is a flexible loop in contrast with that of NDRG2 and α/β-hydrolase proteins

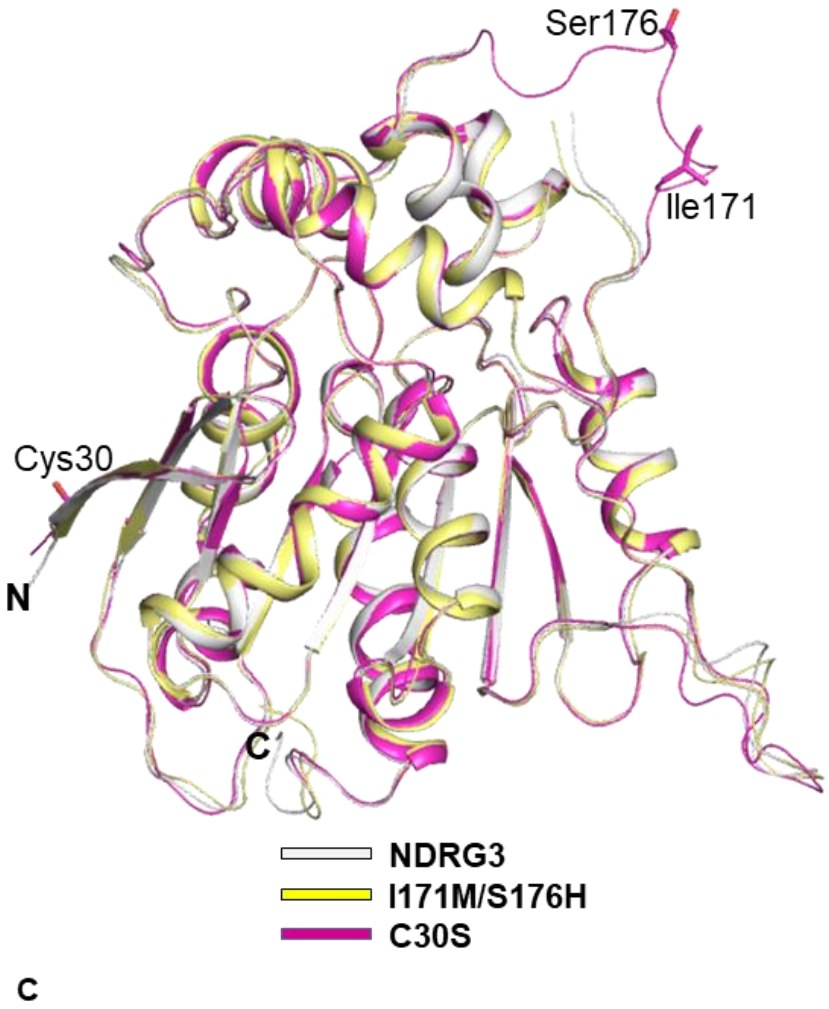

Figure 38. Superimposition of the crystal structures of the NDRG3, NDRG3 I171M/S176H, and NDRG3 C30S.

Structures of NDRG3, NDRG3 I171M/S176H, and NDRG3 C30S are represented as white, yellow, and magenta cartoon models, respectively.

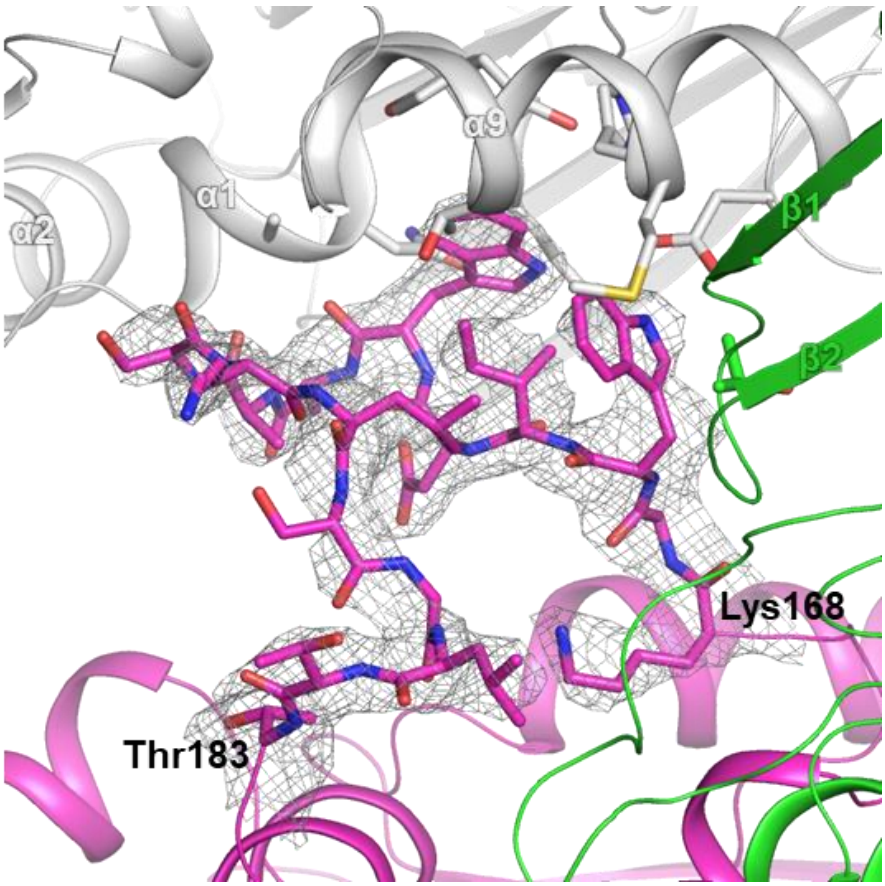

Figure 39. Electron density map of the helix α6 region of NDRG3 C30S mutant.

Chain A is represented as a magenta ribbon and residues on helix α6 region are shown as stick models with an electron density map. Chain B and chain C of NDRG3 C30S are shown in green and white cartoon models, respectively. The 2mFo−DFc electron density map contoured at 1.5 σ is represented as a grey−colored mesh.

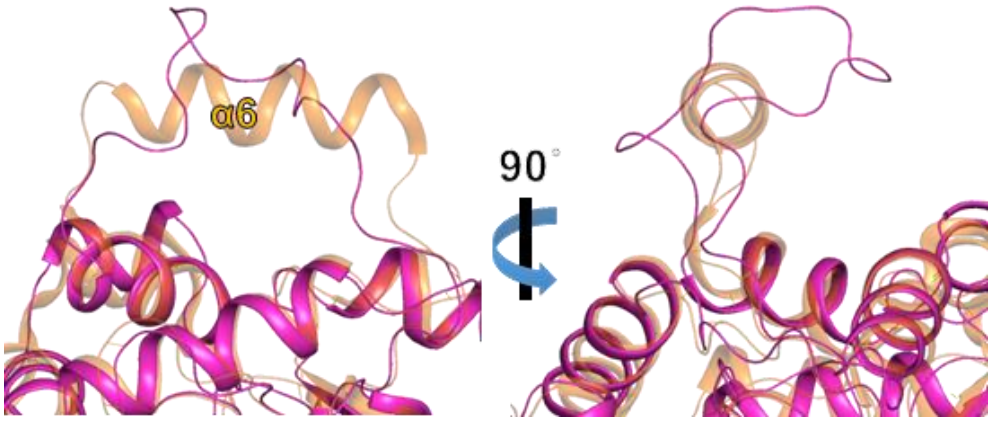

Figure 40. Structural comparison of helix α6 region between NDRG3 C30S and NDRG2.

Structures of NDRG3 C30S and NDRG2 are shown in magenta and orange cartoon models, respectively.

To determine a helical propensity of the residues in the helix, I constructed a helical wheel model using the helix α6 sequence. The helix α6 model of NDRG3 is amphipathic where the electrostatic surface appears to be analogous to that of NDRG2 (Figure 41). Comparing helical propensities of each residue on helix α6 between NDRG3 and NDRG2 (Pace and Scholtz, 1998, Biophys J, 58), Ile171 and Ser176 of NDRG3 overlap with Met165 and His170 of NDRG2, respectively. Based on the helical wheel model, I designed NDRG3 I171M/S176H and C30S/I171M/S176H mutants, which mimicked the helix α6 sequences of NDRG2, and determined the crystal structure of the I171M/S176H mutant at 3.3 Å resolution (Figure 38).

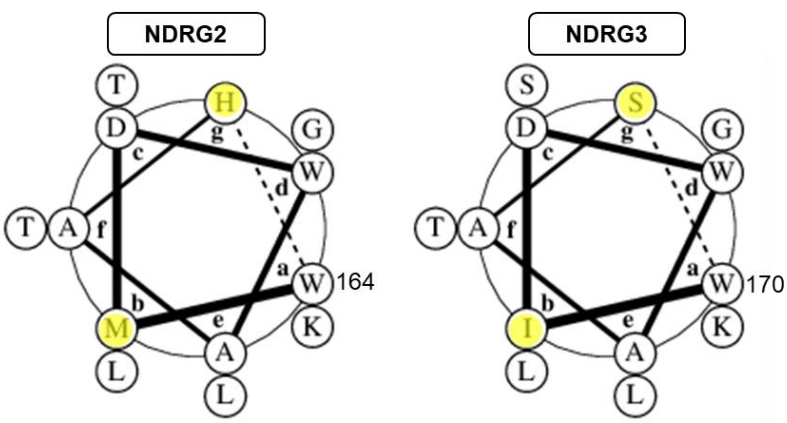

Figure 41. Helix wheel model of helix α6 region based on its sequence.

The N-terminal region of helix α6 region of NDRG3 is start from Trp170. Mutated sites (I171 and S176) are highlighted in yellow.

In the case of the NDRG3 C30S/I171M/S176H, I could not obtain crystals for structure determination, so I implemented circular dichroism (CD) experiments to compare secondary structure elements of NDRG3 WT, NDRG3 mutants, and NDRG2 (Figure 42). While the ellipticities of CD spectrum from NDRG3 WT at 222 nm and 208 nm (θ222 and θ208) were lower than those from NDRG2, the θ222/θ208 ratios of NDRG3 WT and NDRG2 were 1.10 and 1.93, respectively. Considering that θ222/θ208 ratios represent extents of inter-helix interactions (Lau, et al., 1984, J Biol Chem, 59; Manning and Woody, 1991, Biopolymers, 60; Choy, et al., 2003, J Mol Biol, 61), α-helices of NDRG2 are more associated together than those of NDRG3. The CD spectrum of NDRG3 C30S/I171M/S176H was very similar to that of NDRG3 WT but not to that of NDRG2. Therefore, NDRG3 C30S/I171M/S176H seems to be structurally similar to NDRG3 WT. When I further analyzed sequences before and after the helix α6 region of NDRG3 compared with those of NDRG2, the amino acid sequences following the helix α6 region are TNVV and SSIP in NDRG3 and NDRG2, respectively (Figure 23). Furthermore, the structures of following the helix α6 region do not superimpose well (Figure 32). Among residues following the helix α6 region, Val186 in NDRG3 and Pro180 in NDRG2 exhibited the most different biophysical properties. To see whether residues directly following the helix α6 region affect local folding, we mutated Val186 in NDRG3 to Pro and analyzed secondary structure elements using CD. However, CD spectra of NDRG3 V186P and I171M/S176H/V186P mutants did not exhibit changes compared with that of the NDRG3 WT (Figure 42). Taken all together, the unfolded helix α6 region of NDRG3 is structurally unique in comparison to NDRG2 or any other α/β-

hydrolase fold proteins, and the structure is not only determined by nearby sequences but seems to be influenced by its surrounding environment.

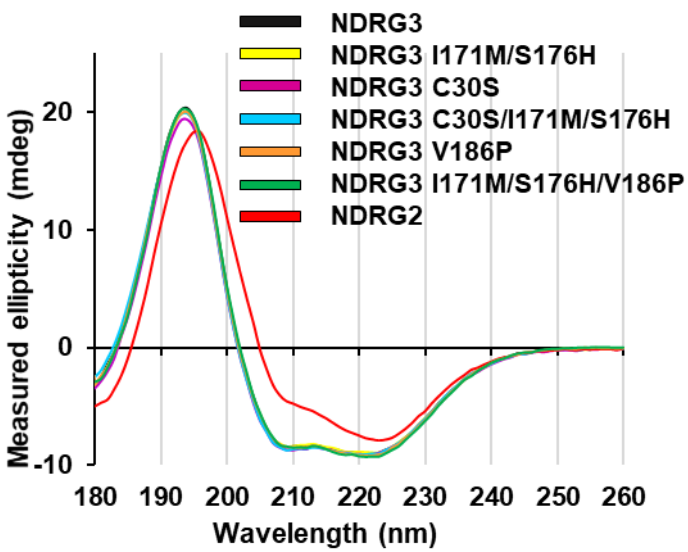

Figure 42. CD spectra of NDRG3 WT, I171M/S176H, C30S, C30S/I171M/S176H, V186P, I171M/S176H/V186P, and NDRG2.

– Chapter 2. Biophysical studies on lactate–related NDRG3 responses –

3.6. *In vitro* binding assays on NDRG3 against lactate.

Since NDRG3 was reported to physically interact with $_{L}$–lactate using [^{14}C]–labeled $_{L}$–lactate (Figure 43), I implemented affinity studies between NDRG3 and $_{L}$–lactate to measure K_D value using isothermal titration calorimetry (ITC) (Figure 44), microscale thermophoresis (MST), and surface plasmon resonance (SPR) (Figure 45), but the results did not allow to determine a clear interaction *in vitro*. NDRG3 protein is overexpressed over 8 mM lactate condition (Lee, et al., 2015, Cell, 28), affinity between NDRG and lactate is weak. Therefore, I used high concentration of lactate during ITC, MST, and SPR experiment. In the case of the ITC experiment, heat transfers were in each injections of lactate. In the cases of MST and SPR, responses were changed at high concentration of lactate, however, these changes seem to be caused by low pH condition. pH value was notably decreased at 25 mM lactate in 50 mM HEPES–NaOH buffer (pH 5.6) compared with that of 12.5 mM lactate in 50 mM HEPES–NaOH buffer (7.1).

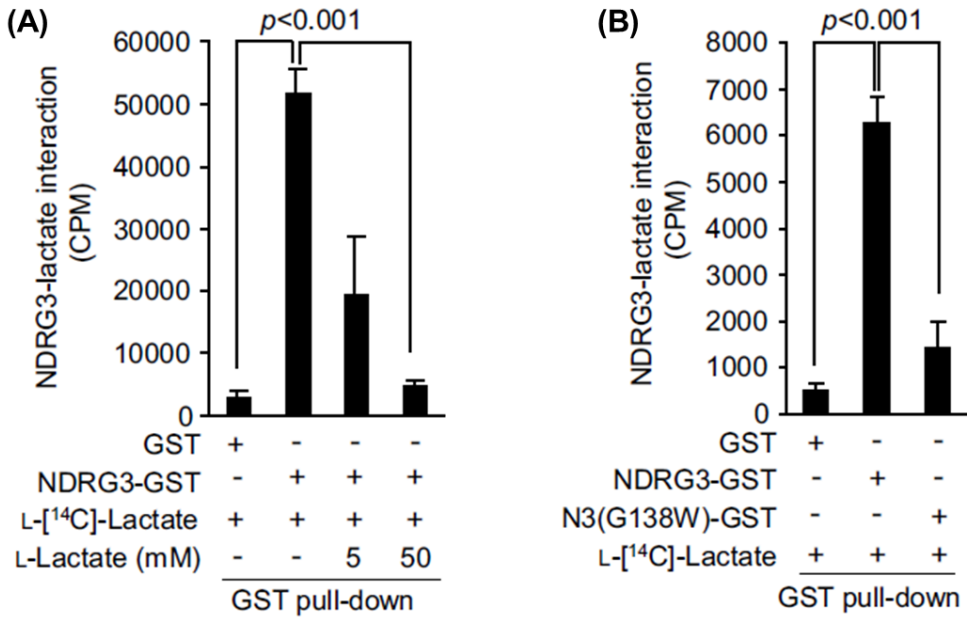

Figure 43. Molecular interaction between L-lactate and NDRG3 *in vitro* (Figures are adopted from Lee, et al., 2015, Cell, 28).

(A) Interaction between L-lactate and NDRG3. Results are mean ± SD of three experiments. The *p* value was assessed by Student's. (B) Interaction between L-lactate and NDRG3 G138W mutant. Results are mean ± SD of three experiments. The *p* value was assessed by Student's.

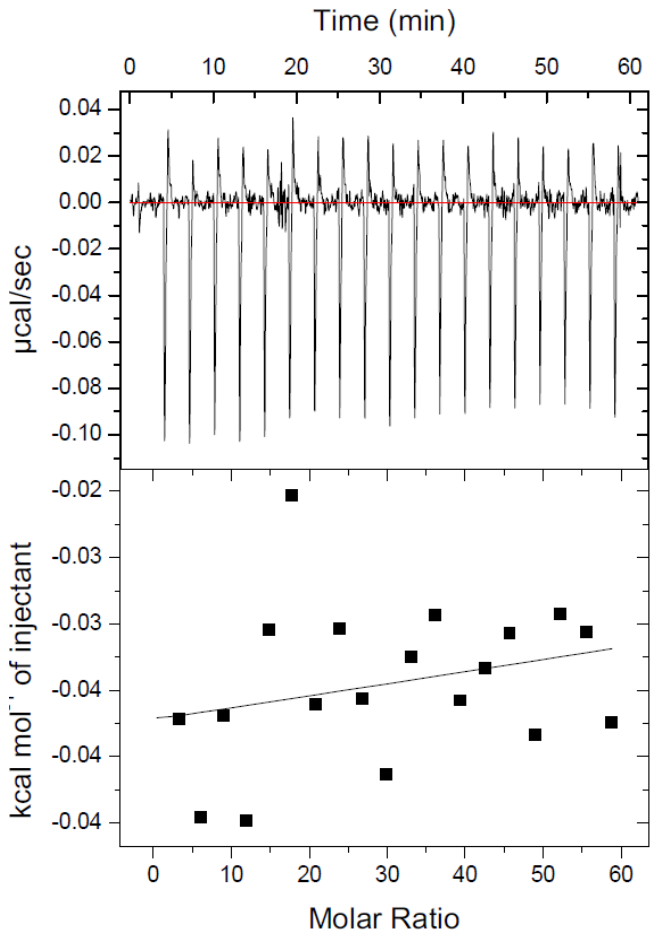

Figure 44. Interaction between NDRG3 and lactate measured by ITC.

ITC could not determine molecular interactions between NDRG3 and lactate. I carried out this ITC experiments with 30 μM of NDRG3 and 10 mM of lactate.

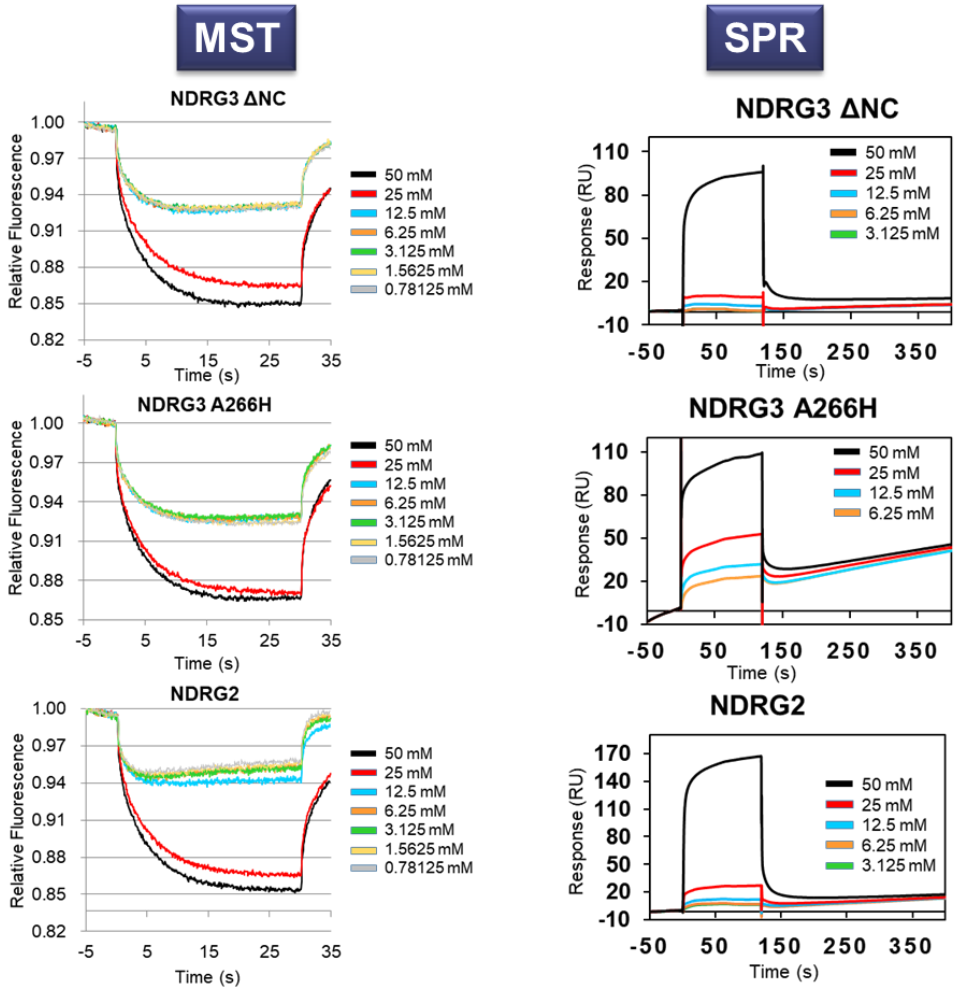

Figure 45. Interaction between NDRG3 and lactate measured by MST and SPR.

MST and SPR could not determine molecular interactions between NDRG3 and lactate.

3.7. Crystal structures of NDRG3 supplemented with different L-lactate concentrations

To determine lactate binding site of NDRG3, I performed co-crystallization of NDRG3 with lactate. Crystal structures of NDRG3 supplemented with 5 mM and 20 mM of L-lactate were determined at 2.70 Å and 2.85 Å resolution, respectively (Figure 46, Figure 47, and Figure 48), but I was unable to model the location of lactate nor observe any structural changes in L-lactate-added structures compared with NDRG3 (Figure 48 and Figure 49). However, the normalized B-factor of the crystal structure at 20 mM of L-lactate markedly decreased in the helix α12 region including Pro294, compared with that of apo and the crystal structures at 5 mM L-lactate (Figure 50).

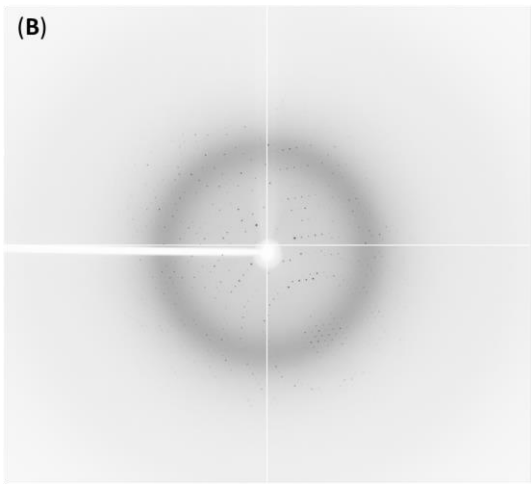

(C)

Shell Lower limit	Upper Angstrom	Average I	Average error	Norm. stat.	Linear Chi**2	Square R-fac	R-fac	Rmeas	Rpim	CC1/2	CC*
50.00	7.32	1904.4	45.9	23.7	0.953	0.043	0.053	0.046	0.015	0.997	0.999
7.32	5.81	716.3	15.7	9.9	0.846	0.052	0.058	0.054	0.016	0.998	0.999
5.81	5.08	858.5	19.1	12.3	0.849	0.052	0.058	0.055	0.016	0.998	0.999
5.08	4.62	1132.6	24.0	15.1	0.847	0.051	0.057	0.053	0.015	0.998	0.999
4.62	4.29	1088.5	24.0	15.5	1.015	0.056	0.062	0.059	0.017	0.998	0.999
4.29	4.03	781.3	19.2	13.6	0.933	0.063	0.063	0.066	0.019	0.998	1.000
4.03	3.83	650.4	17.1	12.7	0.951	0.069	0.069	0.072	0.021	0.998	0.999
3.83	3.66	601.0	16.4	12.6	1.063	0.075	0.079	0.078	0.022	0.996	0.999
3.66	3.52	467.4	14.4	11.6	0.977	0.084	0.082	0.087	0.025	0.997	0.999
3.52	3.40	391.3	13.5	11.3	0.990	0.097	0.093	0.101	0.029	0.997	0.999
3.40	3.30	284.3	11.9	10.5	0.969	0.118	0.111	0.123	0.035	0.995	0.999
3.30	3.20	240.4	11.4	10.3	0.936	0.134	0.125	0.140	0.040	0.994	0.999
3.20	3.12	190.8	10.9	10.1	0.943	0.162	0.153	0.169	0.048	0.992	0.998
3.12	3.04	145.6	10.4	9.8	0.937	0.207	0.188	0.216	0.062	0.990	0.997
3.04	2.97	123.3	10.3	9.9	0.956	0.246	0.231	0.257	0.073	0.982	0.995
2.97	2.91	98.9	10.1	9.8	0.960	0.307	0.289	0.320	0.091	0.978	0.994
2.91	2.85	84.7	10.1	9.8	0.984	0.372	0.347	0.388	0.111	0.965	0.991
2.85	2.80	69.7	10.1	9.9	0.974	0.450	0.419	0.470	0.134	0.957	0.989
2.80	2.75	68.6	10.3	10.1	0.976	0.466	0.443	0.486	0.138	0.953	0.988
2.75	2.70	57.5	10.5	10.4	0.987	0.575	0.514	0.600	0.171	0.947	0.986
All reflections		504.5	15.9	12.0	0.953	0.085	0.069	0.088	0.026		

Figure 46. Crystal of NDRG3 at 5 mM lactate.

(A) The best diffracting crystal of NDRG3 at 5 mM lactate was grown under 200 mM sodium citrate and 20% PEG3350. (B) A diffraction image of the best diffracting crystal of NDRG3 with 5 mM lactate. (C) Scaling statistics of the best diffracting crystal of NDRG3 with 5 mM lactate.

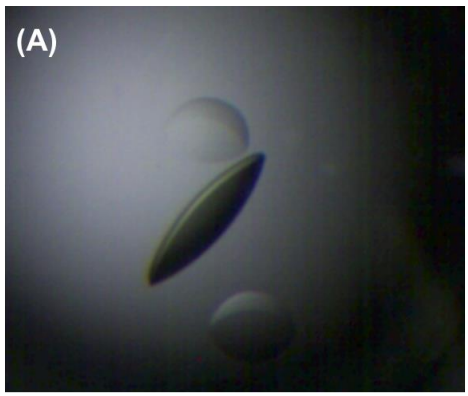

(B)

Shell limit	Lower Angstrom	Upper	Average I	Average error	Norm. stat.	Linear Chi**2	Square R-fac	R-fac	Rmeas	Rpim	CC1/2	CC*
50.00	7.73	358.9	14.8	4.9	1.350	0.064	0.091	0.074	0.037	0.982	0.995	
7.73	6.14	69.5	3.8	2.3	0.597	0.048	0.060	0.057	0.030	0.991	0.998	
6.14	5.36	63.1	3.7	2.5	0.659	0.060	0.065	0.069	0.035	0.992	0.998	
5.36	4.87	67.3	3.9	2.7	0.733	0.067	0.071	0.077	0.038	0.990	0.997	
4.87	4.52	77.7	4.5	3.0	0.781	0.069	0.075	0.080	0.040	0.989	0.997	
4.52	4.26	65.6	4.1	3.0	0.900	0.082	0.085	0.094	0.046	0.987	0.997	
4.26	4.04	45.3	3.6	2.8	0.853	0.093	0.089	0.109	0.056	0.987	0.997	
4.04	3.87	39.0	3.4	2.7	0.880	0.104	0.098	0.122	0.064	0.983	0.996	
3.87	3.72	33.9	3.3	2.8	0.903	0.112	0.111	0.133	0.071	0.974	0.993	
3.72	3.59	29.8	3.0	2.6	0.996	0.136	0.126	0.159	0.081	0.975	0.994	
3.59	3.48	23.6	2.7	2.4	0.957	0.158	0.146	0.184	0.093	0.971	0.993	
3.48	3.38	19.5	2.6	2.3	0.926	0.181	0.164	0.210	0.105	0.969	0.992	
3.38	3.29	15.3	2.4	2.3	0.976	0.234	0.207	0.271	0.135	0.949	0.987	
3.29	3.21	12.3	2.3	2.2	1.009	0.286	0.266	0.331	0.165	0.924	0.980	
3.21	3.14	10.1	2.2	2.1	0.957	0.317	0.310	0.367	0.183	0.886	0.969	
3.14	3.07	8.5	2.2	2.1	0.995	0.376	0.366	0.436	0.219	0.841	0.956	
3.07	3.01	7.2	2.2	2.1	1.031	0.436	0.408	0.507	0.256	0.820	0.949	
3.01	2.95	5.5	2.2	2.1	0.996	0.514	0.477	0.602	0.308	0.751	0.926	
2.95	2.90	4.8	2.2	2.2	0.972	0.552	0.529	0.650	0.338	0.695	0.906	
2.90	2.85	4.0	2.2	2.2	1.002	0.651	0.603	0.767	0.402	0.603	0.867	
All reflections		49.0	3.6	2.6	0.924	0.094	0.091	0.110	0.055	0.989	0.997	

Figure 47. Crystal of NDRG3 at 20 mM lactate.

(A) The best diffracting crystal of NDRG3 at 20 mM lactate was grown under 210 mM sodium citrate and 20% PEG3350. (B) Scaling statistics of the best diffracting crystal of NDRG3 with 20 mM lactate.

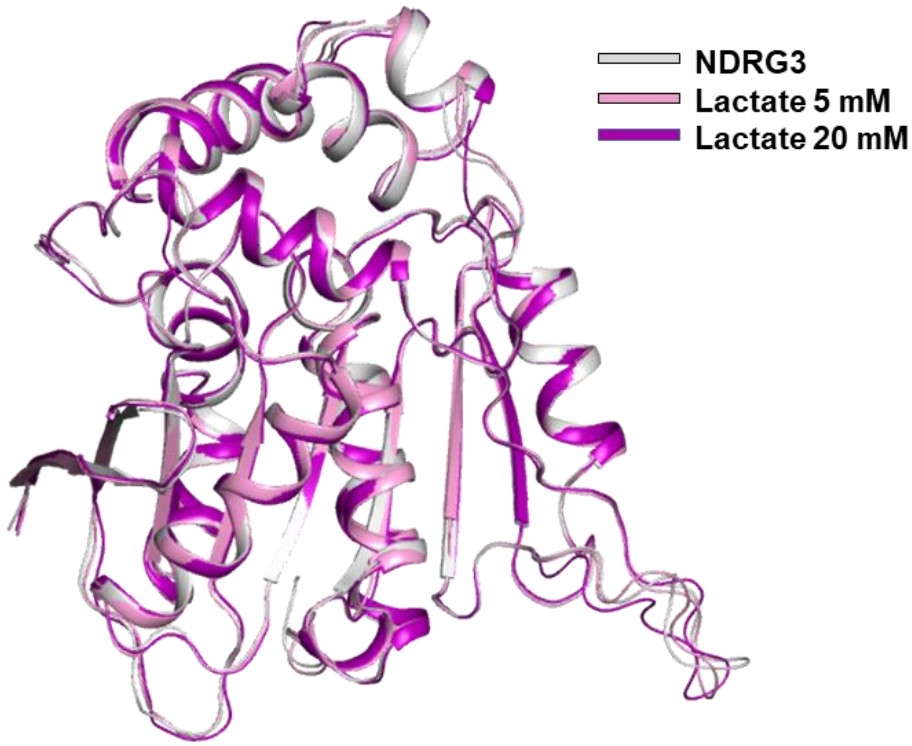

Figure 48. Structural comparison between NDRG3 and NDRG3 supplemented with lactate.

Overall view of superimposition of NDRG3 apo, co-crystallized with 5 mM lactate, and 20 mM lactate. The structures are shown in cartoon model.

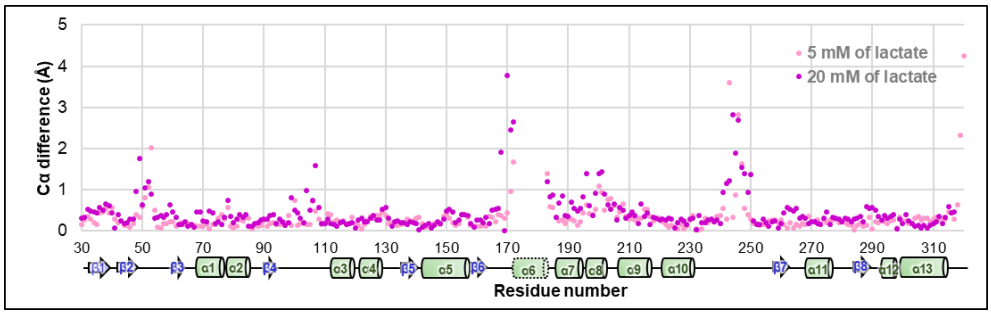

Figure 49. Structural comparison of C_α r.m.s.d. values at 5 mM and 20 mM lactate supplemented structures against NDRG3 structure.

Pink and violet dots represent the r.m.s.d. values at 5 mM and 20 mM lactate co-crystallized structures, respectively. The secondary structure of NDRG3 is shown at the bottom of the r.m.s.d. comparison.

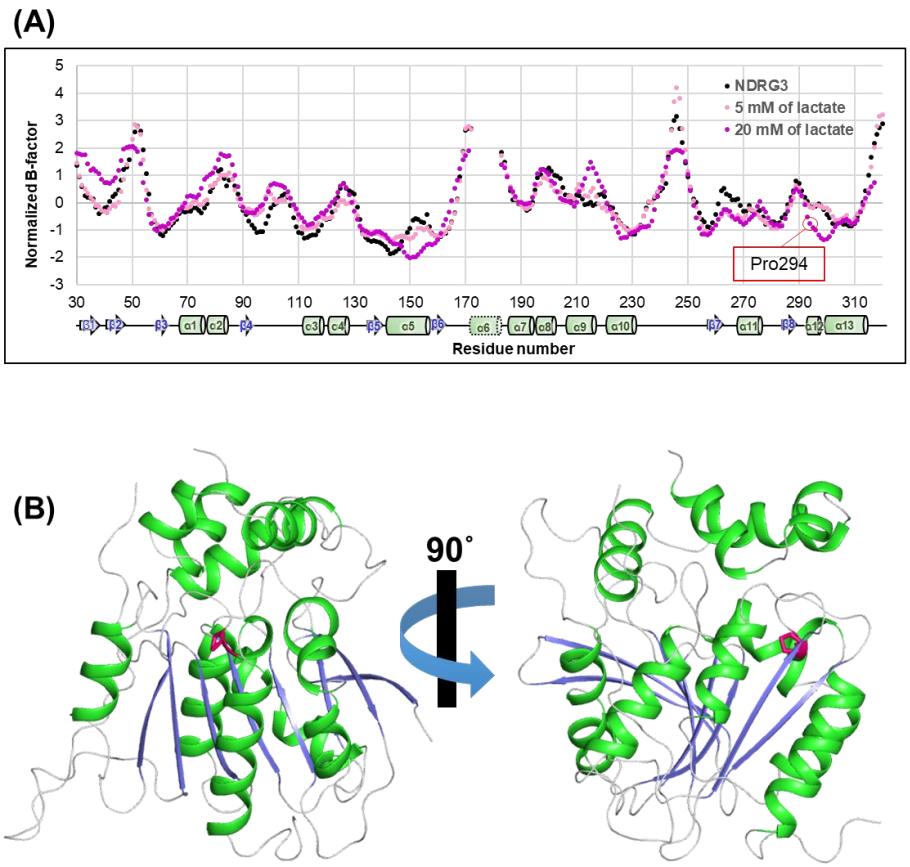

Figure 50. Comparison of the normalized B-factors at 5 mM and 20 mM lactate co-crystallized structures.

(A) The normalized B-factors for the NDRG3 apo, 5 mM, and 20 mM lactate co-crystallized structures are represented as black, pink, and violet dots, respectively. A red circle indicates the location of Pro294 of NDRG3. The secondary structure of NDRG3 is shown at the bottom of the normalized B-factor comparison. (B) Location of Pro294 of NDRG3. Pro294 is represented as magenta stick model.

3.8. Computational docking simulation study on NDRG3 against L-lactate.

To gain a clue of binding mode of NDRG3 against L-lactate, I implemented docking study using individual conformations of NDRG3 generated by molecular dynamics simulation using *NAMD* program (Phillips, et al., 2005, J Comput Chem, 48) (Figure 51). Since the crystal structure of NDRG3 C30S contains structure of the helix $\alpha 6$ region, I used the NDRG3 C30S structure for molecular dynamic simulation. Four regions of NDRG3 were predicted to be highly dynamic. Among 1000 conformations generated from molecular dynamic for 100 picoseconds, 21 conformations of were used for template of docking receptor. To predict affinity energy between NDRG3 and lactate, *PatchDock* (Schneidman-Duhovny, et al., 2005, Nucleic Acids Res, 50) followed by *FireDock* (Mashiach, et al., 2008, Nucleic Acids Res, 51) were performed (Figure 52). A loop between $\alpha 10$-$\beta 7$ was predicted to interact with lactate in three conformations generated from molecular dynamics and predicted affinity energies between the three conformations against lactate was lower than the other conformations. Interestingly, the loop between $\alpha 10$-$\beta 7$ of NDRG3 is unique motif among NDRG family proteins (Figure 23). In conclusion, this docking study hints molecular interaction of NDRG3 against lactate and the unique motif of NDRG3 seems to be an interaction site with lactate.

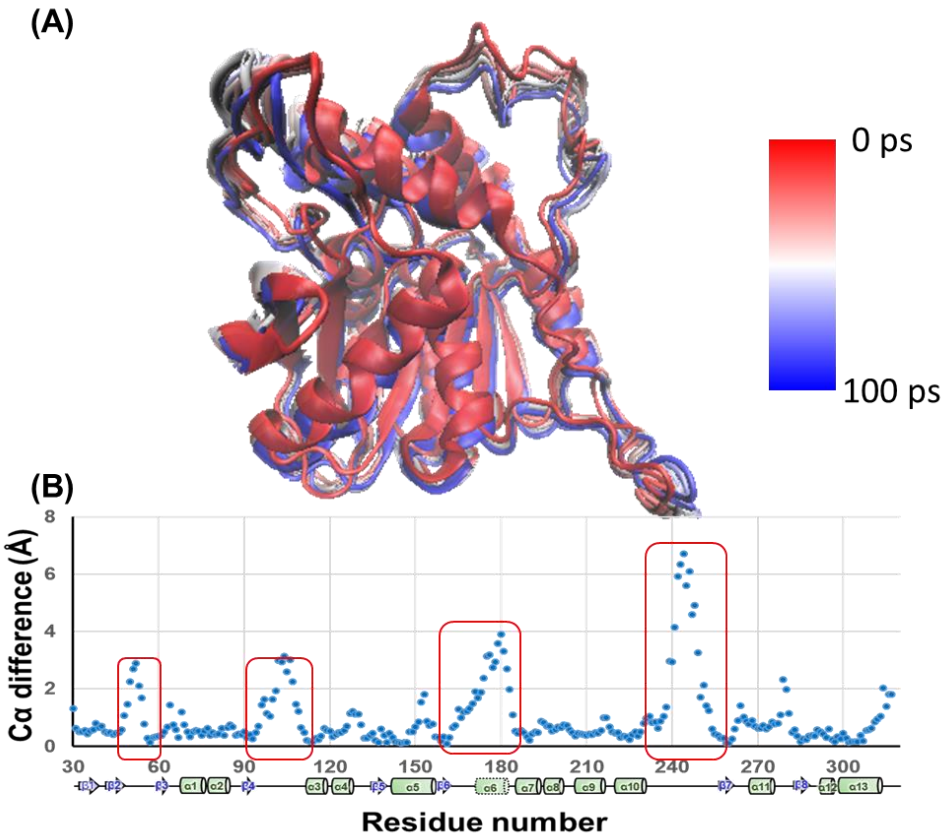

Figure 51. Molecular dynamic simulation on NDRG3 C30S structure for 100 picoseconds.

(A) Superimposition of 11 structures which were calculated by *NAMD* program. The red, white and blue models are NDRG3 structure at 0, 50, and 100 ps, respectively. (B) Structural comparison of C_α r.m.s.d. differences for 11 calculated structures. The highly dynamic regions were marked by red boxes.

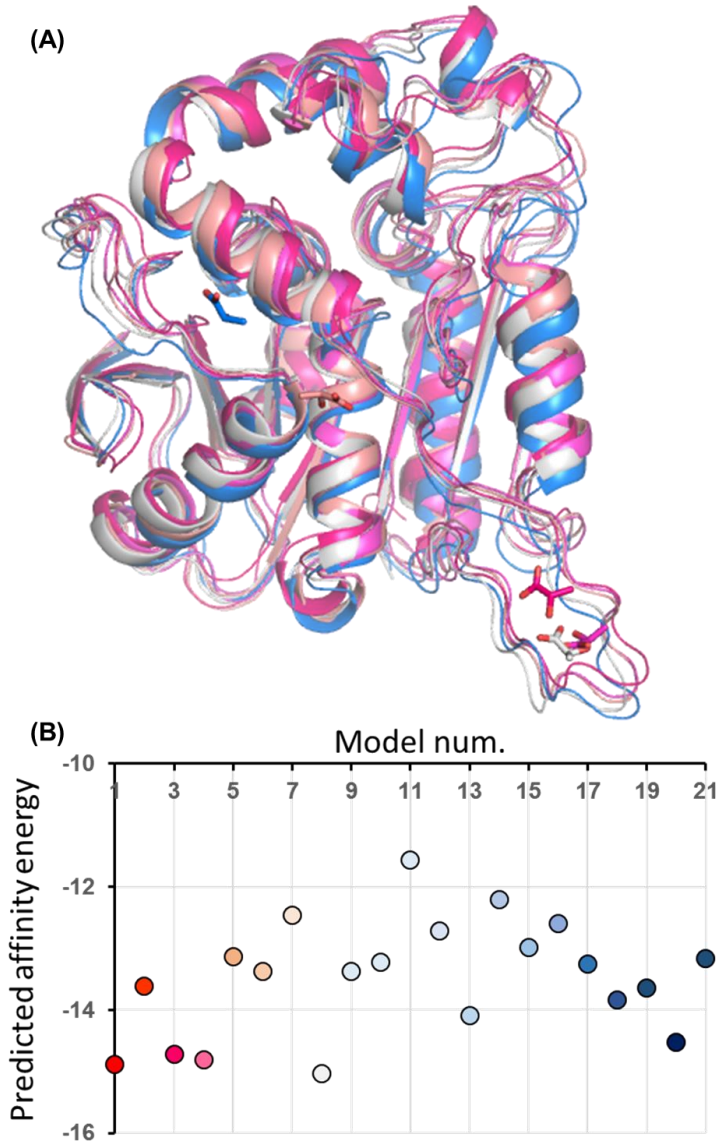

Figure 52. Docking results of individual conformations of NDRG3 against lactate.

(A) Superimposition of docking results of 21 NDRG3 structures against lactate. Colors of model are denoted as Figure 52B (B) Predicted affinity energies of the 21 NDRG3 structures against lactate.

4. Discussion

Since the first characterization of NDRG1 in 1999, the NDRG family has been reported to play promiscuous roles in tumorigenesis or tumor suppression. Then a pro-tumorigenic activity was reported for a member of the NDRG family, NDRG3, when it was known to be associated with prostate cancer (Wang, et al., 2009, Int J Cancer, 27). Later, in the last five years of studies have elucidated additional roles of NDRG3 in various hypoxia responses, including cell proliferation, double-strand break repair, metastasis, and HIF regulation. In this study, I determined the crystal structure of a truncated human NDRG3 fragment comprising residues from 29 to 320, on the basis of its solubility and crystallizability. Although *HKL2000* program (Otwinowski and Minor, 1997, Methods Enzymol, 39) predicted the structure of the crystals in hexagonal symmetry, I processed and scaled the data using *C*-centered monoclinic symmetry to describe the disulfide bonds between each Cys30 and dimer (Figure 21).

Although NDRG3 mainly exists as a monomer, I observed a stabilized dimer fraction during purification. SEC-MALS experiment under reducing conditions indicates that the disulfide bond does not seem to contribute to its dimerization in solution. To characterize the dimeric association of NDRG3, it was worth noting that the dimeric interface between chain B/F and chain A/D faced different directions in the crystal structure. As shown in Figure 27, the dimeric interface of chain B/F is constituted with vis-à-vis each canonical α/β-hydrolase fold domain by covering helix α13 using the α10-β7 loop of NDRG3, comprising 7.5% of total surface area. The dimeric interface area between chain A/D is slightly larger than

that of chain B/F (7.7% of total surface area) by interacting between each $\alpha 10$–$\beta 7$ loop and each helix $\alpha 10$, respectively. However, PISA predicted that the chain B/F dimer is stable in solution, whereas the chain A/D dimer was predicted to result from crystal packing only. Although the number of hydrogen bonds was equal between both dimers, the length of the hydrogen bonds in the chain B/F dimer was shorter than that of the chain A/D dimer (Figure 37). In addition, the predicted hydrophobic effect of the dimeric interface between chain B and chain F was −11.5 kcal/mol, which comprises 2.2% of total solvation energy, whereas that between chain A and chain D was −4.8 kcal/mol (Figure 26 and 27). NDRG3 S255A/N281A mutant study further proved the dimeric interface of NDRG3 *in vitro* (Figure 28, 29). Considering that Ser255 and Asn281 of NDRG3 are unique sequences among NDRG family (Figure 23) and NDRG2 exists as monomer (Hwang, et al., 2011, J Biol Chem, 40), dimerization of NDRG3 would be a distinctive feature in comparison with other NDRG family proteins. Further studies should be conducted to elucidate physiological relevance of the NDRG3 dimer.

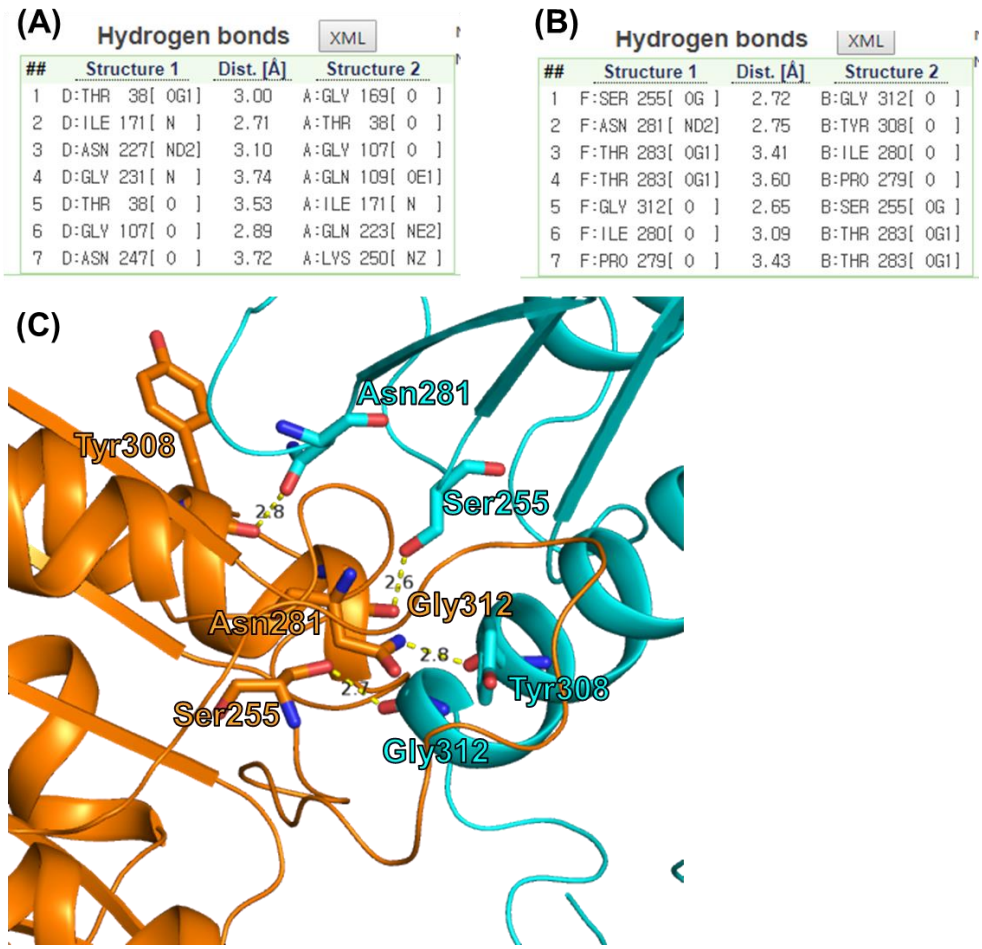

Figure 53. Hydrogen bond interactions in A/D dimer and B/F dimer calculated by PISA.

(A) Hydrogen bond interactions in A/D dimer. (B) Hydrogen bond interactions in B/F dimer. (C) The key hydrogen bond interactions in B/F dimer. Distances of hydrogen bond are measured using *Pymol*. Cyan colored model and labels indicate chain B of NDRG3, and orange colored model and labels indicate chain F of NDRG3 in ASU.

A previous report on the crystal structure of NDRG2 revealed the structural features of helix α6 compared with α/β-hydrolase family proteins and showed that helix α6 plays a key role in regulating TCF/β-catenin signaling (Hwang, et al., 2011, J Biol Chem, 40) (Figure 54). Surprisingly, while NDRG2 and α/β-hydrolase family proteins possess helix α6, the helix α6 region in the crystal structure of NDRG3 was disordered, even though the sequences of the helix α6 region in NDRG2 and NDRG3 are similar. Moreover, the crystal structure of NDRG3 C30S, which counteracts the effects of disulfide bonding, and the CD results of NDRG3 and NDRG3 C30S mutant provided evidence that the helix α6 region in NDRG3 is a flexible loop. Since helix α6 in NDRG2 plays a pivotal role in tumor suppressor activity, the unfolded helix α6 region in NDRG3 seems to exert a different function from helix α6 of NDRG2. Further studies would be needed to demonstrate molecular functions of the unfolded helix α6 region of NDRG3.

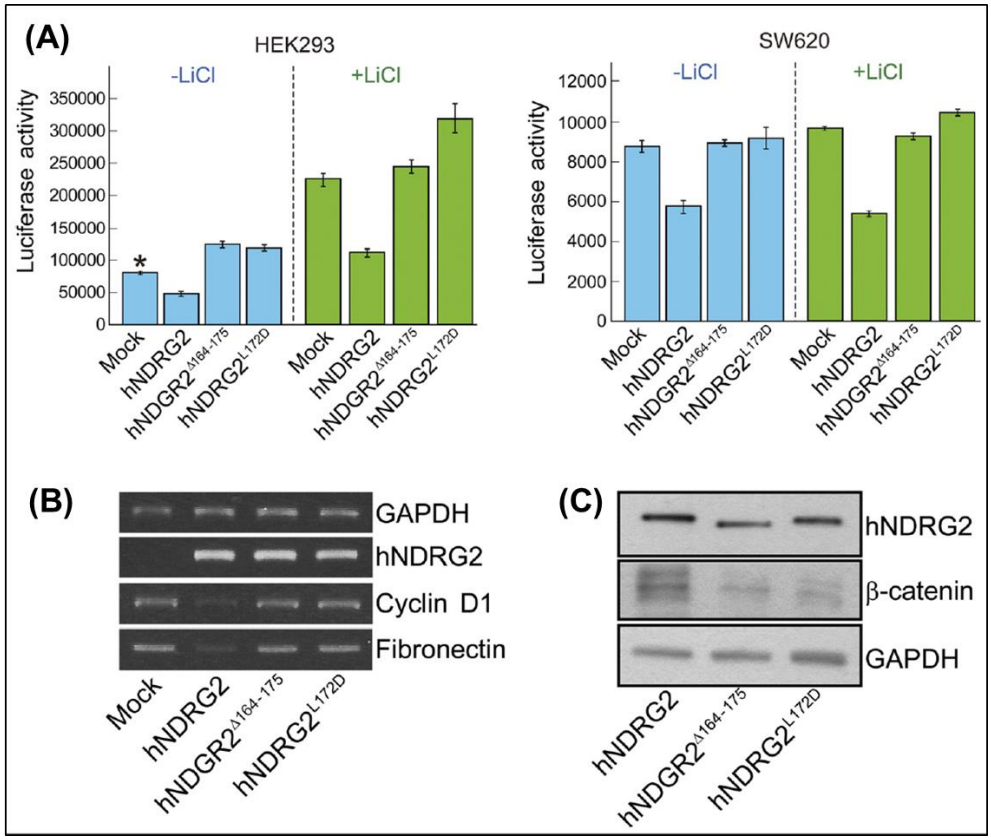

Figure 54. Role of the helix α6 of NDRG2 on TCF/β-catenin signaling (Hwang, et al., 2011, J Biol Chem, 40).

(A) Luciferase reporter assay of NDRG2, NDRG2 α6 deletion, and L172D mutant. Mean S.D. values from three independent experiments performed in duplicate are shown (*, $p < 0.05$). (B) Target genes of TCF/β-catenin, cyclin D1 and fibronectin were assessed by RT-PCR. (C) hNDRG2 was immunoprecipitated with an anti-NDRG2 antibody, and the precipitant was analyzed by SDS-PAGE and Western blot analysis using anti-β-catenin antibody.

NDRG3 has been known to be degraded by PHD2/VHL mediated ubiquitination under normoxia condition, and Pro294 hydroxylation of NDRG3 by PHD2 is a critical step of NDRG3 ubiquitination. To get a clue of ubiquitination of NDRG3, I analyzed ubiquitination sites on NDRG3 using data from the *PhosphoSitePlus* web-server (https://www.phosphosite.org) (Hornbeck, et al., 2015, Nucleic Acids Res, 53). The truncated NDRG3 structure contains two ubiquitination sites, K51 and K286, and K286 site was characterized by mass spectrometry in human cells (Udeshi, et al., 2013, Mol Cell Proteomics, 62), while K51 is a predicted ubiquitination site in human NDRG3. K286 is located in β8 and the region was not well structurally superposed (Figures 24 and 54). In the case of HIF-1α, a representative protein ubiquitinated by PHD2, Pro402, and Pro564 of HIF-1α is hydroxylated by PHD isoforms, and ubiquitination sites of HIF-1α are close to the Pro residues (Appelhoff, et al., 2004, J Biol Chem, 63). Surprisingly, Pro294 of NDRG3 is hydroxylated by PHD2 (Lee, et al., 2015, Cell, 28). Furthermore, K300 and K306 of NDRG1 are known as ubiquitination sites and the Lys residues are amino acidic conserved in NDRG3. Taken together, I suggest that equipositional K301 and K307 of NDRG3 would be novel ubiquitination sites.

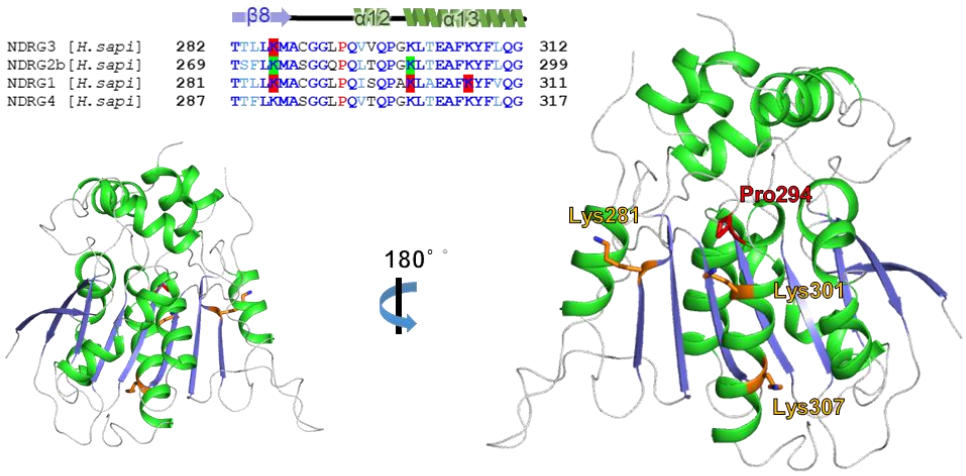

Figure 55. Ubiquitination sites on NDRG3, which are analyzed or predicted using the data from the *PhosphoSitePlus* web-server (https://www.phosphosite.org).

The sequence near Pro294 of NDRg3 is shown above the crystal structure of NDRG3. The red-shaded boxes indicate ubiquitination sites analyzed in human cells and the green-shaded boxes represent predicted ubiquitination sites. Blue and cyan-colored residues represent the identical and conserved residues among the NDRG isoforms, respectively. Pro294 and ubiquitination sites among NDRG family proteins were represented as red and orange stick models, respectively.

Sequence comparisons and structural studies revealed that proteins of the NDRG family contain an α/β-hydrolase fold domain. Although NDRG3 has a high structural similarity to the α/β-hydrolase family, the substitution of the residues of the enzymatic catalytic triad and narrow folded cavity due to the presence of helix $\alpha 7$ and helix $\alpha 10$ indicate that NDRG3 is a nonenzymatic α/β-hydrolase fold protein. Especially, NDRG3 was reported to interact with lactate and exert oncogenic function under hypoxia condition, I tried to determine molecular interactions between NDRG3 and lactate using *in vitro* binding assays and co-crystallization. Crystal structures of NDRG3 with additions of 5 mM and 20 mM of $_{L}$-lactate were determined at 2.70 Å and 2.85 Å resolution, respectively (Figure 48). However, I was unable to model the location of lactate nor observed any structural changes in $_{L}$-lactate-added structures compared with NDRG3. Furthermore, affinity studies between NDRG3 and $_{L}$-lactate using ITC, MST, and SPR were performed, but the results were unclear to determine affinity between NDRG3 and lactate. However, the normalized B-factor of the crystal structure at 20 mM of $_{L}$-lactate notably decreased in the helix $\alpha 12$ region including Pro294, compared with that of apo and the crystal structures at 5 mM $_{L}$-lactate (Figure 50). Because Pro294 is a critical target site of PHD2-mediated NDRG3 ubiquitination (Lee, et al., 2015, Cell, 28) and it is located in inner surface of pseudo-active site, a large conformational change is needed to interact with PHD2. B-factor comparisons of the crystal structures of NDRG3 supplemented with different concentration of lactate suggest that a high concentration of lactate stabilize the helix $\alpha 12$ region and interrupt its conformational change, compared with NDRG3 structure at low concentration of lactate. Moreover,

considering that helix α9 in NDRG3 was predicted to interact with PHD2 in a docking study (Lee, et al., 2015, Cell, 28), the structural differences of helix α9 between NDRG3 and NDRG2 (Figure 36) hint the distinctive feature of NDRG3 against PHD2. Although I was unable to elucidate the interaction between NDRG3 and lactate, these crystal structures imply molecular interactions between NDRG3 and PHD2. Further studies should be implemented in order to clarify the molecular mechanisms of NDRG3 in the modulation of the lactate-induced hypoxia responses.

5. Conclusion

I reported the crystal structure of human NDRG3 and demonstrated the dimeric conformation of NDRG3 from crystal packing in an ASU. Compared with NDRG2, the helix $\alpha 6$ region of NDRG3 is a flexible loop. Considering that helix $\alpha 6$ of NDRG2 regulates TCF/β−catenin signaling, the unfolded helix $\alpha 6$ of NDRG3 would play a distinctive role upon interacting with physiologically relevant binding partners. This structural studies on NDRG3 will shed light on the characterization of NDRG family proteins, providing a fundamental source for understanding the molecular mechanism of NDRG3 in hypoxia responses.

References

1. Ollis DL, Cheah E, Cygler M, Dijkstra B, Frolow F, Franken SM, Harel M, Remington SJ, Silman I, Schrag J, et al. The alpha/beta hydrolase fold. Protein Eng 1992;5(3):197-211.
2. Botti SA, Felder CE, Sussman JL, Silman I. Electrotactins: a class of adhesion proteins with conserved electrostatic and structural motifs. Protein Eng 1998;11(6):415-420.
3. De Jaco A, Comoletti D, Dubi N, Camp S, Taylor P. Processing of cholinesterase-like alpha/beta-hydrolase fold proteins: alterations associated with congenital disorders. Protein Pept Lett 2012;19(2):173-179.
4. Marchot P, Chatonnet A. Enzymatic activity and protein interactions in alpha/beta hydrolase fold proteins: moonlighting versus promiscuity. Protein Pept Lett 2012;19(2):132-143.
5. Shimono A, Okuda T, Kondoh H. N-myc-dependent repression of ndr1, a gene identified by direct subtraction of whole mouse embryo cDNAs between wild type and N-myc mutant. Mech Dev 1999;83(1-2):39-52.
6. Shaw E, McCue LA, Lawrence CE, Dordick JS. Identification of a novel class in the alpha/beta hydrolase fold superfamily: the N-myc differentiation-related proteins. Proteins 2002;47(2):163-168.
7. O'Connell BC, Cheung AF, Simkevich CP, Tam W, Ren X, Mateyak MK, Sedivy JM. A large scale genetic analysis of c-Myc-regulated gene expression patterns. J Biol Chem 2003;278(14):12563-12573.
8. Vervoorts J, Luscher-Firzlaff J, Luscher B. The ins and outs of MYC regulation by posttranslational mechanisms. J Biol Chem 2006;281(46):34725-34729.
9. Qu X, Zhai Y, Wei H, Zhang C, Xing G, Yu Y, He F. Characterization and expression of three novel differentiation-related genes belong to the human NDRG gene family. Mol Cell Biochem 2002;229(1-2):35-44.
10. El-Gebali S, Mistry J, Bateman A, Eddy SR, Luciani A, Potter SC, Qureshi M, Richardson LJ, Salazar GA, Smart A, Sonnhammer ELL, Hirsh L, Paladin L, Piovesan D, Tosatto SCE, Finn RD. The Pfam protein families database in 2019. Nucleic Acids Res 2019;47(D1):D427-D432.
11. Melotte V, Qu X, Ongenaert M, van Criekinge W, de Bruine AP, Baldwin HS, van Engeland M. The N-myc downstream regulated gene (NDRG) family: diverse functions, multiple applications. FASEB J 2010;24(11):4153-4166.
12. Ring BZ, Seitz RS, Beck R, Shasteen WJ, Tarr SM, Cheang MC, Yoder BJ, Budd GT, Nielsen TO, Hicks DG, Estopinal NC, Ross DT. Novel prognostic immunohistochemical biomarker panel for

estrogen receptor-positive breast cancer. J Clin Oncol 2006;24(19):3039-3047.
13. Bandyopadhyay S, Pai SK, Hirota S, Hosobe S, Takano Y, Saito K, Piquemal D, Commes T, Watabe M, Gross SC, Wang Y, Ran S, Watabe K. Role of the putative tumor metastasis suppressor gene Drg-1 in breast cancer progression. Oncogene 2004;23(33):5675-5681.
14. Guan RJ, Ford HL, Fu Y, Li Y, Shaw LM, Pardee AB. Drg-1 as a differentiation-related, putative metastatic suppressor gene in human colon cancer. Cancer Res 2000;60(3):749-755.
15. van Belzen N, Dinjens WN, Diesveld MP, Groen NA, van der Made AC, Nozawa Y, Vlietstra R, Trapman J, Bosman FT. A novel gene which is up-regulated during colon epithelial cell differentiation and down-regulated in colorectal neoplasms. Lab Invest 1997;77(1):85-92.
16. Sun B, Chu D, Li W, Chu X, Li Y, Wei D, Li H. Decreased expression of NDRG1 in glioma is related to tumor progression and survival of patients. J Neurooncol 2009;94(2):213-219.
17. Bandyopadhyay S, Pai SK, Gross SC, Hirota S, Hosobe S, Miura K, Saito K, Commes T, Hayashi S, Watabe M, Watabe K. The Drg-1 gene suppresses tumor metastasis in prostate cancer. Cancer Res 2003;63(8):1731-1736.
18. Maruyama Y, Ono M, Kawahara A, Yokoyama T, Basaki Y, Kage M, Aoyagi S, Kinoshita H, Kuwano M. Tumor growth suppression in pancreatic cancer by a putative metastasis suppressor gene Cap43/NDRG1/Drg-1 through modulation of angiogenesis. Cancer Res 2006;66(12):6233-6242.
19. Chua MS, Sun H, Cheung ST, Mason V, Higgins J, Ross DT, Fan ST, So S. Overexpression of NDRG1 is an indicator of poor prognosis in hepatocellular carcinoma. Mod Pathol 2007;20(1):76-83.
20. Nishio S, Ushijima K, Tsuda N, Takemoto S, Kawano K, Yamaguchi T, Nishida N, Kakuma T, Tsuda H, Kasamatsu T, Sasajima Y, Kage M, Kuwano M, Kamura T. Cap43/NDRG1/Drg-1 is a molecular target for angiogenesis and a prognostic indicator in cervical adenocarcinoma. Cancer Lett 2008;264(1):36-43.
21. Lee DC, Kang YK, Kim WH, Jang YJ, Kim DJ, Park IY, Sohn BH, Sohn HA, Lee HG, Lim JS, Kim JW, Song EY, Kim DM, Lee MN, Oh GT, Kim SJ, Park KC, Yoo HS, Choi JY, Yeom YI. Functional and clinical evidence for NDRG2 as a candidate suppressor of liver cancer metastasis. Cancer Res 2008;68(11):4210-4220.
22. Chu D, Zhang Z, Li Y, Wu L, Zhang J, Wang W, Zhang J. Prediction of colorectal cancer relapse and prognosis by tissue mRNA levels of NDRG2. Mol Cancer Ther 2011;10(1):47-56.
23. Yamamura A, Miura K, Karasawa H, Morishita K, Abe K, Mizuguchi Y, Saiki Y, Fukushige S, Kaneko N, Sase T, Nagase H, Sunamura M, Motoi F, Egawa S, Shibata C, Unno M, Sasaki I, Horii A. Suppressed expression of NDRG2 correlates with poor prognosis in pancreatic cancer. Biochem Biophys Res Commun 2013;441(1):102-107.

24. Choi SC, Yoon SR, Park YP, Song EY, Kim JW, Kim WH, Yang Y, Lim JS, Lee HG. Expression of NDRG2 is related to tumor progression and survival of gastric cancer patients through Fas-mediated cell death. Exp Mol Med 2007;39(6):705-714.
25. Deng Y, Yao L, Chau L, Ng SS, Peng Y, Liu X, Au WS, Wang J, Li F, Ji S, Han H, Nie X, Li Q, Kung HF, Leung SY, Lin MC. N-Myc downstream-regulated gene 2 (NDRG2) inhibits glioblastoma cell proliferation. Int J Cancer 2003;106(3):342-347.
26. Liang ZL, Kang K, Yoon S, Huang SM, Lim JS, Kim JM, Lim JS, Lee HJ. NDRG2 is involved in the oncogenic properties of renal cell carcinoma and its loss is a novel independent poor prognostic factor after nephrectomy. Ann Surg Oncol 2012;19(8):2763-2772.
27. Wang W, Li Y, Li Y, Hong A, Wang J, Lin B, Li R. NDRG3 is an androgen regulated and prostate enriched gene that promotes in vitro and in vivo prostate cancer cell growth. Int J Cancer 2009;124(3):521-530.
28. Lee DC, Sohn HA, Park ZY, Oh S, Kang YK, Lee KM, Kang M, Jang YJ, Yang SJ, Hong YK, Noh H, Kim JA, Kim DJ, Bae KH, Kim DM, Chung SJ, Yoo HS, Yu DY, Park KC, Yeom YI. A lactate-induced response to hypoxia. Cell 2015;161(3):595-609.
29. Jing JS, Li H, Wang SC, Ma JM, Yu LQ, Zhou H. NDRG3 overexpression is associated with a poor prognosis in patients with hepatocellular carcinoma. Biosci Rep 2018;38(6).
30. Li T, Sun R, Lu M, Chang J, Meng X, Wu H. NDRG3 facilitates colorectal cancer metastasis through activating Src phosphorylation. Onco Targets Ther 2018;11:2843-2852.
31. Lee GY, Shin SH, Shin HW, Chun YS, Park JW. NDRG3 lowers the metastatic potential in prostate cancer as a feedback controller of hypoxia-inducible factors. Exp Mol Med 2018;50(5):61.
32. Estiar MA, Zare AA, Esmaeili R, Farahmand L, Fazilaty H, Jafari D, Samadi T, Majidzadeh AK. Clinical significance of NDRG3 in patients with breast cancer. Future Oncol 2017;13(11):961-969.
33. Chu D, Zhang Z, Zhou Y, Li Y, Zhu S, Zhang J, Zhao Q, Ji G, Wang W, Zheng J. NDRG4, a novel candidate tumor suppressor, is a predictor of overall survival of colorectal cancer patients. Oncotarget 2015;6(10):7584-7596.
34. Ding W, Zhang J, Yoon JG, Shi D, Foltz G, Lin B. NDRG4 is downregulated in glioblastoma and inhibits cell proliferation. OMICS 2012;16(5):263-267.
35. Lee GY, Chun YS, Shin HW, Park JW. Potential role of the N-MYC downstream-regulated gene family in reprogramming cancer metabolism under hypoxia. Oncotarget 2016;7(35):57442-57451.
36. Pan H, Zhang X, Jiang H, Jiang X, Wang L, Qi Q, Bi Y, Wang J, Shi Q, Li R. Ndrg3 gene regulates DSB repair during meiosis through modulation the ERK signal pathway in the male germ cells. Sci Rep 2017;7:44440.
37. Cui C, Lin H, Shi Y, Pan R. Hypoxic postconditioning attenuates apoptosis via inactivation of adenosine A2a receptor through

NDRG3-Raf-ERK pathway. Biochem Biophys Res Commun 2017;491(2):277-284.
38. Park KC, Lee DC, Yeom YI. NDRG3-mediated lactate signaling in hypoxia. BMB Rep 2015;48(6):301-302.
39. Otwinowski Z, Minor W. Processing of X-ray diffraction data collected in oscillation mode. Methods Enzymol 1997;276:307-326.
40. Hwang J, Kim Y, Kang HB, Jaroszewski L, Deacon AM, Lee H, Choi WC, Kim KJ, Kim CH, Kang BS, Lee JO, Oh TK, Kim JW, Wilson IA, Kim MH. Crystal structure of the human N-Myc downstream-regulated gene 2 protein provides insight into its role as a tumor suppressor. J Biol Chem 2011;286(14):12450-12460.
41. Adams PD, Afonine PV, Bunkoczi G, Chen VB, Davis IW, Echols N, Headd JJ, Hung LW, Kapral GJ, Grosse-Kunstleve RW, McCoy AJ, Moriarty NW, Oeffner R, Read RJ, Richardson DC, Richardson JS, Terwilliger TC, Zwart PH. PHENIX: a comprehensive Python-based system for macromolecular structure solution. Acta Crystallogr D Biol Crystallogr 2010;66(Pt 2):213-221.
42. Vagin AA, Steiner RA, Lebedev AA, Potterton L, McNicholas S, Long F, Murshudov GN. REFMAC5 dictionary: organization of prior chemical knowledge and guidelines for its use. Acta Crystallogr D Biol Crystallogr 2004;60(Pt 12 Pt 1):2184-2195.
43. Winn MD, Ballard CC, Cowtan KD, Dodson EJ, Emsley P, Evans PR, Keegan RM, Krissinel EB, Leslie AG, McCoy A, McNicholas SJ, Murshudov GN, Pannu NS, Potterton EA, Powell HR, Read RJ, Vagin A, Wilson KS. Overview of the CCP4 suite and current developments. Acta Crystallogr D Biol Crystallogr 2011;67(Pt 4):235-242.
44. Emsley P, Lohkamp B, Scott WG, Cowtan K. Features and development of Coot. Acta Crystallogr D Biol Crystallogr 2010;66(Pt 4):486-501.
45. Joosten RP, Long F, Murshudov GN, Perrakis A. The PDB_REDO server for macromolecular structure model optimization. IUCrJ 2014;1(Pt 4):213-220.
46. Chen VB, Arendall WB, 3rd, Headd JJ, Keedy DA, Immormino RM, Kapral GJ, Murray LW, Richardson JS, Richardson DC. MolProbity: all-atom structure validation for macromolecular crystallography. Acta Crystallogr D Biol Crystallogr 2010;66(Pt 1):12-21.
47. Schrodinger, LLC. The PyMOL Molecular Graphics System, Version 1.8. 2015.
48. Phillips JC, Braun R, Wang W, Gumbart J, Tajkhorshid E, Villa E, Chipot C, Skeel RD, Kale L, Schulten K. Scalable molecular dynamics with NAMD. J Comput Chem 2005;26(16):1781-1802.
49. Humphrey W, Dalke A, Schulten K. VMD: visual molecular dynamics. J Mol Graph 1996;14(1):33-38, 27-38.
50. Schneidman-Duhovny D, Inbar Y, Nussinov R, Wolfson HJ. PatchDock and SymmDock: servers for rigid and symmetric docking. Nucleic Acids Res 2005;33(Web Server issue):W363-367.

51. Mashiach E, Schneidman-Duhovny D, Andrusier N, Nussinov R, Wolfson HJ. FireDock: a web server for fast interaction refinement in molecular docking. Nucleic Acids Res 2008;36(Web Server issue):W229-232.
52. Slabinski L, Jaroszewski L, Rychlewski L, Wilson IA, Lesley SA, Godzik A. XtalPred: a web server for prediction of protein crystallizability. Bioinformatics 2007;23(24):3403-3405.
53. Hornbeck PV, Zhang B, Murray B, Kornhauser JM, Latham V, Skrzypek E. PhosphoSitePlus, 2014: mutations, PTMs and recalibrations. Nucleic Acids Res 2015;43(Database issue):D512-520.
54. Di Tommaso P, Moretti S, Xenarios I, Orobitg M, Montanyola A, Chang JM, Taly JF, Notredame C. T-Coffee: a web server for the multiple sequence alignment of protein and RNA sequences using structural information and homology extension. Nucleic Acids Res 2011;39(Web Server issue):W13-17.
55. Krissinel E, Henrick K. Inference of macromolecular assemblies from crystalline state. J Mol Biol 2007;372(3):774-797.
56. Holm L, Laakso LM. Dali server update. Nucleic Acids Res 2016;44(W1):W351-355.
57. Oliveira SH, Ferraz FA, Honorato RV, Xavier-Neto J, Sobreira TJ, de Oliveira PS. KVFinder: steered identification of protein cavities as a PyMOL plugin. BMC Bioinformatics 2014;15:197.
58. Pace CN, Scholtz JM. A helix propensity scale based on experimental studies of peptides and proteins. Biophys J 1998;75(1):422-427.
59. Lau SY, Taneja AK, Hodges RS. Synthesis of a model protein of defined secondary and quaternary structure. Effect of chain length on the stabilization and formation of two-stranded alpha-helical coiled-coils. J Biol Chem 1984;259(21):13253-13261.
60. Manning MC, Woody RW. Theoretical CD studies of polypeptide helices: examination of important electronic and geometric factors. Biopolymers 1991;31(5):569-586.
61. Choy N, Raussens V, Narayanaswami V. Inter-molecular coiled-coil formation in human apolipoprotein E C-terminal domain. J Mol Biol 2003;334(3):527-539.
62. Udeshi ND, Svinkina T, Mertins P, Kuhn E, Mani DR, Qiao JW, Carr SA. Refined preparation and use of anti-diglycine remnant (K-epsilon-GG) antibody enables routine quantification of 10,000s of ubiquitination sites in single proteomics experiments. Mol Cell Proteomics 2013;12(3):825-831.
63. Appelhoff RJ, Tian YM, Raval RR, Turley H, Harris AL, Pugh CW, Ratcliffe PJ, Gleadle JM. Differential function of the prolyl hydroxylases PHD1, PHD2, and PHD3 in the regulation of hypoxia-inducible factor. J Biol Chem 2004;279(37):38458-38465.

초 록

N-Myc downstream-regulated gene 단백질은 α/β-hydrolase 구조를 지니고 있는 군으로 지금까지 세포 증식, 분화, 그리고 저산소증에서 유도되는 암세포의 대사에 큰 영향을 끼치는 것으로 보고되었다. NDRG 단백질 군은 4가지 동형 단백질이 존재하며 이 중 NDRG3 단백질은 전립선 암에서의 증식 및 전이와 밀접하게 관련이 있으며, 특히 젖산 유도의 저산소증 반응 및 종양 발생에서 핵심적인 역할을 할 것으로 밝혀졌다. 본 논문에서는 NDRG3 단백질의 결정 구조를 2.2 Å 해상도로 구조를 규명하고, NDRG3 단백질의 생물물리학적 특징을 제시하였다. NDRG3는 용액 상에서 단량체 혹은 이량체로 존재하며 결정 구조를 통해 이량체의 결합 구조를 제시하였다. NDRG3는 구조적으로 α/β-hydrolase 부류와 비슷하지만 활성 부위에 핵심적인 잔기가 비활성화된 잔기로 변형되어 있어 가수분해 기능이 없을 것으로 추측할 수 있다. 또한 NDRG3의 구조는 기존에 밝혀진 NDRG2 단백질과 아미노산 서열, 구조적으로 비슷하지만, NDRG2의 종양억제기능으로 핵심적인 α6 헬릭스 구조 부분이 유연한 루프 형태로 바뀐 것을 확인할 수 있었다. 이러한 구조적 차이를 토대로 NDRG3는 종양억제기능을 가진

NDRG2와는 다른 역할을 할 것으로 유추한다. 따라서, 본 연구결과는 NDRG3의 분자 범위에서의 연구를 수행하는데 구조적, 생물물리학적 특징을 제시하였다.

주요어 : N-Myc downstream-regulated gene 3 (NDRG3); α/β-hydrolase fold; 단백질 결정; Unfolded helix
학 번 : 2014-30556

Acknowledgements

I would like to fully appreciate my research supervisor, Professor Byung Woo Han, for proceeding this project during my Ph.D course. Also, I sincerely thank Prof. Jung Weon Lee, Prof. Young-Joon Surh, Prof, Hyuk-Jin Cha, and Dr. Hyoun Sook Kim for scientifically thorough advices to my dissertation. Ms. Kyung A Kim made initial crystals of NDRG3, and Ms. Yuri Choi and prof. Hyung Ho Lee helped to implement SEC-MALS experiments. Dr. Dong Chul Lee, Dr. Kyung Chan Park, and Dr. Young Il Yeom introduced the function of NDRG3 protein. Thanks to them, I could start this project. Dr. Joon Sung Park, Dr. Hyunggu Han, Prof. Hyun-Jung Kim revised my manuscript. Especially, Dr. Jun Young Jang gave me brilliant ideas and sincerely helped me to write manuscript. I thank the staff members of BL-7A and BL-11C at the Pohang Accelerator Laboratory (Pohang, Republic of Korea) for X-ray diffraction experiments. I also thank the staff members of AR-NE3A of the Photon Factory (Tsukuba, Japan). Dr. Myung Hee Kim and Prof. Kyung-Jin Kim kindly provided the NDRG3, NDRG2 gene, and VHb fusion vector for cloning, respectively. I also thank Mr. Dong Man Jang and Dr. Nguyen Thi Kim Yen for contributing to SPR and ITC experiments, respectively.

감사의 글

2011년 9월 처음으로 한병우 교수님을 뵙고 구조약학실에서 대학원 생활을 시작한 이후, 박사 졸업을 하기까지 긴 시간이 걸렸습니다. 항상 노력에 비해 많은 것을 받아왔다고 생각해왔었고 졸업하는 과정에서도 제 노력과 능력에 비해 많은 도움을 받아 무사히 박사라는 타이틀을 받게 되었습니다. 먼저 이번 학기에 졸업을 하도록 저를 일깨워 주시고 지도 교수로서 존경하며 또한 제 인생의 지향점으로 항상 배우고 싶은 한병우 교수님께 진심으로 감사드립니다. 교수님께서 걸어오신 길을 보여주셨고 교수님의 경험에서 우러나온 조언을 통해 학문뿐만 아니라 인생에서 배워야 할 부분이 많다는 것을 느꼈습니다. 교수님과 처음 면담했을 때 말씀하셨던 것처럼 마라톤과 같은 박사 과정을 겪으면서 여러 생각이 들고 다른 길들이 많이 보였지만 교수님의 도움과 조언 덕분에 박사 과정을 마무리할 수 있었습니다. 박사 이후의 과정에서도 교수님의 조언대로 타인의 장점을 배우려고 노력하고 어느 집단에서도 그 분야의 최고를 배우려고 노력하겠습니다. 단백질의 구조에 대해 무지한 갓 학사 졸업한 저를 한 명의 박사로 성장하게 해주신 교수님의 노고와 지도에 다시 한번 감사드립니다.

대학원 과정에서 수업 및 조언을 아끼지 않으셨던 교수님들께도 감사드립니다. 신호 전달 체계에 대해 체계적으로 가르쳐주신 이정원 교수님, 학부 생화학 수업에서 생화학 및 구조의 중요성을 가르쳐주신 서영준 교수님, 특히 서영준 교수님께서 X-선 회절을 이용한 단백질 구조에 대해 수업하시면서 단백질의 결정 구조 하나만 밝혀도 박사 졸업을 할 수 있다는 말씀을 듣고 단백질 구조에 관심을 가지고 졸업까지 마무리할 수 있었습니다. 비록 면식은 없었지만 파컴 선배로서 따뜻한 조언 및 논문 지도를 해주신 차혁진 교수님, docking을 협업하면서 재미있는 주제를 많이 던져주신 Marc Diederich 교수님께도 감사드립니다. 또한 서세원 교수님께서 가르쳐주신 단백질의 구조 분석 및 신환철 교수님의 결정학 수업도 인상적이었습니다. 대학원 과정에서 저를 가르쳐주시고 지식을

넓혀주신 교수님들께 다시 한번 감사드립니다.

서세원 교수님 연구실에서 도움을 주신 김현숙 박사님, 윤지영 박사님, 임하나 박사님, 안두리 박사님께도 감사드립니다. Crystallization solution 및 mosquito machine 등 물심 양면으로 도움을 주셨고 단백질 구조 결정에 대한 경험 및 지식을 아낌없이 전수해 주셨습니다. 특히 김현숙 박사님께서는 과학적으로 심도있는 조언을 주시고 박사 과정에서의 어려움을 기꺼이 들어주셨습니다. 하와이 학회에서 보여주신 프로페셔널한 모습, 무엇보다 *Wincoot*의 창조자인 Paul Emsley 선생님께 MAD 및 SAD phasing을 설명하시는 모습은 제 평생 기억에 남을 것 같습니다. 현숙 박사님께서 구조약학실에 머무시는 동안 실험을 대하는 자세에서부터 번뜩이는 통찰력까지 많은 것을 배울 수 있었습니다.

제 논문을 완성하는데 도움을 주신 분들께도 감사를 전하고 싶습니다. 결정을 얻는 과정에서 좌절하는 와중에 단백질 결정 및 구조를 규명하는데 큰 도움을 준 김경아 학생에게 감사의 말을 전하고 싶습니다. 경아 학생의 도움이 없었더라면 제 졸업 논문의 주제가 완전히 달라졌을 것입니다. 경아 학생도 대학원 생활에서 좋은 일이 가득하길 기원합니다. NDRG3 단백질의 중요성을 세상에 알려주신 염영일 박사님, 박경찬 박사님, 그리고 이동철 박사님께도 감사드립니다. 선생님들께서 발표하신 신문기사 덕분에 관심을 가지고 이 프로젝트를 시작할 수 있었습니다. 제 논문을 꼼꼼히 봐주시고 개선하는데 큰 도움을 주신 중앙대 김현정 교수님께도 감사의 뜻을 전합니다. 또한 SEC-MALS 분석에 힘써주신 이형호 교수님과 최유리 학생, 실험에 필요한 plasmid를 제공해주신 김명희 박사님께도 정말 감사드립니다.

교수님의 선한 지도 편달 덕에 구조약학실에 들어와서 좋은 인연을 많이 만났습니다. 최고참이었던 박상호 선배님, 한미라 선배님, 박미설 선배님. 그리고 석사 졸업을 앞둔 이지연 선배님, 백장미 선배님. 한미라 선배님으로부터 처음 프로젝트를 받아 같이 실험하면서 계획적으로 꼼꼼히 실험하는 과정을 배웠습니다. 실험을 시작하기 전에 오늘 할 일을 적어두고 마치기 전에 내일 할 실험을 준비하는 과정 등, 실험을 대하는

기본적인 자세를 가르쳐준 미라에게 감사드립니다. 실험실의 정신적 지주이자 근면성실한 모습을 보여준 상호형, 박사과정 동안 기댈 수 있는 든든한 선배가 있다는 점에 감사드립니다. 실험실의 분위기 메이커인 미설, 고민 상담해주고 다정다감하게 북돋아준 지연, 실험실 생활에 정착하는데 친근하게 대해준 장미. 실험실의 좋은 선배님들을 만나서 대학원 생활이 즐거웠습니다.

제 동기인 박준성 박사와 백인화 학생에게도 진심으로 고맙습니다. 긴 시간동안 대학원 생활을 같이 공유하고 포항 가속기 연구소나 하와이, 바르셀로나 학회에서 준성이 덕분에 즐겁게 지낼 수 있었습니다. 실험실의 동력원인 준성이를 보며 동생이지만 많은 것을 보고 배울 수 있었습니다. 특히, 모든 일을 열성적이고 적극적으로 대하고 후회없이 노력하는 모습에 감탄해 마지않았으며, 준성이를 따라하면서 제 자신을 자극하고 더 노력할 수 있었습니다. 미국에서의 박사 후 과정에서도 곧 좋은 소식을 전해 줄 것으로 믿어 의심치 않습니다. 미국에서 박사과정을 진행 중인 인화도 행복과 행운이 가득하길 바랍니다. 인화 덕분에 대학원 생활에 활력을 가질 수 있었고, 관계에서는 부드럽지만 누구보다 진지하게 학문을 대하는 인화의 모습을 본받으려고 노력하고 있습니다. 동기이지만 제 멘토로 삼고 싶은 두 사람에게 감사드립니다.

실험실 구성원인 장준영 박사님, 한형구 박사, Nguyen Thi Kim Yen 박사, 송미경 학생, 김민주 학생, 장동만 학생, 오서영 학생, 이재석 학생, 오은경 학생, 천상원 학생, 양미현 선생님, 채원 선생님, 곧 들어올 강진모 학생, 박천준 학생 모두 뜻하는 바를 얻으시길 바랍니다. 날카로우면서도 따뜻하게 챙겨주는 형구, 누구보다 끈기를 가지고 최선을 다하는 Yen, 실험실에 활력을 나눠준 미경, 포항 실험을 도와준 민주, 막내였지만 지금은 실험실 그 자체이자 여러 후배들의 멘토가 될 동만, 훌륭하게 졸업하고 교수님의 자랑인 서영과 은경, 꼼꼼하게 최선을 다하는 재석, 항상 웃으면서 선배의 재미없는 얘기를 들어주는 상원, 동생들의 고민을 진심으로 들어주시고 도와주신 양미현 선생님, 행정 업무를 깔끔하게 처리해주시고 분위기 메이커이신 채원 선생님, 구조약학실에 오셔서 저의

연구 및 박사 과정의 힘듦을 같이 나누시고 아낌없는 조언을 주신 장준영 박사님. 제 실험실 생활에 양으로 음으로 도움을 준 모든 구조약학실 구성원에게 감사 인사를 드립니다. 또한 구조약학실을 거쳐가신 이경희 선생님, 박경미 선생님, 이지현 박사님, 전소영 선생님, 이현웅 선생님, 장민석 선생님, 김수진 선생님, 양경원 선생님, 이영빈 선생님, 이한별 선생님, 이나리 선생님, 심찬규 선생님, 현영음 학생, 남훈식 학생, 모멘 학생, 진소라 학생, 서주희 학생, 한근희 학생, 김경은 학생, 고혜린 학생 모두 감사드리며 행복 가득하시길 기원합니다. 특히, 제가 처음으로 가르친 현영음 학생이 가장 기억에 남습니다. 실험실 자리가 없어서 실험실에 대충 칸막이를 설치하고 실험실 생활을 시켰었고, 저도 지식이 부족해서 구조약학실의 매력을 잘 전달하지 못했었기에 미안한 마음이 듭니다. 그럼에도 불구하고 제 얘기를 잘 들어준 현영음 학생에게 고맙고 졸업 후 행운이 깃들길 기원합니다. 또한 이경희 선생님으로부터 단백질 정제의 꿀팁을 많이 배웠고 지루한 학식에 길들여 있던 와중에 맛있는 점심을 많이 사주셨습니다. 이경희 선생님과 운주에게도 행운을 빌어드립니다.

실험실 구성원 외에도 대학원 생활을 같이 진행하며 기쁨과 즐거움을 나눈 최훈, 지승원 박사님, 최배정 박사님, 포항 가속기 연구소를 나눠 사용하고 UV−microscope를 가르쳐 준 배의영 교수님 연구실의 가동현 박사, 문소진 박사님, DRS 및 ARS 단백질 연구에 도움을 주신 김성훈 교수님 연구실의 권남훈 박사님, 이진영 박사님, 김대규 박사님, 김병규 박사님, 정승재 박사님, 세포 배양의 기본부터 가르쳐 주신 김도희 박사님과 정훈이. 저 혼자만으로는 해결할 수 없었던 일들을 도와주신 여러분들께 감사의 뜻을 전해드리며 원하시는 뜻을 펼치시길 기원합니다.

심심한 대학원 생활에 활력을 불어넣어준 태웅형, 두현이, 지원형, 대학원 생활의 고초를 공유하며 덜어준 장규, 동영이, 항상 안부를 물어봐준 대성이 모두 고맙습니다. 솔직 과감하면서도 사려깊은 태웅형으로부터 정서적이나 경제적이나 많은 도움을 받았습니다. 일요일마다 따뜻하게 맞이 해주신 청라 365 약국의 선생님들, 일생의 도피처에서 반겨주

신 로스트아크의 루메초행임니다 멤버 분들, 서강대학교 조규봉 교수님 연구실의 염태호 선생님 모두 감사의 뜻을 전해드립니다.

그리고 박사 과정의 시작과 끝을 곁에서 지켜보며 제 모난 마음과 감정을 따뜻하게 품어준 가영에게 고마운 마음과 사랑을 전하고 싶습니다.

마지막으로 박사 과정의 긴 시간동안 묵묵히 지켜봐주신 아버지 김천수, 어머니 강순자, 그리고 누나 김지현에게 정말 감사드립니다. 가족의 따뜻한 응원과 격려 덕분에 박사 학위를 받을 수 있었습니다. 항상 무뚝뚝하고 내색을 하지 않았지만 이 자리를 빌어 가족들에게 진심 어린 감사와 사랑한다는 말을 전하고 싶습니다. 제 연구의 성과 및 박사 과정에서의 모든 업적을 가족에게 바치며 감사의 글을 마무리하겠습니다.

2020 년 1월 21일 김경록 올림